Solid-State batteries based on sulfide and oxyhalide electrolytes.

Beatriz Moura Gomes
Masters in physics engineering
Department of physics and astronomy from Faculty of sciences of University of Porto
2023

Supervisor
Maria Helena Sousa Soares de Oliveira Braga, Associate Professor, Faculty of Engineering of University of Porto

Co- Supervisor
Luís Miguel Oliveira, Research Coordinator, INEGI

MatΣR
Materials Energy Research

U.PORTO
FEUP FACULDADE DE ENGENHARIA
UNIVERSIDADE DO PORTO

U.PORTO
FACULDADE DE CIÊNCIAS
UNIVERSIDADE DO PORTO

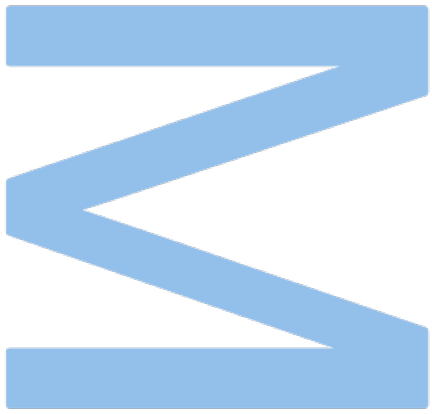

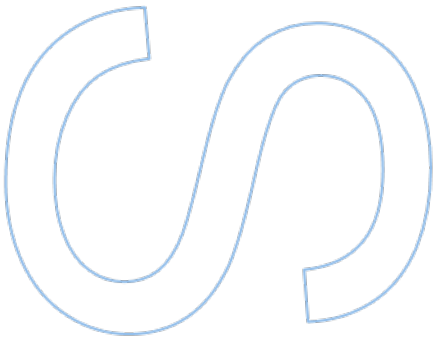

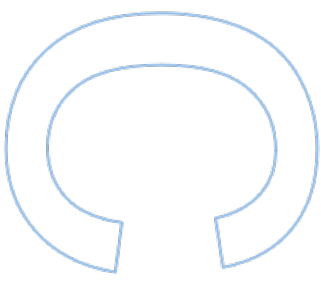

Dedicated to my Parents

Acknowledgments

First off, I want to express my gratitude to Professor Helena Braga, my supervisor. She didn't just teach me a ton about science; she also inspired and supported me on a personal level; even whenever I was close to losing it, she was there to calm me down. Her journey as a scientist and as a woman is something I truly admire. I hope to find my own path in the future, inspired by her making her proud. I also want to extend my thanks to my colleagues at MatER. While I plan to personally express my gratitude to each of them, I'd like to start by acknowledging them as a team. They've been by my side since day one, offering support and guiding me through my journey at the laboratory. I hope I brought joy, laughter, and music to your workdays. Thank you also to my co-supervisor Luís Oliveira for your contribution on this academic journey.

I'd like to begin my thanks with my colleague Manuela Baptista. She was the one who welcomed me into the laboratory, teaching and explaining the concepts and guiding me through procedures. Her incredible patience towards me and availability with her work time were beyond amazing – I couldn't have asked for better. Nuno Guerreiro, our atomic force microscope journey has brought me a lot of excitement and good memories. However, the unforgettable experiences during our PULSELiON trip to Finland surpassed everything else. I just wanted to say a big thank you for all your help. Mafalda, our paths in the lab might have crossed just a few times, but I've always admired your strong work ethic and responsibility. Thank you on a personal level. You've become my friend; thanks for being that motivating force that pushes me not to give up. Beatriz, sharing the same name doesn’t show how much in common we have. Your incredible work ethic truly impresses me and motivates me to improve myself; however, it’s as a friend that you inspire me the most. Thanks for all your advice and for turning our lunch breaks into gym class torture sessions – it's all in good fun!

I want to thank my boyfriend, João, for enduring my stressed-out moments, which were quite frequent during these five years of studying (thanks to physics!). I'm sorry for often taking it out on you. Thank you for your patience, help, and friendship. To my friends, thank you – I'll mention a few, but everyone matters. Lino, you ensured I ate lunch during my thesis; I tend to forget when working. Chico Zé, working on that paper together was great. Thanks for stopping me from overworking and reminding me how crazy I can be. To Sofia and Farida, you're my oldest friends. We've been through a lot, but we made it together, which makes me truly happy. Thanks for believing in me and keeping me in check when necessary.

Before mentioning my family, I want to thank someone from my past– Professor Luísa. Thank you for believing in me. Portuguese wasn't my best subject, but you saw potential in me, even in the course I didn't like. Your words continue to inspire and shield me from negative thoughts.

Finally, I want to thank my family, especially my awesome mom and dad. Parents have a big say in how kids turn out, and you two did a stellar job (at least, I like to think so!). Thanks for looking out for me all these years, being my support and inspiration and teaching me how to be decent. Your wisdom shaped who I am, and I hope I make you half as proud to have me as your kid as I am to have you as my parents. Thank you!

Resumo

O trabalho de pesquisa começou com a caracterização dos materiais ativos, $LiFePO_4$ e NMC900505 utilizando um *atomic force microscope* capaz de realizar *scanning kelvin probe microscopy*. Posteriormente, no âmbito do projeto europeu PULSELiON, foram fabricadas *coin cells*, com NMC como material ativo do cátodo, o eletrólito Li_6PS_5Cl como separador e lítio metálico como ânodo. Estas células foram testadas a 25 e 40 °C sendo o melhor desempenho surpreendentemente obtido para as células a 25 °C. O estudo final nesta tese explorou células que inicialmente não continham ânodo - células *anode-les*s. Durante a carga inicial, o lítio metálico é depositado no coletor de corrente do ânodo, criando-o. As células *anode-less* criadas nesta tese incorporaram $LiFePO_4$ como material ativo e o eletrólito ferroelétrico $Li_{2.99}Ba_{0.005}OCl$ como separador. Para otimizar a nucleação foram usadas camadas protetoras no coletor de corrente do ânodo de dois tipos diferentes - óxido de zinco e óxido de lítio. Ambas as configurações melhoraram com sucesso a nucleação de lítio no coletor. A capacidade máxima de descarga de 0,82 mAh foi alcançada para uma célula *anode-less* de óxido de zinco na qual se obteve uma espessura máxima de lítio de 0,296 µm. O processo de descarga desta célula durou um total de 273 horas, nunca atingindo um potencial inferior a 0,6 V.

Palavras-chave: Anode-less; All-Solid-State Batteries; Ferroelectric Electrolytes; Argyrodite Sulfide electrolytes.

Abstract

The research work started with the characterization of $LiFePO_4$ and NMC900505 materials using an atomic force microscope, which also enabled scanning Kelvin probe tests. Subsequently, within the scope of the PULSELiON European project, coin cells were assembled, featuring NMC as the cathode material, Li_6PS_5Cl as the electrolyte separator, and Li metal as the anode material. These cells underwent testing at 25 °C and 40 °C, yielding a surprising result—better performance at 25 °C, contrary to initial expectations. The final study in this thesis explored anode-less cells, a type of battery without an anode, relying solely on an anode current collector. Lithium metal is plated onto an anode current collector during the initial charge, creating the anode material. The anode-less cells crafted in this thesis incorporated $LiFePO_4$ as the active material and employed $Li_{2.99}Ba_{0.005}OCl$ ferroelectric glassy electrolyte as the separator. Two protective layers were employed on the collector—Zinc Oxide and Lithium Oxide to optimize nucleation. Remarkably, both configurations successfully improved lithium plating onto the collector. The maximum discharge capacity was achieved with Zinc Oxide anode-less cell, reaching 0.82 mAh corresponding to a maximum lithium thickness of 0.296 μm, for a discharge of 273 h, never reaching a potential inferior to 0.6 V. This thesis work aims to make a valuable contribution to the advancement of all-solid-state batteries.

Keywords: Anode-less; All-Solid-State Batteries; Ferroelectric Electrolytes; Argyrodite Sulfide electrolytes.

Table of Contents

List of Tables vi

List of Figures vii

List of Abbreviations x

Introduction 1

1.1. Context 1

1.2. Motivation 1

1.3. Objectives 2

1.4. Contributions 3

State of the Art 7

2.1. Features enabling energy storage in SSEs. 9

2.2. Synthesis methods 13

2.3. Overview of different types of Inorganic Solid-state electrolytes 15

2.3.1. Argyrodite Electrolytes 20

2.3.2. Antiperovskite Electrolytes 24

2.3.3. Halide Electrolytes 27

2.4. Ferroelectric materials prospects for harvesting and storing energy. 33

2.5. Cathode Materials 35

2.6. Anode-Less Assembly – Novel Approach for battery design and construction 37

Experimental Procedures 40

3.1. Materials 40

3.1.1. $Li_{2.99}Ba_{0.005}ClO$ electrolyte 40

3.1.2 Li_6PS_5Cl electrolyte 41

3.1.3 $LiFePO_4$ 41

3.1.4 NMC 41

3.1.5 ZnO – Zinc Oxide Solution 41

3.1.6 Li_2O – Lithium Oxide Solution 42

3.1.7 Laminated Film 42

3.2. Methods 42

3.2.1. Assembly and Testing Procedures for Coin Cells 47

3.2.2. Assembly and testing procedures for anode-less cells 49

3.2.3. Atomic Force Microscope and Scanning Kelvin Probe Sample Preparation Methodology 50

Results and Discussion 51

4.1. Scanning Kelvin Probe – Atomic Force Microscope 51

4.2. Coin – Cell 53

4.3. Anode – Less 56

4.3.1. Cu anode current collector 56

4.3.2. ZnO layer on the anode current collector 59

4.3.3. Li_2O layer on the anode current collector 63

Conclusion 70

References 73

Attachment 1 89

List of Tables

Table 1. Synthesis methods for the electrolytes LPSCl, LLZO, and NASICON and their possible influence on their ionic conductivity. CIF files: [41]–[54]..... 12
Table 2. C – rates charge and discharge..... 49
Table 3. Cu + 5 glue/$Li_{2.99}Ba_{0.005}ClO$ in cellulose/$LiFePO_4$/Cu pouch cell capacity throughout the charge discharge steps. Surface area A = 16 cm^2. All values were determined from voltages measured in the terminals of the external resistor. 59
Table 4. Cu/ZnO/$Li_{2.99}Ba_{0.005}ClO$ in cellulose/$LiFePO_4$/Cu pouch cell, with surface area A = 13.5 cm^2. All values were determined from voltages measured in the terminals of the external resistor – Cell 1. 62
Table 5. Cu/ZnO/$Li_{2.99}Ba_{0.005}ClO$ in cellulose/$LiFePO_4$/Cu pouch cell, with surface area A = 13.5 cm^2. All values were determined from voltages measured in the terminals of the external resistor – Cell 2. 63
Table 6. Cu/Li_2O + 5 dots of conductive glue /$Li_{2.99}Ba_{0.005}ClO$ in cellulose/$LiFePO_4$/Cu pouch cell capacity throughout the charge and discharge steps. Surface area A = 16 cm^2..... 68
Table 7. Cu/Li_2O/$Li_{2.99}Ba_{0.005}ClO$ in cellulose/$LiFePO_4$/Cu pouch cell capacity throughout the charge and discharge steps. Surface area A = 13.5 cm^2. 69

List of Figures

Figure 1. Ionic conductivities of ISE: $K_{2.99}Ba_{0.005}OCl$ and $Na_{2.99}Ba_{0.005}OCl$ [8]; $Li_{2.99}Ba_{0.005}OCl$ [9]; $Li_{5.4}PS_{4.4}Cl_{1.6}$ [10]; $LiTaOCl_4$ and $LiNbOCl_4$[11]; $Na_{25}S_5O_4I_7$ (theoretical study) [12]; $Li_{10}GeP_2S_{12}$ [13]; $Li_{5.5}PS_{4.5}Cl_{1.5}$ [14], $Na_{3.4}Zr_{1.9}Zn_{0.1}Si_{2.2}P_{0.8}O_{12}$ [15]; Na_3OBH_4 [16]; $Na_{3.4}Sc_{0.47}Zr_{1.6}Si_2PO_{12}$ [17]; $Na_{11}Sn_2PS_{12}$ [18]; $Na_{3.3}Zr_{1.7}La_{0.3}Si_2PO_{12}$ [19]; Li_3ScCl_6 [20]; $Li_{2.7}Zr_{0.3}In_{0.7}Cl_6$ [21]; Li_3InCl_6 [22]; Li_3OCl[9]; $Na_3Zr_2Si_2PO_{12}$ [23]; $Li_{2.5}Y_{0.5}Zr_{0.5}Cl_6$ [24]; $Na_3Sb_{0.5}S_4$ [25]; $Li_{2.25}Zr_{0.75}Fe_{0.25}Cl_6$ [26];Li_3YCl_6 [27]; Li_2ZrCl_6 [26]; and Li_3ErCl_6 [28]..... 8

Figure 2. Original data: **(a)** chemical potentials for electrically insulated materials and the lowest energy in the conduction band; **(b)** band gap reflecting the insulator or semiconductor character of the electrolytes. **Note:** the energy of the band gaps in (a) is $Eg = 2\times(EC - \mu electrolyte)\ eV$. 9

Figure 3. Synthesis methods: **(a)** High energy density ball milling [155]; **(b)** Pulsed laser deposition PLD [156]; **(c)** chemical vapor deposition CVD [157]; **(d)** Water mediated synthesis **Li_3InCl_6** [22], $Li_{2.99}Ba_{0.005}OCl$ [9], $K_{2.99}Ba_{0.005}OCl$ and $Na_{2.99}Ba_{0.005}OCl$ [8]. ... 11

Figure 4. Argyrodites summary scheme, Li_6PS_5Cl [31]; $Li_{5.4}PS_{4.4}Cl_{1.6}$ [10]; $Li_{5.5}P_{0.96}Sb_{0.04}S_{4.40}O_{0.10}Cl_{1.5}$ [75]; Na_3PS_4[76], [77], and Na_6AB_5X, A = (P, Sb), B = (S, Se), X = (Cl, Br, I) [78]..... 20

Figure 5. Antiperovskite electrolytes structures: **(a)** Li_3OCl [9]; **(b)** $Li_6SO(BH_4)_2$ [83]; CIF files: [41]–[54]. 24

Figure 6. Halide electrolytes Li_xMHal_y, where M = Ga, In, Er, Yb or divalent metals Fe, Zn and Hal is a halogen atom Hal = F, Cl, Br, I. Li_3InCl_6 [22], $LiGaCl_4$ [91], $LiErCl_6$ [28], Li_3YbCl_6[92], Li_6FeCl_8 [93], Li_2FeCl_4 [94], Li_2ZnCl_4 [95]. CIF files: [41]–[54]. 27

Figure 7.Dielectric, piezoelectric, and ferroelectric materials. Force F, polarization *P*, capacity *Q*, electric field *E*, potential energy *U*, and capacitance *C*, remanent polarization $P_{remanent}$, coercive electric field $E_{coercive}$ 32

Figure 8. NMC vs LFP: Structure, plating mechanism of Li ions, and optimizations ..... **Error! Bookmark not defined.**

Figure 9. Anode-less Batteries: Structure, plating mechanism of Li ions, and optimizations..... 38

Figure 10. Potentiostatic Electrochemical Impedance Spectroscopy (PEIS) curve of a commercial lithium-ion cell containing liquid electrolyte. 43

Figure 11. Charge and Discharge curve of a coin-cell featuring LFP as cathode material, LiPF6 liquid electrolyte and graphite as the anode material. Reproduced from ref.[153] CC BY 4.0..... 44

Figure 12. Chronopotentiometry test to study the Li plating/stripping performance of CGPE-GFW Li | Li symmetric cell at different density currents. Reproduced from ref. [154] CC BY 4.0. 45
Figure 13. Cyclic Voltammetry curve of a Coin-Cell Featuring LFP as Cathode Material, LiPF6 Liquid Electrolyte, and graphite as the anode material. Reproduced from ref. [153] CC BY 4.0. 46
Figure 14. Schematic representation of the half (coin) cell architecture. 47
Figure 15. Cell assembly: **(a)** materials; **(b)** cell; **(c)** cell protected by Teflon tape; **(d)** vacuum closed and sealed cell. 49
Figure 16. Two different samples analysed on the AFM. 51
Figure 17. AFM on NMC sample. **Topography**: **(a)** 2D and **(b)** 3D. **SKPM: (c)** 3D study and **(d)** 2D Potential study. 52
Figure 18. AFM on LFP sample: **Topography**: **(a)** 2D and **(b)** 3D. **(c)** SKPM analysis 52
Figure 19. Symmetric cell study: (a) PEIS test immediately after assembling; (b) chronopotentiometry test; (c) final PEIS after chronopotentiometry. 53
Figure 20. Charge/discharge cycling at 25 ºC for half (coin) cells with configuration: NMC/Li_6PS_5Cl/Li^0 at different C-rates. 54
Figure 21. Charge/discharge cycling at 40 ºC for half (coin) cells with configuration: NMC/Li_6PS_5Cl/Li^0 at different C-rates. 55
Figure 22. Specific capacity vs. number of cycles at (a) 25 ºC and (b) 40 ºC for coin cells with configuration: NMC/Li_6PS_5Cl/Li^0 at different C-rates. 56
Figure 23. The potential difference for a pouch cell with configuration Cu + 5 dots of glue/$Li_{2.99}Ba_{0.005}OCl$ in cellulose/$LiFePO_4$/Cu while cycling with external resistance of 985 kΩ. 58
Figure 24. Potential difference for two pouch cells with configuration Cu/ZnO/$Li_{2.99}Ba_{0.005}ClO$ in cellulose/$LiFePO_4$/Cu while cycling with external resistance of **(a)** 4.7 MΩ; 985 kΩ; 549 kΩ; 217 kΩ and 99.4 kΩ; **(b)** 985 kΩ; 559 kΩ; 217 kΩ and 98.9 kΩ; 59
Figure 25. Potentiostatic Impedance Spectroscopy of a pouch cell featuring the Cu/ZnO/$Li_{2.99}Ba_{0.005}OCl$ in cellulose/$LiFePO_4$/Cu configuration. PEIS performed after: **(a)** 4.7 MΩ charge discharge testing; **(b)** 985 kΩ charge discharge testing; **(c)** 549 KΩ charge discharge testing; **(d)** 217 kΩ charge discharge testing and **(e)** 99.4KΩ charge discharge testing. 61

Figure 26. Potential difference for two pouch cells with configuration Cu/Li_2O + 5 dots of conductive glue /$Li_{2.99}Ba_{0.005}ClO$ in cellulose/$LiFePO_4$/Cu while cycling with external resistance of (**a)** 980 kΩ;**(b)** 559 kΩ;**(c)** 4.7 MΩ; **(d)** 556kΩ and **(e)** 216 kΩ..... 64
Figure 27. Potentiostatic Impedance Spectroscopy of a pouch cell featuring the Cu/Li_2O + 5 dots of conductive glue /$Li_{2.99}Ba_{0.005}OCl$ in cellulose/$LiFePO_4$/Cu configuration. PEIS test was performed after: **(a)** 980 kΩ charge/discharge testing; **(b)** 559 kΩ charge/discharge testing. 65
Figure 28. Cyclic Voltammetry test results: (a) I vs. V; (b) Q-Q_0(C) vs. Potential. 66
Figure 29. Potential difference of a pouch cell with configuration Cu/Li_2O/$Li_{2.99}Ba_{0.005}ClO$ in cellulose/$LiFePO_4$/Cu while cycling with external resistance of (a) 980 kΩ; (b) 556 kΩ and (c) 216 kΩ..... 67
Figure 30. Potential difference of a pouch cell with configuration: **(a)** Cu/ Li_2O + 5 dots of conductive glue/ $Li_{2.99}Ba_{0.005}ClO$ in cellulose/$LiFePO_4$/Cu; and **(b)** Cu/Li_2O /$Li_{2.99}Ba_{0.005}ClO$ in cellulose/$LiFePO_4$/Cu, while cycling with external resistance. 69

List of Abbreviations

2D	TWO DIMENSIONS
3D	THREE DIMENSIONS
ABEE	AVESTA BATTERY AND ENERGY ENGINEERING
AFM	ATOMIC FORCE MICROSCOPY
AFSSB	ANODE-FREE SOLID-STATE BATTERY
ALD	ATOMIC LAYER DEPOSITION
ASSB	ALL SOLID-STATE BATTERIES
BM	BALL MILLING
CATL	CONTEMPORARY AMPEREX TECHNOLOGY LIMITED
CAVALI	CADEIA DE VALOR DO LÍTIO
CC	CURRENT COLLECTOR
CE	COULOMBIC EFFICIENCY
CIC	CIC ENERGIGUNE
CP	CHRONOPOTENTIOMETRY
CV	CYCLIC VOLTAMMETRY
CVD	CHEMICAL VAPOR DEPOSITION
DFT	DENSITY FUNCTIONAL THEORY
DOS	DENSITY OF STATES
EDLC	ELECTRICAL DOUBLE-LAYER CAPACITOR
EVS	ELECTRICAL VEHICLES
FCUP	FACULTY OF SCIENCE OF UNIVERSITY OF PORTO
FET	FERROELECTRIC TRANSISTORS
FETIS	FERROELECTRIC TOPOLOGICAL INSULATORS
FEUP	FACULTY OF ENGINEERING OF UNIVERSITY OF PORTO
HT	HEAT TREATMENT
ISE	INORGANIC SOLID ELECTROLYTES
LAGP	$LI_{1.5}AL_{0.5}GE_{1.5}(PO_4)_3$
LFP	$LiFePO_4$
LGP	$LIGE_2(PO_4)_3$
LIB	LITHIUM-ION BATTERIES
LIBS	LASER-INDUCED BREAKDOWN SPECTROSCOPY
LIRAP	LITHIUM RICH ANTIPEROVSKITES
LISICON	LITHIUM SUPER IONIC CONDUCTOR

LLTO	PEROVSKITE ELECTROLYTES
LPSC	LI6PS5CL
LYC	Li_3YCl_6
MATER	MATERIALS FOR ENERGY RESEARCH
NASICON	SODIUM SUPER IONIC CONDUCTOR
NC	NEGATIVE CAPACITANCE
NMC	$LINI_{1-X-Y}MN_XCO_YO_2$
O-ICSE	ORGANIC AND INORGANIC COMPOSITE ELECTROLYTES
PEIS	POTENTIOSTATIC ELECTROCHEMICAL IMPEDANCE SPECTROSCOPY
PLD	PULSE LASER DEPOSITION
PULSELiON	PULSED LASER DEPOSITION TECHNOLOGY FOR SOLID STATE BATTERY MANUFACTURING SUPPORTED BY DIGITALIZATION
PVDF	POLYVINYLIDENE FLUORIDE
RT	ROOM TEMPERATURE
SEI	SOLID ELECTROLYTE INTERPHASE
SEM	SCANNING ELECTRON MICROSCOPY
SKP	SCANNING KELVIN PROBE
SPE	SOLID-STATE POLYMER ELECTROLYTES
SS	SOLID-STATE
SSE	SOLID-STATE ELECTROLYTES
UP	UNIVERSITY OF PORTO
WF	WORK FUNCTION
WP	WORK PACKAGE
XPS	X-RAY PHOTOELECTRON SPECTROSCOPY
XRD	X-RAY DIFRACTION

Chapter 1

Introduction

1.1. Context

The outbreak of war in Europe brought to light the energy deficiencies experienced within the European Union and across the globe. This highlighted the necessity for each country to achieve energetic independence, serving as a driving force for the rapid development of new viable energy, storage, and production approaches. Over time, batteries have undergone tremendous advancements and become the leading technology to storage energy [1]. The most significant breakthrough in this field came with the development of Lithium-ion batteries (LIB), which have revolutionized energy storage, from portable charging devices to electric vehicles [2].

1.2. Motivation

Liquid or gel electrolytes are crucial for lithium-ion batteries (LIBs), allowing Li^+- ions to move between electrodes during battery cycling. However, rapid charging can lead to dendrite formation on the negative electrode's surface, especially at low temperatures. These dendrites are fractals and may eventually penetrate the separator, connecting both electrodes and creating a short circuit that poses significant safety risks due to the flammable character of liquid and gel electrolytes, the likelihood of thermal runways, and cathodes' oxygen release [3]. To overcome the challenges associated with traditional liquid and gel electrolytes, researchers have developed solid-state electrolytes that exhibit cation conduction, such as Li^+, Na^+, and K^+ [4], [5].

Solid-state electrolytes are not flammable, offer increased stability to dendrite formation, and are compatible with high-potential electrodes, allowing for higher energy-density batteries. Hence, solid-state electrolytes are expected to evolve to a level where they entirely surpass their predecessors and emerge as the predominant choice for electrolyte technology.

While electrolytes play a crucial role, batteries are fabricated using other essential components, with cathode materials being an example of significance. The cathode material significantly influences a battery's capacity and power output. Presently, most cathode materials utilized in batteries incorporate metals such as cobalt. Although these cathode materials showcase high capacity, they contain elements like cobalt, raising environmental concerns. Moreover, extracting these elements from mines raises ethical

questions, often including human rights violations and child labor exploitation. The $LiFePO_4$, LFP, cathode material represents an environmentally friendly choice. The abundant availability of its raw materials contributes to the cost-effectiveness of the cathode, leading to the development of more affordable battery technology. This cathode material is being studied and optimized and is starting to become the leading cathode option in the industry (e.g., Tesla, CATL, ABEE, etc.).

The anode is another crucial component of traditional batteries. Batteries that utilize lithium metal as the anode take advantage of its high theoretical capacity, leading to higher energy density than other anode materials like graphite. However, the safety concerns surrounding the maneuver of Li metal are countless, and, as a result, the commercialization of lithium-metal batteries has been hindered.

Anode-less solid-state batteries offer an innovative configuration where the battery doesn't have an anode component. These batteries consist of an anodic current collector, a separator with an electrolyte, a cathode, and cathodic current collectors. By eliminating the requirement of an anode, anode-less cells have gained attention in the battery industry due to their ease of assembly, enhanced safety, cost-effectiveness, and improved sustainability, as they eliminate the need for pure lithium metal layers in the manufacturing process. A prestigious research center such as CIC energiGUNE has highlighted the cutting-edge concept of an anode-less innovative configuration as a pivotal cornerstone for the future of battery technology.

1.3. Objectives

The primary objective of this thesis was advancing the development of an efficient anode-less battery cell containing $LiFePO_4$ (LFP) as the cathode material, and a ferroelectric electrolyte, $Li_{2.99}Ba_{0.005}OCl$. The goal was to improve the performance of anode-less cells through the incorporation of seed layers on the anode current collector to enhance Li metal nucleation. The second study developed in this thesis aimed to gain insights into the behavior of cells containing sulfur electrolytes and Li metal as the anode material. This was achieved with the assembly of coin cells featuring a sulfur electrolyte, Li_6PS_5Cl, NMC as the cathode $LiNi_{0.90}Mn_{0.05}Co_{0.05}O_2$, and Li metal as the anode. To achieve these goals the following steps were followed:

1. **Materials characterization:**
    a. Scanning Kelvin Probe (SKP) microscopy testing of solid-state electrolytes and cathodes.

   b. Atomic Force Microscopy (AFM) analysis of solid–state electrolytes and cathodes.

2. **Coin-cell assembly using solid-state electrolytes and different cathode materials:**
   a. Fabrication of pellets: monolayer of electrolyte and bilayers of electrolyte + cathode materials.
   b. Electrochemical testing of the cells:
      i. Potentiostatic Electrochemical Impedance Spectroscopy (PEIS).
      ii. Electrochemical performance: Charge and Discharge cycles.
      iii. Chronopotentiometry (CP)
3. **Assembling anode-less pouch cells**
   a. Oxide layer deposition to improve nucleation of lithium on the surface of the negative electrode.
   b. Fabrication of cells using an “industrial” production line.
   c. Electrochemical testing:
      i. Potentiostatic Electrochemical Impedance Spectroscopy (PEIS).
      ii. Electrochemical performance: Charge and Discharge cycles.
      iii. Cyclic Voltammetry (CV)

1.4. Contributions

This thesis was conducted at the MatER Laboratory in FEUP. The experimental work of this thesis was carried out under the PULSELiON and CAVALI projects.

In the PULSELiON project, my involvement covered different work packages (WP3 and WP5). The initial work on WP3 and WP5 involved round-robin tests, during which my colleague Manuela Baptista and I concentrated on assembling and testing solid-state coin cells containing the sulfur argyrodite electrolyte Li_6PS_5Cl. The methodology for producing pellets (solid separator and bilayer), assembly, and subsequent tests conducted on the coin cells will be described in the following sections of this document, particularly in the “Methods” chapter. Another study developed on WP3 involved the synthesis of cathode materials via wet synthesis; this study stayed in a preliminary phase.

Regarding the CAVALI Project, my involvement occurred during the project's concluding phase. During this stage, I successfully assembled pouch cells and contributed to refining the cell assembly process by implementing a pouch cell production line. Additionally, I played a role in enhancing the performance of anode-less cells by employing oxides to improve lithium nucleation on the anode electrode. My participation

in this project was a collaborative process with Manuela Baptista and all the work previously developed by her and my colleagues at the MatER laboratory.

The collaborative research during this master's program produced four articles, including a perspective paper. In the latter, I am the first author with a significant contribution to the research and original text. Two manuscripts are under review while two of the papers have already been published in high impact journals.

(1) "Building blocks of a cathode toward a more efficient battery: The $LiFePO_4$ case study". This article seeks to comprehend the factors that inhibit cathodes from reaching their theoretical capacity, explore the reasons behind irreversible losses during the initial cycle, and determine the extreme potentials to which battery cells should be cycled. Our findings were derived from a comprehensive understanding of electron transport properties and the reinforcement of their significance in enhancing battery performance. This study emphasizes the critical importance of total local potentials, electronic density of states (DOS), and charge carrier density in comprehending the electrochemical cycling behavior of battery cells, particularly in Li//LFP configurations with both liquid and solid electrolytes. The research establishes a stable plateau potential difference of 3.42 V, with maximum charge and minimum discharge potentials at 4.12 V and 2.80 V, respectively. The investigation reveals the formation dynamics of metastable phases at plateau voltages exceeding 3.52 V. Moreover, it demonstrates that determining the working chemical potentials of Li and Al involves combining work function and DOS analysis while highlighting carbon black's role beyond conductivity enhancement. The theoretical and experimental analysis encompassed Li, C, Al, Cu, LFP, $FePO_4$, $Li_{0.25}FePO_4$, polyvinylidene fluoride (PVDF), and Li_6PS_5Cl (LPSCl) materials using Density Functional Theory (DFT), SKP, and electrochemical methods. These findings, grounded in electrical properties, hold significance for all cathodes and batteries, aiding in selecting optimal formulations and cycling conditions.

My contributions to this paper were cell fabrication, experimental work, and helping draft the article's initial version. Furthermore, I played a vital role in preparing cells for SKP analysis, which focused on cells containing LFP and argyrodite. In terms of the manuscript, I revised the introduction. I assisted in crafting the results section, beginning with interpreting the chemical potential and work function relationship and the content related to interpreting SKP results involving Li_6PS_5Cl. To finish, I developed an introductory review and performed a dimensional analysis of the equations necessary for this study. This manuscript was already submitted and is under review.

(2) "Conditioning Solid-State Anode-less cells for the next generation of batteries", this article was already published in **Batteries Vol. 9 No. 8 p. 402, DOI: 10.3390/batteries9080402**. In this article, we fabricated two distinct variations of anode-less pouch cells. The first employed a copper negative current collector, while the second utilized the same copper current collector coated with a zinc oxide (ZnO) layer to enhance lithium nucleation. Both cell types shared a common all-solid-state electrolyte, $Li_{2.99}Ba_{0.005}ClO$ electrolyte, embedded within a cellulose matrix and featuring a $LiFePO_4$ cathode. Through a combination of direct methodologies, X-ray Photoelectron Spectroscopy (XPS) and Laser-Induced Breakdown Spectroscopy (LIBS), alongside indirect techniques like electrochemical cycling, impedance measurements, and Scanning Electron Microscopy (SEM), we successfully verified the occurrence of lithium plating during the cell charging process. The maximum thickness obtained by lithium plating during charging reached 2.9 μm, while the subsequent discharge reduced it 0.13 μm. Notably, the discharge started at a maximum potential of 3.2 V, a condition only possible if a high chemical potential phase like an anode, such as lithium (Li), were to form during plating. The anode-less cells exhibited rapid initial discharge at higher potentials, then transitioned to a sustained discharge potential for prolonged durations. This long discharge behavior is likely attributed to the ferroelectric characteristics of the electrolyte.

In terms of my experimental involvement, I actively participated in synthesizing the materials essential for the pouch cell, alongside contributing to its meticulous assembly process, using all the equipment of the production line of pouch cells. Furthermore, I helped conduct tests on the cells, utilizing the indirect methodologies already mentioned. Transitioning to my contributions towards drafting the article, I assisted in revising the results section and fine-tuning the final draft of the manuscript. Additionally, I contributed to developing the graphical abstract, ensuring its clear and concise representation. This article resulted from the work produced during the final stage of the CAVALI project.

(3) "A perspective on the building blocks of a solid-state battery: from solid electrolytes to quantum power harvesting and storage", this article was already published in J. Mater. Chem. A, 2024, 12, 690–722 **DOI: 10.1039/D3TA04228F,** where I am first author. This paper offers an in-depth perspective on the essential components of solid-state batteries, ranging from all-solid-state electrolytes to quantum power harvesting and storage. To begin with, we explore the key attributes that define an effective electrolyte. Our findings confirm that the most promising electrolytes are semiconductors with a low work function, exhibiting behavior reminiscent of anodes.

Additionally, electrolyte categories containing multiple dominant elements like S, O, and Cl, exemplified by argyrodites and oxyhalide electrolytes, demonstrate more significant potential than those centered around a single dominant element, such as sulfides, oxides, and halides. We also discussed devices containing ferroelectric electrolytes capable of simultaneously harvesting and storing energy. Ferroelectric materials possess exceptional qualities that hold the potential to revolutionize the upcoming generation of electronic devices. Furthermore, our exploration extends to Ferroelectric Topological insulators (FETIs), opening a realm of new possibilities. Several innovative studies in this domain were enumerated in this article. Moving forward to the minuscule, a comprehensive overview of the principles governing quantum batteries was provided. We presented the general quantum model and three different types of quantum batteries: the Dicke model, the spin-chain model, and the quantum thermal machines, whose function mechanism is based on Maxwell's demons (isothermal baths) and quantum refrigerators. By presenting these insights, this article aimed to contribute to advancing solid-state batteries and quantum power harvesting and storage, technologies that maintain coherence even at macro sizes, paving the way for more efficient and sustainable electronic devices.

I contributed several to this article, including drafting the text and creating summarizing and explanatory schematics. Additionally, I actively participated in developing simulations related to the Dicke quantum batteries. Notably, I provided revisions solely for the Dicke and spin chain chapters, while all other sections were initially written by me and reviewed collaboratively with the other authors.

(4) “Toward energy harvesting through device-driven Josephson plasma feedback”

In this article, I have made experimental contributions to cell fabrication, low-temperature electrochemical experiments, and nm-SKP experiments. Furthermore, I have developed the Python code to validate the experimental results (presented in **Attachment 1**and confidential as the paper is under review).

Chapter 2

State of the Art

One key component of a battery is the electrolyte, making it one of the essential factors for battery performance. An ideal solid-state electrolyte is said to possess the following properties: **(1)** high ionic conductivity (**Figure 1**); **(2)** low electrical conductivity (**Figure 2**); **(3)** a wide electrochemical window of stability to match with high-voltage cathodes (**Figure 2**); **(4)** a high A^+-ion transference number for inhibiting the formation of negative space charge near the anode and promoting uniform ion deposition; **(5)** sufficient mechanical strength to inhibit ion growth; **(6)** good electrode wettability and low interfacial resistance with the electrodes; **(7)** good flexibility to accommodate the change of the electrodes' volume during battery charge and discharge; **(8)** good thermal stability to ensure safe and stable operation of batteries at lower and higher temperatures; **(9)** easy fabrication and low cost.

It is possible to distinguish three types of solid electrolytes: Inorganic Electrolytes (ISEs) [6], polymer electrolytes (SPE) [7], and organic and inorganic composite electrolytes (O-ICSE). O-ICSE is the most recent class of electrolyte, as its composition combines ISE and SPE characteristics. However, studying these composites is a relatively recent subject, and much research still needs to be done. SPEs consist of a polymer matrix and Li salts without any liquid solvents. These electrolytes are lightweight and easy to shape, therefore capable of adapting to different battery structures. They also have good electrode wettability and flexibility that reduces the impact of electrode volume change during the charge-discharge process. However, they cannot always suppress the formation of Li dendritic structures, and the ionic conductivity of SPEs is very low, 10^{-4} - 0.01 $mS.cm^{-1}$, representing a significant drawback for application in all-solid-state batteries. On the other hand, inorganic solid electrolytes possess high ionic conductivities capable of competing even with liquid electrolytes > 10 $mS.cm^{-1}$, vertical line in **Figure 1**. ISE is also associated with higher mechanical modules; they inhibit the growth of Li dendrites, are non-flammable, and are therefore associated with a higher safety level.

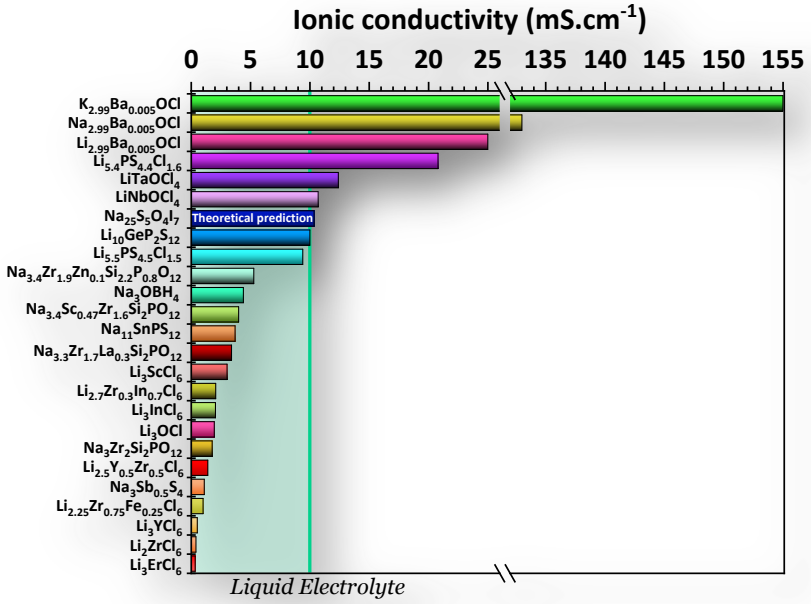

Figure 1. Ionic conductivities of ISE: $K_{2.99}Ba_{0.005}OCl$ and $Na_{2.99}Ba_{0.005}OCl$ [8]; $Li_{2.99}Ba_{0.005}OCl$ [9]; $Li_{5.4}PS_{4.4}Cl_{1.6}$ [10]; $LiTaOCl_4$ and $LiNbOCl_4$[11]; $Na_{25}S_5O_4I_7$ (theoretical study) [12]; $Li_{10}GeP_2S_{12}$ [13]; $Li_{5.5}PS_{4.5}Cl_{1.5}$ [14], $Na_{3.4}Zr_{1.9}Zn_{0.1}Si_{2.2}P_{0.8}O_{12}$ [15]; Na_3OBH_4 [16]; $Na_{3.4}Sc_{0.47}Zr_{1.6}Si_2PO_{12}$ [17]; $Na_{11}Sn_2PS_{12}$ [18]; $Na_{3.3}Zr_{1.7}La_{0.3}Si_2PO_{12}$ [19]; Li_3ScCl_6 [20]; $Li_{2.7}Zr_{0.3}In_{0.7}Cl_6$ [21]; Li_3InCl_6 [22]; Li_3OCl[9]; $Na_3Zr_2Si_2PO_{12}$ [23]; $Li_{2.5}Y_{0.5}Zr_{0.5}Cl_6$ [24]; $Na_3Sb_{0.5}S_4$ [25]; $Li_{2.25}Zr_{0.75}Fe_{0.25}Cl_6$ [26];Li_3YCl_6 [27]; Li_2ZrCl_6 [26]; and Li_3ErCl_6 [28]. Note: the ionic conductivity of the liquid electrolytes contrapart is ≈10 $mS.cm^{-1}$.

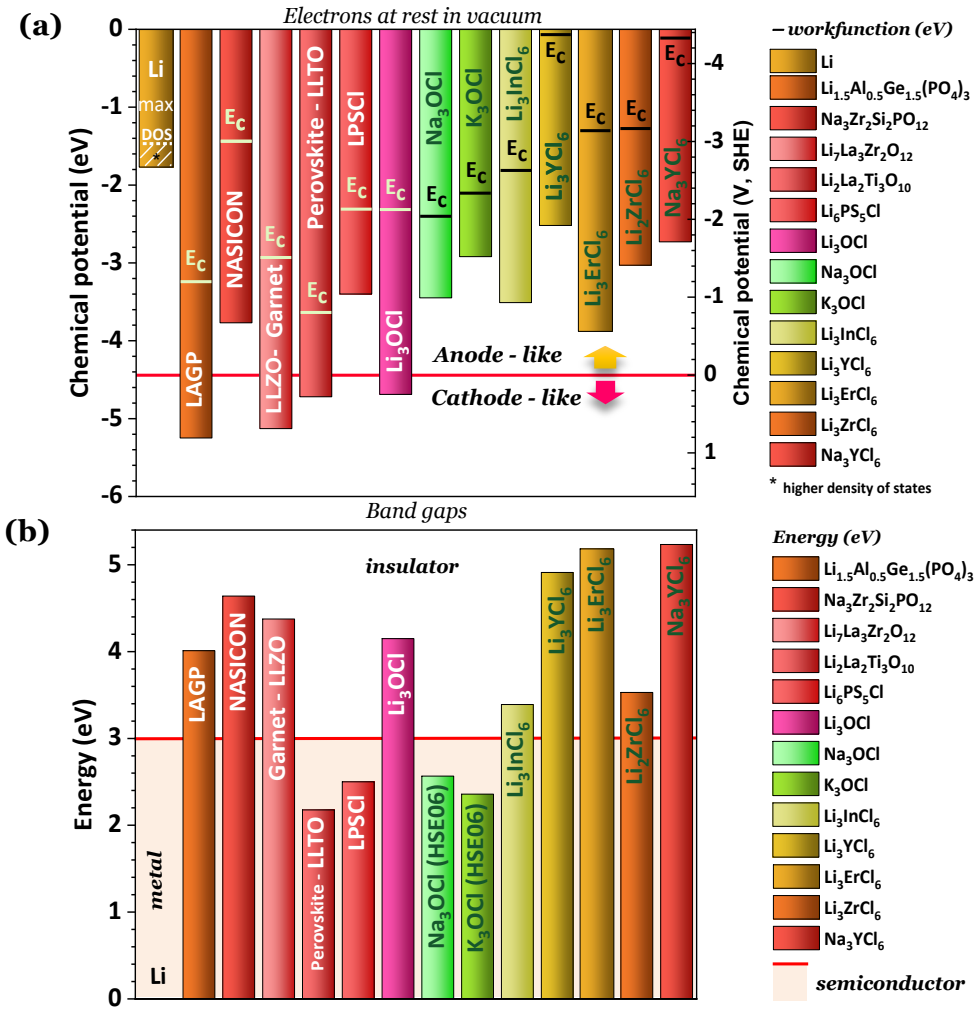

Figure 2. Original data: **(a)** chemical potentials for electrically insulated materials and the lowest energy in the conduction band; **(b)** band gap reflecting the insulator or semiconductor character of the electrolytes. **Note:** the energy of the band gaps in (a) is $E_g = 2\times(E_C - \mu_{electrolyte})\ eV$.

2.1. Features enabling energy storage in SSEs.

The ionic conductivity in solid electrolytes depends on parameters such as the mobile ions' concentration, size and mobility, lattice structure and defects, and conduction mechanisms. Performing solid electrolytes, like liquid electrolytes, display mass and charge transport. The solid electrolytes herein typically exhibit cation conductivity instead of liquid electrolytes, which count with both cation and anion motilities. Thus, intensive research on ionic transport in solid electrolytes exhibiting fast ionic conductivity at room temperature (RT) is needed.

In solid electrolytes, ions move through disordered sublattices within an enclosed, cage-like framework. The equation that expresses the ion conduction in solid-state

electrolytes, $\sigma_i = n_i q \vartheta_i$, where n_i, q, ϑ_i are the mobile ion concentration, elementary charge, and ionic mobility. These parameters are dependent on the temperature following an Arrhenius-type behavior. The ionic conductivity is related to the diffusivity of mobile ions - which is given by the Nernst-Einstein equation, $D_i = \frac{\sigma_i k_B T}{n_i z_i^2 q^2}$, where k_B and T are Boltzmann's constant and absolute temperature, z_i number of transferred charges per ion, q is the unitary charge of the electron.

Ionic diffusion in inorganic materials consists of ions hopping between the adjacent available sites, overcoming a higher energy barrier, the activation energy, due to geometry constraints and electrostatic interactions. Generally, two different hopping mechanisms can be distinguished: direct and knock-off. In the direct hopping mechanism, an individual ion hops from one lattice site to its adjacent vacant site. In contrast, the knock-off-hopping is due to an indirect interstitial mechanism where an interstitial atom pushes the matrix atom toward another interstitial site and realizes ionic transport.

In solid electrolytes, to enhance the ionic conductivity, it is necessary to create highly disordered defects for ions to move, designated Schottky and Frenkel point defects. According to the Arrhenius model, the ionic conductivity in crystalline solids is given by the equation $\sigma_i = \frac{A}{T} e^{-\frac{E_A}{k_B T}}$, where A is a pre-exponential factor, and E_A is the activation energy of diffusion. The predominant carriers for ion conduction are point defects in solids; this characteristic excludes most inorganic materials due to the lack of functional defects for ion migration or high activation energy. Thanks to the advances in crystal structure engineering, it was discovered that only a limited number of materials sharing types of structures could diffuse Li^+ and Na^+ ions efficiently.

The fundamentals of solid-state batteries surpass the internal resistance associated with ionic transport, which is a consequence, not the driving force for the ionic and electric. The driving force of a battery is associated with the necessity of aligning the electrochemical potentials, according to the equation,

$$\bar{\mu}_j - \bar{\mu}_i = \mu_j - \mu_i + z_i e(\phi_j - \phi_i) \quad (1)$$

where j and i are different species in electrical contact, as in a heterojunction; $\bar{\mu}_j$, μ_j, and ϕ_j are the electrochemical potential or Fermi level for the solid species, chemical potential, and surface potential of species j; $z_i e \phi_j$ is an electrical work performed by i on the surface of j; z_i is the valence of the mobile charges (e.g., $z_{Li} = +1$). When the electrochemical potentials are equalized, $\bar{\mu}_j - \bar{\mu}_i = 0 = \mu_j - \mu_i + z_i e(\phi_j - \phi_i) \Rightarrow \mu_j -$

$\mu_i = z_i e(\phi_i - \phi_j) = z_i e \Delta V_{ij}$. If both i and j are conductors, such as the electrodes, they may equalize their chemical potentials by exchanging electrons upon electrical contact. Nonetheless, if one of the species is an insulator or semiconductor, when possible, electrical double-layer capacitors EDLC of potential difference ΔV_{ij} will form at the interfaces to equalize the difference in chemical potentials. In a solid-state device such as a battery, the EDLCs store the energy. Therefore, for energy storage to happen, an interface involving at least one semiconductor or insulator must be present. A battery cell's asymmetry relies on one or two double-layer capacitors formed at the interface negative electrode/electrolyte or electrolyte/positive electrode.

From the EDLCs, electrons tunnel to the electrolyte's surface, reducing the Li^+ to Li^0, which then diffuses to the cathode under Fick's law of diffusion. The latter mechanism is more likely if the electrolytes' surface states are dense enough, $\geq 10^{12}$ states.cm^{-2}, to hold a specific concentration of electrons. The EDLC is a triangular quantum well or barrier, depending on the electrolyte/cathode relative chemical potentials. However, the anode/electrolyte/cathode will represent a quantum well or barrier themselves depending on the relative positions of the chemical potentials. When the electrolyte is ferroelectric, the difference in chemical potentials at the interfaces is minimized [29], and the internal resistance is reduced to the activation energy associated with the mobility of the ions.

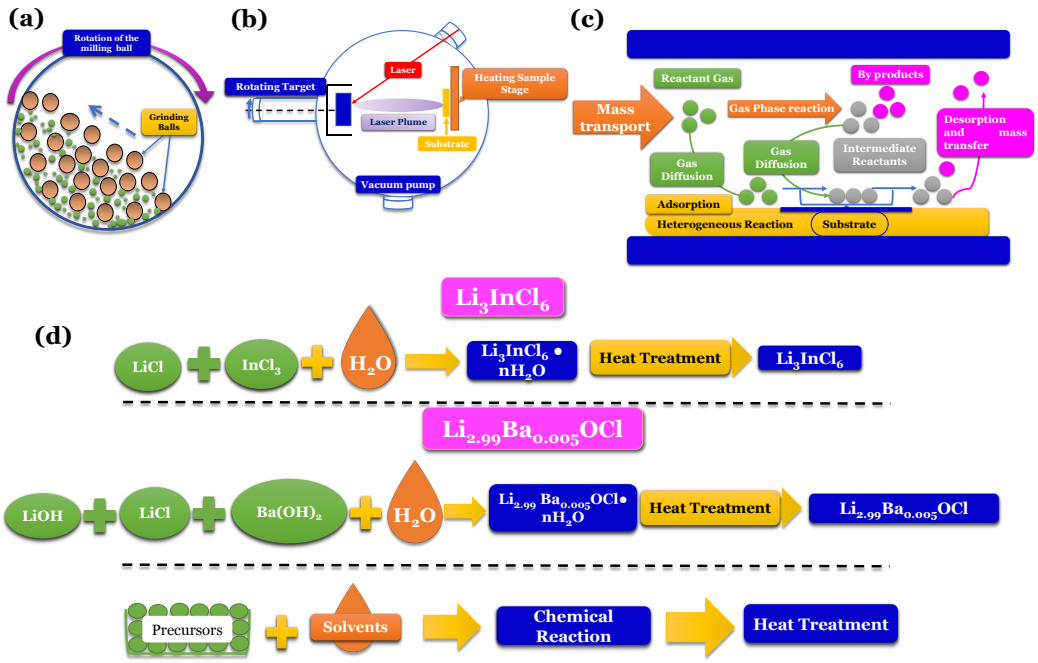

Figure 3. Synthesis methods: **(a)** High energy density ball milling [155]; **(b)** Pulsed laser deposition PLD [156]; **(c)** chemical vapor deposition CVD [157]; **(d)** Water mediated synthesis **Li_3InCl_6** [22], $Li_{2.99}Ba_{0.005}OCl$ [9], $K_{2.99}Ba_{0.005}OCl$ and $Na_{2.99}Ba_{0.005}OCl$ [8].

Table 1. Synthesis methods for the electrolytes LPSCl, LLZO, and NASICON and their possible influence on their ionic conductivity. CIF files: [41]–[54].

Electrolyte	Fabrication Method	Parameters	Ionic conductivity ($mS.cm^{-1}$)	Crystal Structure	Ref.
Li_6PS_5Cl - LPSCl	Ball Milling	10h - 600 rpm	1.3 (25 °C)	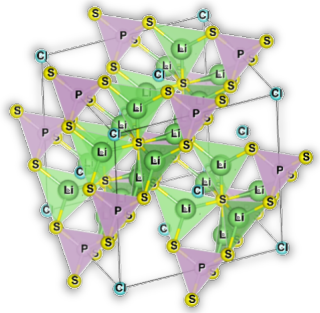	[30]
	Solid State Reaction	**(1)** $LiCl+Li_2S+P_2S_5$ 100 rpm for 1h **(2)** 10h of annealing	5.0 (26°		[31]
	Wet Phase	Mixture with ethanol solution	1.4×10^{-2} (RT)		[32]
	Wet Phase ($LiCl+Li_2S+P_2S_5$+ pyridine)	**(1)** P_2S_5 + pyridine 400 rpm, RT **(2)** add LiCl + Li_2S to 400 rpm at 70 °C **(3)** removing pyridine in vacuum at 120 °C	4.3 (RT)		[33]
$Li_7La_3Zr_2O_{12}$ - LLZO	Solid State Reaction	**(1)** 200 rpm 12h in 2-propanol **(2)** 900 °C 4h **(3)** 200 rpm 12h	0.2 (25 °C)	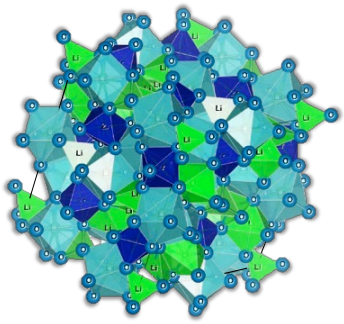	[34]
	Radio Frequency magnetron sputtering	RF power of 40, 60, and 80 W at a working pressure of 7 MPa under Ar atmosphere.	4×10^{-4} (25 °C)		[35]
	Pulsed Laser Deposition – Laser annealed	$f_{laser\ pulse}$= 10 Hz; 7.5 $J.cm^{-2}$; 7700 shots; thickness ~1 µm; laser annealing	7.4×10^{-4} (RT)		[36]
	Pulsed Laser Deposition – annealed at 800 °C	$f_{laser\ pulse}$= 10 Hz; 7.5 $J.cm^{-2}$; 7700 shots; thickness ~1 µm; annealing 800 °C	1.8×10^{-4} (RT)		[36]
$Na_3Zr_2Si_2PO_{12}$ - NASICON	Solid-state reaction	**(1)** Calcined at 1100 °C for 12 h; **(2)** ball milling at 150 rpm for 18 h	0.2 (50 °C)	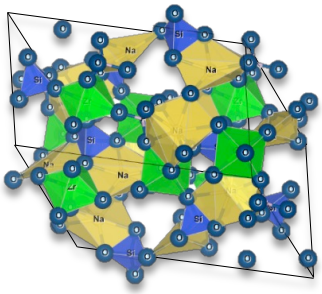	[37]
	Solid-state reaction (nano precursors)	1230 °C for 40h	1.2 (RT)		[38]
	Co-precipitation	• Solution 1: $NaOH + NH_4H_2PO_4$ stirred with deionized water for 1h at 70 °C; • Solution 2: $Zr(OC_3H_7)_4$ diluted with 1-propanol; Solution 1 dipped on solution 2, forming a precipitate	1.7 (25 °C)		[39]
	Spark Plasma Sintering	Powders were placed into a 10 mm graphite die; 1000 A; 62 MPa; 100 °C.min^{-1}; 900-1200 °C - 30min;	1.8 (RT)		[40]

2.2. Synthesis methods

When different methods prepare an electrolyte, the final characteristics of the electrolyte differ; this occurs because the preparation methods influence the crystal structure of the solid, the structural disorder, and mobile ion distributions, resulting in significantly different values of ionic conductivities in **Table 1**.

Mechanochemical methods, specifically ball-milling **(Figure 3 (a))**, are commonly linked to forming distinct phases, such as amorphous and/or nanocrystalline structures. On the other hand, when solid-state electrolytes SSEs are annealed at elevated temperatures, they tend to exhibit thermodynamically stable phases.

The vapor-phase deposition is widely used to prepare inorganic SSE membranes for thin-film batteries. These methods involve the formation of the vapor phases of the reactants, subsequent nucleation, and product growth on substrates, allowing the achievement of a homogeneous mix of the reactants on a molecular or atomic level. The gas-phase techniques involve deposition methods such as Pulse Laser Deposition PLD **(Figure 3 (b)),** Atomic Layer Deposition ALD, and Chemical Vapor Deposition CVD **(Figure 3 (c)).**

To secure a dominant role in the industry, SSEs must be easily reproducible, and the cost of fabrication must be low. Techniques like ball milling don't allow reproducibility, and vapor-phase deposition techniques are usually expensive. Recently, a new technique only compatible with some types of electrolytes has been developed; this process is a water-mediated synthesis **(Figure 3 (d))** with great potential for mass production due to the relatively low cost of implementation.

Ball-Milling. High-energy methods are among the favorite synthesis methods to produce inorganic solid electrolytes. This technique generates chemical reactions through a force caused by the collision between the milling balls and the reactants, **Figure 3 (a)**. During this process, the reagents are pulverized and mixed, combined with the formation of point and lattice defects. The mechanochemical method's main advantage is its ability to overcome the diffusion limitation in the solid-state reaction without the necessity to add bulk solvents or exposure to heat. This technique was first introduced by Hayashi *et al.* [55] in 2001 and has since been a promising technique to achieve improved ionic conductivity; the strain during ball-milling increases the activation volume, allowing ion hopping.

Additionally, ball-milling can induce defects in inorganic solid electrolytes, enhancing their ionic transport. However, the results obtained by this technique don't

show satisfactory reproducibility. Even using the same equipment, the ball milling process is influenced by chamber atmosphere, ball milling time, rotation speed, and ball size; this represents a significant setback for using this technique for mass-scale production.

Pulsed Laser Deposition. Pulse Laser deposition (PLD) is a process where a high-energy laser beam is used to ablate a target material onto a substrate inside a vacuum chamber. The target is heated and vaporized by the energy of the laser. The vapor absorbs energy and is transformed into plasma with high energy. The atoms in the plasma collide and recondense on the substrate and form a thin film **Figure 3 (b)**. The main advantage of this technique is that the highly focused laser can effectively deliver energy to a localized area and ensure the evaporation of the target materials even with very low vapor pressure [36]. Additionally, the PLD technique exhibits a high deposition rate and accurate control of film growth precursor. In contrast to the conventional evaporation techniques, it is hard to control the chemical composition of the thin film because of possible precursor loss due to volatilization.

Chemical Vapor Deposition. Chemical vapor deposition CVD is a process that involves the reaction of a volatile precursor previously injected into a chamber, typically under a vacuum. The chamber is heated to a temperature that causes the precursor gas to react or break down into the desired coating and bond to the material surface. The process begins with the introduction of the reactants to the deposit region. After this, the reactants are transported by diffusion from the main gas stream through the boundary layer to the substrate surface, where the absorption of the reactants will occur. When this process starts, surface reactions and decomposition take place. The CVD process ends with the forced convection transport of the by-products away from the deposition region, **Figure 3 (c)**. The CVD process involves highly complex flow dynamics since gases flow into the reactor, reacting, and then the by-products are exhausted.

The CVD is a relatively new technique for fabricating thin film batteries [56]. The main advantage of CVD is the dependence on relatively low kinetic energy particles and the multitude of chemistries available to perform the deposition.

Water-Mediated Synthesis. To achieve mass-scale production of solid-state electrolytes, it is essential to utilize cost-effective synthesis methods. However, many previously discussed methods are expensive and impractical for large-scale manufacturing. A recent liquid or wet-phase synthesis development provides a potential solution. When applied to sulfide-based electrolytes, this method, also known as wet chemical synthesis, can be executed in two ways: **(1)** generating a precipitate by mixing

a precursor with a solvent or **(2)** dissolving the precursor to create a homogeneous solution [57]. Both approaches are followed by solvent evaporation to obtain the final solid-state electrolyte. However, these methods have limitations in terms of time consumption and solvent compatibility. Considering environmental concerns, water seems to be the ideal solvent due to its favorable properties. Unfortunately, it can only be employed in moisture-stable electrolytes, which excludes most sulfide electrolytes. Nevertheless, despite the incompatibility of sulfide-electrolytes with water-mediated synthesis, various oxyhalides, and halide electrolytes have demonstrated compatibility with this method, as shown in **Figure 3 (d).** Moreover, these electrolytes exhibit exceptional ionic conductivities, further emphasizing their potential for practical applications. For example, Li_3InCl_6, when synthesized via solid-state synthesis, shows an ionic conductivity of 1.49 $mS.cm^{-1}$ [58] (**Halide Electrolytes**). However, when prepared via water-mediated synthesis, the ionic conductivity increases up to 2.04 $mS.cm^{-1}$ [22] (**Halide Electrolytes**). However, the most significant advantage of this method is the increased humidity resistance when prepared by water-mediated synthesis.

2.3. Overview of different types of Inorganic Solid-state electrolytes

Inorganic solid-state electrolytes can be divided into different kinds of structures or element-containing compounds that summarize the characteristics of the most studied families of electrolytes, such as Li/Na-SICON, argyrodite, garnet, and perovskite structures.

The LISICON and argyrodite structures are usually found in sulfide-and-oxide-based electrolytes. The general structure of LISICON (Lithium Super Ionic Conductor) materials is based on the NASICON (sodium superionic conductor) crystal structure. LISICON belongs to a broader family of solid-state materials with the general chemical formula $A_{11}B_2Ch_{12}$, where A represents alkali metal cations (e.g., Li, Na, K), B represents metal cations (e.g., Ge, Ti, Zr), and Ch represents chalcogen anions (e.g., O, S, Se). The crystal structure of LISICON can be described as a three-dimensional framework of corner-sharing polyhedral units. The B cations are surrounded by oxygen (or other chalcogen) anions, forming a B-centered polyhedron. These polyhedra are connected by shared oxygen (or chalcogen) ions to create a 3D network. Within this framework, the A cations (e.g., Li) occupy the interstitial spaces between the B-centered polyhedra. Lithium ions in these interstitial sites allow for efficient lithium-ion transport, making LISICON materials promising candidates for solid-state electrolytes.

The first LISICON electrolyte report can be traced back to 1980 when $Li_{3.6}Ge_{0.6}V_{0.4}O_4$ was successfully synthesized, resulting in an ionic conductivity of approximately 0.04 $mS.cm^{-1}$ at room temperature RT [59]. The crystalline structure of oxide-based LISICON electrolytes commonly resembles Li_4SiO_4 (monoclinic, P21/m space group) or γ-Li_3PO_4 (orthorhombic, Pnma space group) structures. These structures consist of tetrahedral units based on XO_4 (where X can be P, Al, Si, Ge, S, or Ti) and Li-O polyhedral units. For LISICON-oxide-based electrolytes, the highest reported value of ionic conductivity is approximately 0.9 $mS.cm^{-1}$ at 27 °C, for the $Li_4Al_{1/3}Si_{1/6}Ge_{1/6}P_{1/3}O_4$ electrolyte [60]. LISICON-oxide-based electrolytes are associated with relatively low ionic conductivity at RT, a significant limitation for employing these electrolytes in all-solid-state batteries.

Thio-LISICON solid-state electrolytes are derived from LISICON-oxide electrolytes by substituting the O^{2-} anion with the S^{2-}. This substitution improved the ionic conductivity of the LISICON electrolytes up to 12 $mS.cm^{-1}$ at RT for the $Li_{10}GeP_2S_{12}$ LGPS [13], **Figure 1**, which meets the demands of commercial all-solid-state-batteries (ASSBs). Albeit the thio-LISICON presents higher ionic conductivities due to the presence of sulfur in the backbone, this same element leads to a decrease in the overall stability of the electrolyte towards moisture.

Argyrodites are a group of compounds with the general chemical formula $A_{7-x}BCh_{6-x}Hal_x$, where A represents alkali metal cations (e.g., Li, Na, K), B is P or As, Ch is a chalcogen (e.g., S, Se) and Hal is Cl, Br, or I. In the argyrodite structure, the Ch chalcogens share the corners of the cube with the Hal halides; the P or As form a B-centered polyhedron with the Ch at the corners. The A cations are positioned at the cube's center, and the tetrahedral voids within the B-centered polyhedron. This crystal structure creates a three-dimensional network of corner-sharing polyhedral, providing pathways for efficient ion transport, particularly for lithium ions. Argyrodites are known for their high lithium-ion conductivity**, Section 2.3.1, Figure 4**, making them promising candidates for solid-state electrolytes in advanced lithium-ion batteries and other electrochemical devices.

Among the argyrodite-type sulfur electrolytes, Li_6PS_5Hal (Hal = Cl, Br, I) stand out as the most extensively studied and promising [61]. Substituting the halogen element between Cl, Br, and I lead to an evident variation in lattice site disorder, increasing the unit cell volume and the intra-cage and inter-cage jump distance [62].

In this thesis, our primary focus is on the chloride anion-based electrolytes. This choice is based on the following reasons: **(1)** fluorine is the most electronegative element, resulting in a strong bond with Li ions and further impeding fast Li-ion conduction; at the same time, as they have a small radius, the lattice volume is smaller, further hindering

the Li^+ conductivity; **(2)** Bromine is toxic, and as the world seeks safer and more environmentally friendly options, it has been disregarded; **(3)** iodine, while expected to yield better results, has limitations due to its photosensitivity, which poses challenges for mass-scale production applicability. Considering these factors, chloride anion-based electrolytes are a more favorable option, as they offer better Li-ion conduction while addressing the concerns associated with fluorine, bromine, and iodine.

Regarding Li_6PS_5Cl, the highest value of ionic conductivity reported for this electrolyte is 4.96 $mS.cm^{-1}$ at 26 °C when prepared via solid-state reaction [31]. The most common preparation method for this electrolyte is ball-milling [63]; however, several groups adopted a multiple-step synthesis that included both annealing and ball-milling to improve the crystallinity and ionic conductivity. The ionic conductivity values obtained for different synthesis methods are presented in **Table 1**. The argyrodite-sulfur electrolytes display high ionic conductivity, **Figure 1**. However, the presence of sulfur in the backbone leads to decreased stability toward moisture [64]. In 2010, it was reported the first synthesis of oxide-based argyrodites Li_6PO_5Hal [65]. The ionic conductivity of the oxygen-based Li_6PO_5Cl electrolyte reported at RT was 10^{-6} $mS.cm^{-1}$, a value quite inferior to its sulfide-argyrodite counterpart.

The garnet structure is observed in oxide-based electrolytes, exhibiting exceptional stability when in contact with lithium metal and demonstrating satisfactory ionic conductivity. Garnet structures are commonly found in orthosilicates, characterized by the general formula $A_3^{II}B_2^{III}(SiO_4)_3$ (A = Ca, Mg; B = Al, Cr, Fe) where A, B, and Si cations occupy the eight, six, and four coordination sites, respectively. These structures typically crystallize in a cubic arrangement with an Ia-3d space group. Among garnet-type electrolytes, there are four main subtypes: Li_3, Li_5, Li_6, and Li_7. Notably, the ionic conductivity of garnets containing lithium demonstrates a substantial exponential growth as the Li content expands throughout a wide range. Among all the famous Garnet-type electrolytes, the one that has emerged as the most promising is LLZO, $Li_7La_3Zr_2O_{12}$ [66]. This electrolyte has a high lithium-ion conductivity of 0.3 – 0.5 $mS.cm^{-1}$ at 25 °C [34], good thermal and chemical stability against reactions with prospective electrode materials, low cost of production, and environmental availability. On the downside, the total ionic conductivity in this electrolyte is highly sensitive to grain boundaries. These structures tend to reduce the ionic conductivity of the electrolyte, introducing the need for careful control over the high-temperature sintering process to reduce grain boundaries and, therefore, achieve high ionic densities and conductivities.

The general structure of NASICON (Sodium Super Ionic Conductor) materials is based on a three-dimensional framework of corner-sharing polyhedral units. NASICON is a family of solid-state materials with the general chemical formula $AM_2(PO_4)_3$, where A represents monovalent cations (e.g., Li, Na) and M represents a combination of divalent and trivalent cations (e.g., Sn, Ti, Zr).

In the NASICON crystal structure, the M cations are located at the corners of a distorted octahedron, forming an M-centered polyhedron. The PO_4 tetrahedral units (phosphate anions) are connected to these M-centered polyhedral, creating a three-dimensional network. The A cations are positioned in the interstitial sites between these polyhedral units.

The general structure of perovskites is based on a three-dimensional framework of corner-sharing polyhedral units. Perovskites are a family of materials with the general chemical formula ABX_3, where A (e.g., Ba) and B (e.g., Ti) are cations, and X is an anion, for example, oxygen; the structure is cubic and Pm-3m. In the perovskite crystal structure, the X atoms (e.g., O) are located at the corners of an octahedron, forming a BO_6 polyhedral unit. The B cations are located at the center of the octahedron. The A cations are positioned in the center of the cube. The arrangement of these polyhedral units creates a three-dimensional network with a cubic symmetry. The general formula ABX_3 signifies that six X anions surround each B cation, and each A cation is coordinated to six X anions in an octahedral arrangement.

Perovskites exhibit a wide range of properties and have applications in various fields, including solid-state materials, electronics, energy conversion and storage (e.g., photovoltaics, fuel cells), and catalysis. The versatility of perovskite materials branches from the ability to modify the A, B, and X elements, which can result in diverse electronic, magnetic, and optical properties.

The NASICON and the perovskite structure have lower ionic conductivity than previously mentioned electrolyte types and are still highly subjective to grain boundary issues. The NASICON electrolytes, discovered in 1976 by Goodenough et al. [67], have a general formula of $AM_2(PO_4)_3$, where A = Li, Na and M = Ge, Zr, Ti, and may be doped with Al. Generally, the ionic conductivity is higher when the A element is sodium Na rather than lithium Li. For instance, $LiGe_2(PO_4)_3$ - LGP exhibited an ionic conductivity of approximately 10^{-4} $mS.cm^{-1}$. Adding aluminum as a dopant in $Li_{1.5}Al_{0.5}Ge_{1.5}(PO_4)_3$ - LAGP significantly improved the ionic conductivity of this electrolyte, with a maximum achieved value of 0.58 $mS.cm^{-1}$ at RT [68]. Comparatively, the LAGP electrolyte showed a remarkable enhancement in ionic conductivity, surpassing LGP by four orders of

magnitude. Considering the case of a sodium conducting ion, $Na_{1+x}Zr_2Si_xP_{3-x}O_{12}$, the highest ionic conductivity obtained is for x = 2, $Na_3Zr_2PSi_2O_{12}$ with an ionic conductivity of approximately 1.13 $mS.cm^{-1}$ at RT [69]. However, several doping strategies have been employed to achieve higher ionic conductivities: **(1)** doping with potassium ion, which demonstrated for $Na_{2.303}K_{0.099}Zr_2Si_{1.880}P_{1.106}O_{12}$ an ionic conductivity of 0.8 $mS.cm^{-1}$ at RT [70]; **(2)** doping with Ge, $Na_{3.125}Zr_{1.75}Sc_{0.125}Ge_{0.125}Si_2PO_{12}$, resulted in total ionic conductivity 4.6 $mS.cm^{-1}$ [71]; **(3)** doping with Sc, $Na_{3.4}Zr_{1.6}Sc_{0.4}Si_2PO_{12}$ renders an RT ionic conductivity of 4.0 $mS.cm^{-1}$ [69].

As for perovskite electrolytes, one notable example is $Li_{3x}La_{(2/3)-x}TiO_3$ LLTO. In 1987, Belous et al. [72] synthesized the LLTO perovskite for $0.04 \leq x \leq 0.17$ for the first time. In the LLTO solid electrolytes' structure, the Li-ion occupies the A-site resulting in a lower activation energy. This electrolyte shows several advantages: **(1)** large ionic transference numbers, **(2)** superior chemical and **(3)** thermal stabilities in air, and **(4)** environmentally friendly character without any release of toxic gases during decomposition reactions. However, the significant grain boundary resistance reduces the total ionic conductivity of this electrolyte to < 0.01 $mS.cm^{-1}$ at RT. LLTO is also very unstable when in the presence of Li metal. For potentials below -1.7 V vs. Li^0 (SHE), LLTO is reduced, and Li can be intercalated in it, which causes the reduction of Ti^{4+} and enhances the electrical conductivity of $Li_{0.29}La_{0.57}TiO_3$ LLTO [73]. The latter observation indicates that the lowest energy of the conduction band is approximately -3.1 eV (E = 0 eV, electrons at rest in vacuum). The calculations in **Figure 2 (a)** and **Figure 2 (b)** demonstrate that the lowest energy of the conduction band for LLTO is -3.6 eV, which is in good agreement with the experimental result, considering this value results from two different simulations: **(1)** the average potentials from a simulated surface of the electrolyte; **(2)** the band structure from the bulk electrolyte [74]. Moreover, herein, we simulated $Li_2La_2Ti_3O_{10}$ LLTO, a perovskite and stable against Li^0.

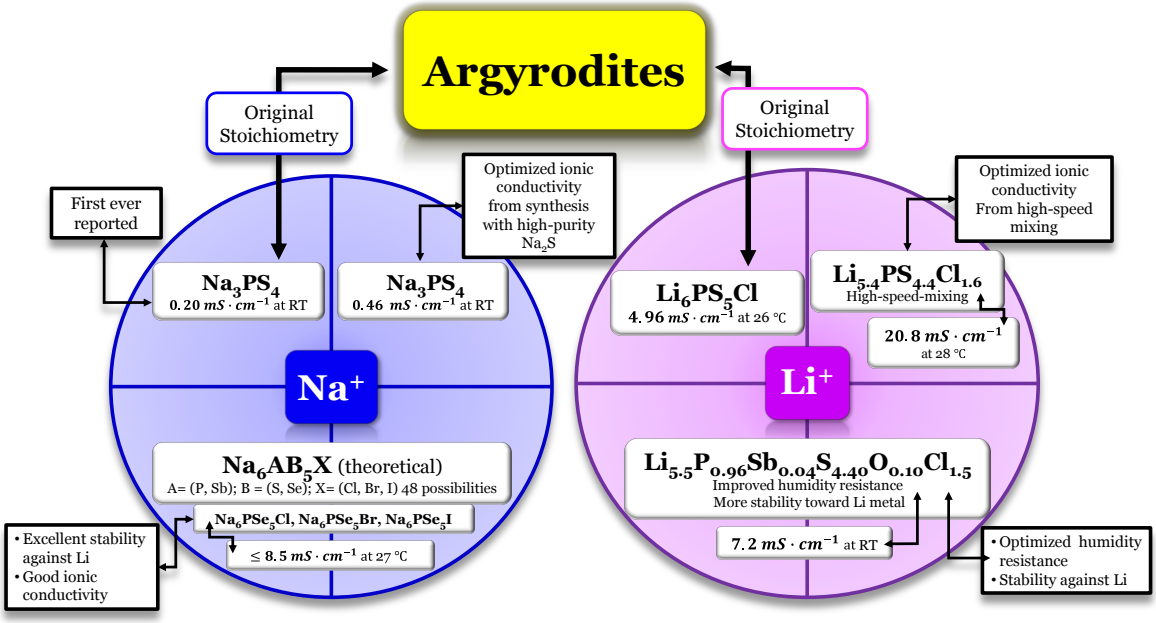

Figure 4. Argyrodites summary scheme, Li_6PS_5Cl [31]; $Li_{5.4}PS_{4.4}Cl_{1.6}$ [10]; $Li_{5.5}P_{0.96}Sb_{0.04}S_{4.40}O_{0.10}Cl_{1.5}$ [75]; Na_3PS_4[76], [77], and Na_6AB_5X, A = (P, Sb), B = (S, Se), X = (Cl, Br, I) [78].

2.3.1. Argyrodite Electrolytes

Argyrodite – structure electrolytes, are derived from the Ag_8GeS_6 mineral, and have been reported both in sulfide and oxide-based electrolytes. Considering the great interest in the mobility of Li^+ ions in solids, it was surprising that there were only a few reports of experimental work with the corresponding crystalline Li analogues, and none of these appear mention the argyrodite connection. In the Li-argyrodite family compounds are described by the general formula $Li_{7+x-y}M^{IV}_xM^{V}_{1-x}Ch_{6-y}Hal_y$ (M^{IV}= Si, Ge, Sn; M^{V} = P, Sb; Ch = O, S, Se; Hal = Cl, Br, I, BH_4; $0 \leq x \leq 1$; $0 \leq y \leq 2$) [79]. In 2008, Deiseroth *et al.* [80] reported the first Li_6PS_5Hal, Hal = Cl, Br, I argyrodite electrolyte, showcasing its ionic conductivity in the range of 1 to 10 $mS.cm^{-1}$ at RT. Since then, numerous reports have emerged regarding this stoichiometry, with the highest ionic conductivity obtained for Li_6PS_5Cl (LPSCl), being 4.96 $mS.cm^{-1}$ at 26.2 °C, when prepared via solid-state reaction [31]. However, this is not the only stoichiometry configuration possible for a lithium argyrodite (**Figure 4**).

In a recent study by Chen *et al.* [10] the synthesis of a Li-argyrodite electrolyte, $Li_{5.4}PS_{4.4}Cl_{1.6}$, was made using high-speed mixing. This electrolyte demonstrated an astonishingly high ionic conductivity of 20.2 $mS.cm^{-1}$ at 28 °C, **Figure 1** and **Figure 4**, which is the highest reported value for a lithium argyrodite so far. For the standard high-energy ball milling, the highest reported ionic conductivity value is 9.4 $mS.cm^{-1}$ [14]. Also, for $Li_{5.4}PS_{4.4}Cl_{1.6}$ **Figure 1**, Chen et al.'s study [26] introduced a cost-effective and

efficient method known as *high-speed mixing,* which utilizes an affordable consumer-grade commercial mixer. The high-speed mixing process enables rapid material mixing, producing more than 500 g per batch of LSPCl solid electrolyte. In contrast, the traditional high-energy ball-milling method is limited to 50 g per batch. Notably, the high-speed mixing technique is both energy-efficient and highly effective.

Using the ultra-high speed mixing preparation process, no obvious grain boundary was observed in the cross-sectional microstructure, which is one of the main factors for the reported high ionic conduction. This presents an effective mixing method for the mass production of $Li_{5.4}PS_{4.4}Cl_{1.6}$ solid electrolyte. Additionally, the authors also reported that an all-solid-state electrolyte cell containing graphite/LPSC-mixing/NMC622 cell delivered an outstanding discharge capacity of 165 $mAh.g^{-1}$ at C/10 and a coulombic efficiency of 82.4%.

Despite the numerous advantages offered by the conventional argyrodite electrolyte, concerns have been raised due to its vulnerability to atmospheric air, as well as its limited structural and electrochemical stabilities. Nevertheless, completely replacing sulfur with oxygen in the argyrodite structure has significantly reduced ionic conductivity [65], indicating that this approach may not be the ideal solution. However, an alternative worth exploring involves doping the argyrodite structure with oxygen (**Figure 4**). This approach appears to combine the best attributes of both sulfur and oxygen, leading to meaningful results [81].

Hwang *et al.* [81] investigated the substitution of oxygen (O) for sulfur (S) in $Li_6PO_xS_{5-x}Br_{0.5}Cl_{0.5}$ SEs to comprehend the underlying mechanisms and improve the stability of these materials. In his study, the author combined first-principles calculations and electrochemical experiments, spanning from bulk to surface models. Moreover, the author developed systematic experimental investigations to explore the impact of O substitution on suppressing/reducing structural decomposition. The materials were synthesized and thoroughly characterized. The goal of doping the sulfide electrolyte with oxygen is to increase the resistance to moisture absorption, delaying phase decomposition. The atomic and electronic structures of sulfide electrolytes were calculated from bulk to surface. The theoretical analysis determined that the introduction of oxygen causes a more noticeable contraction of the lattice constants compared to the substitution of halogen elements. This suggests that replacing sulfur (S) with oxygen (O) significantly impacts the chemical bonding between isovalent chalcogens, leading to a stronger electrostatic bonding between O and Li ions. This strong bonding is closely associated with structural stability. Following this hypothesis, the authors studied the

effect of the introduction of oxygen in the electrochemical environment of the electrolyte. The latter realization was made by considering that oxygen has a superior tendency to electronegativity than sulfur.

A new study by Wei et al. [75] described the synthesis of a chlorine-rich lithium argyrodite, $Li_{5.5}P_{0.96}Sb_{0.04}S_{4.40}O_{0.10}Cl_{1.5}$, which demonstrated enhanced stability in the presence of air and lithium-ion stability (**Figure 1** and **Figure 4**). The reported ionic conductivity of this compound is 7.2 $mS.cm^{-1}$ at RT, slightly lower than that of the $Li_{5.5}PS_{4.5}Cl_{1.5}$ electrolyte that exhibits 9.4 $mS.cm^{-1}$ at RT. However, it was observed that when both electrolytes were exposed to moisture, the ionic conductivity of $Li_{5.5}PS_{4.5}Cl_{1.5}$ decreased significantly to 1.1 $mS.cm^{-1}$, while the $Li_{5.5}P_{0.96}Sb_{0.04}S_{4.40}O_{0.10}Cl_{1.5}$ electrolyte showed a comparatively higher ionic conductivity of 3.6 $mS.cm^{-1}$. Furthermore, a comparison of the X-ray diffraction (XRD) spectra revealed that the $Li_{5.5}PS_{4.5}Cl_{1.5}$ electrolyte exhibited weakened diffraction peaks and the presence of various impurity phases when exposed to open air for 20 minutes. In contrast, the $Li_{5.5}P_{0.96}Sb_{0.04}S_{4.40}O_{0.10}Cl_{1.5}$ electrolyte displayed improved stability with fewer impurity phases, indicating its superior moisture resistance compared to the bare $Li_{5.5}PS_{4.5}Cl_{1.5}$ electrolyte. The introduction of the Sb element helped to enhance the stability of the electrolyte towards lithium metal.

The compound known as sulfur argyrodite is commonly found in Li^+-ion conducting electrolytes. However, there have been reports of Na^+-ion argyrodite electrolytes as well (**Figure 4**). In 2012, Hayashi *et al.* [76] reported the synthesis of Na_3PS_4 as a superionic glass-ceramic electrolyte for the first time, displaying an ionic conductivity of 0.2 $mS.cm^{-1}$ at RT. In 2014, the same author reported the synthesis of the same electrolyte with an improvement of the ionic conductivity of 0.46 $mS.cm^{-1}$ at RT [77]. The progress was a result of an optimization during the synthesis mode. The author synthesized Na_3PS_4 in cubic phase directly via mechanical milling using a highly pure Na_2S reagent; with this, the authors could reduce the reaction time necessary to produce the glass ceramic effectively. This glass-ceramic electrolyte was synthesized by milling 75 mol% Na_2S and 25 mol% P_2S_5 for 1.5 hours and subsequent heat treatment at 270 °C for 1 hour, as reported in [76]. This method reduces the reaction time and facilitates the production of glass ceramics. Moreover, in this study, the author also synthesized an all-solid-state cell containing $Na_{15}Sn_4/Na_3PS_4/NaCrO_2$. The cell was tested electrochemically at RT and displayed an average capacity of 60 $mAh.g^{-1}$ of $NaCrO_2$ for 15 cycles.

Following the previous reports in 2016, de Klerk and Wagemaker [82], conducted a study to comprehend the diffusion mechanism in Na_3PS_4 and explore potential ways to

enhance Na^+-ion conductivity. Na_3PS_4 is known to exist in two distinct phases, cubic and tetragonal. However, the differences between these phases are small, the tetragonal phase being tetragonally distorted concerning the cubic phase [82]. The main difference between these two structures lies in the positioning of sodium within the crystal. Regardless, if both phases are synthesized in a similar way, they display similar ionic conductivity. A significant boost in ionic conductivity is observed when transitioning from the crystalline to the glass-ceramic form of the cubic phase, increasing 30 times the ionic conductivity. The introduction of halogen dopants plays a crucial role in enhancing ion conductivity. This effect is attributed to a significant increase in the concentration of Na^+ vacancies, which is vital to microscopic diffusion. The function of temperature is also an essential factor in Na^+-ion diffusion. In this study, the authors [82] conducted molecular dynamics simulations to investigate the effects of lattice parameter increase on the conductivity of cubic $Na_{2.50}PS_4$ and $Na_{2.94}PS_4$ at 252 °C. Considering 1% expansion in lattice parameters, corresponding to a 3 % volume expansion, the conductivity increased 10 % for $Na_{2.94}PS_4$, and 17 % for $Na_{2.50}PS_4$, highlighting the significant impact of lattice expansion on conductivity when temperature is increased.

In 2020, Ouyang et al. [78], conducted research utilizing computational simulations to explore the discovery of halogen-substituted Na^+-argyrodites. In this study, the author gained insights into the necessary conditions to achieve high ionic conductivity in Na^+ argyrodites, **Figure 4**. This investigation focused on the phase stability, electrochemical stability, and ionic conductivity of 48 potential Na-based argyrodites. In the argyrodite formula Na_6ACh_5Hal, A represents a pnictogen atom P or Sb, Ch is typically a chalcogenide atom such as S or Se, and Hal is a halogen element, similar to its Li^+ counterpart (**Figure 4**). Regarding the phase stability, the authors concluded that the formation of the SbS_4 polyanion in Na^+ Argyrodites performs more favorably compared to the PS_4 polyanion. The halogen element Hal had minimal impact on the electrochemical stability or the decomposition phases, considering the established limits imposed by the polyanion and chalcogen elements. The Na^+ argyrodites are generally electrochemically stable within the potential range of 1 - 2 V vs Na/Na^+, which means that the lowest energy of the conduction band of the Na^+ argyrodites varies from $-1.73 \leq E_c(eV) \leq -2.73$ where $E_0 = 0$ eV (-4.44 eV/e = 0 V, SHE) is the energy of the electrons at rest in vacuum. The latter value for the lowest energy of the conduction band is shown in **Figure 2 (a)** to agree with the equivalent value for the Li^+ argyrodite, LPSCl. The previous limits, as already mentioned, are imposed by the pnictogen element, which reduces from +5 to +3 for potentials above the stability window for $E > E_C$ and by the chalcogen element since it oxidizes for values of potentials lower than the stability

window $E < E_V$ [78]. Furthermore, a comparison of stability windows revealed that the Na-Sb-S(Se)-Hal systems have a narrow electrochemical window, whereas the Na-P-S(Se)-Hal systems generally possess a wider electrochemical window [78]. When considering the ionic conductivity, the halogen element has a dominant role since the occupancy of the halogen, especially in a sulfide-based system, deeply affects the ionic conductivity, whereas in selenide-based systems the ionic conductivity remains similar, regardless of the halogen occupancy. The compression effect generated by halogen substitution is less significant in the selenides systems, which generally leads to good ionic conductivity [78]. Ouyang et al. [78] concluded that among the predicted Na^+ argyrodites, the compositions within the Na−P−Se−Hal (Hal = Cl, Br, or I) system demonstrated excellent stability and ionic conductivity.

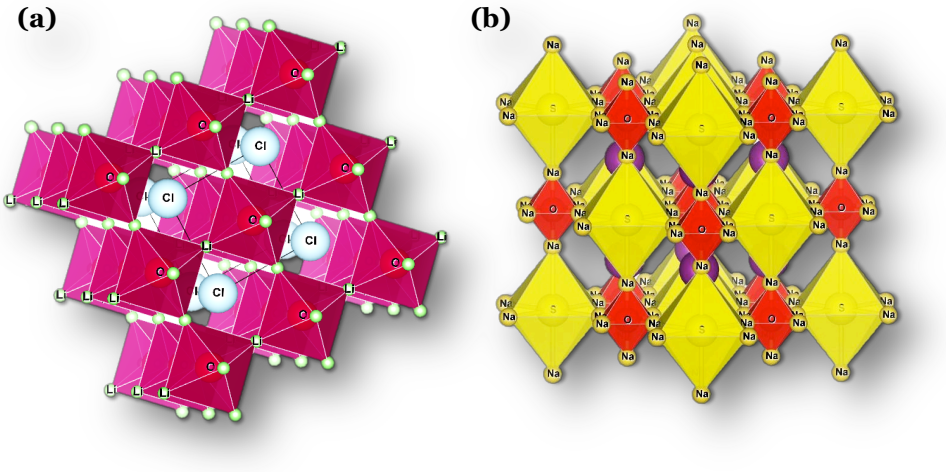

Figure 5. Antiperovskite electrolytes structures: **(a)** Li_3OCl [9]; **(b)** $Li_6SO(BH_4)_2$ [83]; CIF files: [41]–[54].

2.3.2. Antiperovskite Electrolytes

Recently, a new type of structure called antiperovskites has been receiving increased attention in inorganic material research. The antiperovskites have the same structure as the perovskites. However, they adopt a reversed ionic arrangement, which means unique anion-centered units in antiperovskites compared to the conventional cation-centered ones in perovskites. The cation position in the antiperovskite causes significant differences in these structures, providing a distinct local environment for mobile ions and thereby altering their mobility. The first time ionic conductive antiperovskites with X_3BA structures were reported dates to 1960 when Reuter *et al.* [84] reported Ag_3SI compound with Ag^+ as a mobile cation. In 2012, Zhao *et al.* synthesized and designed the first Li^+ conducting X_3BA shape antiperovskites [85]. In the antiperovskite formula X_3BA, X is a cation, and A and B are different-sized anions. The discovery of the ionic conductivity of

Li-rich antiperovskites (LIRAP) was inspired by the high-temperature superionic conductivity of $NaMgF_3$ perovskites. The electronically inverted antiperovskite Li_3OHal (Hal = Cl, Br, I) allowed Li^+ ionic conductivity like the F^- superionic conductivity in $NaMgF_3$. However, the perfect X_3BA antiperovskite structures are considered a disadvantage for ionic conduction due to the lack of intrinsic defects that would work as charge carriers in ionic conduction [86]. A variety of methods for defect engineering, such as mixing, doping, and depletion by doping, for example, with divalent ions such as Ba^{2+}, was proposed theoretically [86]. Following this study, Braga *et al.* [9] reported a series of divalent cation-doped Li_3OCl glass electrolytes, $Li_{3-2x}M_xOCl$ with M= Mg, Ca, Sr, Ba, synthesized by water-mediated synthesis, **Figure 3(d)**, followed by a heat treatment to remove the solvent. These latter electrolytes are not antiperovskites anymore as they are amorphous, disordered materials.

In solids, as explained before, ion conduction occurs by ion hopping from one lattice site to another by vacancy mechanisms, **section 2.1**. The rate of ion transport in a lattice is dictated by diffusivity and concentration of vacancies mediating transport. Glassy materials are usually associated with high ionic conductivity because their open structures facilitate the ionic hoping process.

In the Li_3OCl crystalline allotrope, the antiperovskite structure, the pattern followed is the following: **(1)** the Cl^- occupies the center atom of the cube; **(2)** the center of the octahedral is occupied by the O^{2-}; **(3)** the Li^+ occupies the vertices of the octahedral, making it a Li^+-rich structure, **Figure 5**. Doping this structure with higher valence cations such as Ba^{2+} and Ca^{2+} creates vacancies in the cation sublattice, one per each Ba^{2+} that replaces two Li^+. This lowers the activation energy for Li^+-ion diffusion as the formation of vacancies is unnecessary or assured at synthesis.

Of all the reported electrolytes [9], the one that displayed better results was the one doped with Ba^{2+} cation; Barium ion has a larger doping ion radius, resulting in a higher anisotropy of the lattice, which favors a higher ionic conductivity. The glassy electrolyte $Li_{2.99}Ba_{0.005}OCl$ obtained a ground-breaking ionic conductivity of 25 $mS.cm^{-1}$ at 25 °C. After this study, Braga *et al.* synthesized the analogous Na^+ and K^+ electrolytes [8]. The $Na_{2.99}Ba_{0.005}OCl$ and $K_{2.99}Ba_{0.005}OCl$ electrolytes, synthesized as glass materials, displayed an astonishing ionic conductivity of 133 $mS.cm^{-1}$ and 155 $mS.cm^{-1}$ at RT. The high ionic conductivity, **Figure 1**, reported in these electrolytes is attributed to their ferroelectricity driven by the mobility of the ions and the electrolytes' semiconductor nature, **Figure 2(b)**, with surface-protected states that contribute to the fast polarization of the electrolytes. These concepts will be briefly discussed in detail in **Section 2.4.**

Recently, a structural modification on Li^+/Na^+ antiperovskite electrolytes has been proposed with the introduction of large polyatomic units to replace single ions on crystallographic sites. In 2017, Fang *et al.* [87] developed a simulation that allowed them to propose a new Li^+ antiperovskite structure composed of BH_4^- polyatomic ions in A-sites (i.e., $Li_3O(BH_4)$). BH_4^- is commonly known as a super-halogen, which has been suggested to replace halogen ions due to their similar chemistry but stronger electron affinity when compared to halogens. In 2019, Sun *et al.* [16] synthesized a sodium electrolyte containing BH_4^- polyatomic ions into X_3BA-type antiperovskite structure for the first time, $Na_3O(BH_4)$ from a solid reaction between Na_2O and $NaBH_4$ mixtures. This material was identified as having an antiperovskite structure and exhibiting an ionic conductivity of 4.4 $mS.cm^{-1}$ at RT and additionally displayed a low activation energy of 0.25 eV. Since the first synthesis reported for this electrolyte, other attempts to synthesize this double antiperovskite have been performed. In 2020, Ahiavi *et al.* [88] reported the mechanochemical synthesis of the $Na_3O(BH_4)$ electrolyte; however, the reported ionic conductivity was seven orders of magnitude inferior to the one reported by Sun *et al*.[16] . The author explained that the hot-pressing pellets method used in [16] could alleviate the effects of blocking grain boundary, improving the ionic conductivity. Further research is still necessary to determine which synthesis method enhances the characteristics and nature of this electrolyte.

Recently Tsai *et al.* reported the synthesis of double paddle-wheel sodium amide borohydride $Na_{3-x}O_{1-x}(NH_2)_x(BH_4)$ [89]. The electrolyte contains two clusters of anions, the super halogen BH_4^- and the amide cluster anion NH_2^-. Antiperovskites offer an appealing model system for studying paddle-wheel effects. They can incorporate various ionic substitutions, including multiple cluster anions. This characteristic makes them highly versatile for investigating and understanding the paddle-wheel phenomenon. The *paddle-wheel* effect refers to the correlated rotations of cluster anions, enabling easier cation translation with reduced energy barriers and thereby enhancing cation mobility. Antiperovskites are appealing for studying paddle-wheel effects due to their ability to accommodate a wide range of ionic substitutions, including multiple cluster anions.

The $Na_3O(BH_4)$ electrolyte already discussed corresponds to a single paddle wheel system, whereas the $Na_{3-x}O_{1-x}(NH_2)_x(BH_4)$ corresponds to a double paddle wheel system. The authors verified [89] that for x = 1 $Na_2(NH_2)BH_4$ has a low activation energy of 0.268 eV, and when x = 0.5, the ionic conductivity is a hundred times greater than the extrapolated conductivity at x = 1.

Another common structural modification performed on X_3BA antiperovskite is the formation of double antiperovskites. Islam *et al.* [83], reported the first synthesis of a

super-halogen Li-rich double antiperovskite $Li_6OS(BH_4)_2$ as a solid electrolyte. The synthesis consisted of a 3-step process starting with ball milling and liquid phase process, followed by heat treatment at 380 – 400 °C and water removal under a high vacuum to promote the creation of the $Li_6OS(BH_4)_2$ product, $Li_2O + Li_2S + 2Li(BH_4) \rightarrow Li_6OS(BH_4)_2$ [83], [90]. In the study [83], the band gap of the electrolyte was determined to be 4.03 eV. Furthermore, a symmetric cell was fabricated containing Li/$Li_6OS(BH_4)_2$/Li; this cell is reported to have a long cyclic stability of about 3000 h at 60 μA.cm^{-2} current density, even though the increment of the current density seems to reduce the cyclic stability. The crystal structure of $Li_6SO(BH_4)$ has been found to stabilize in the cubic Fm-3m phase [83] which is consistent with the antiperovskite structures of $Li_3O(BH_4)$ and $Li_3S(BH_4)$, but unlike Li_3OCl whose cubic crystalline structure belongs to the Pm-3m space group. Moreover, this electrolyte exhibits exceptional mechanical stability, with a bulk modulus of 128.5 GPa. The combination of these properties renders this double perovskite suitable for ensuring a safe operation in all-solid-state ASS technologies.

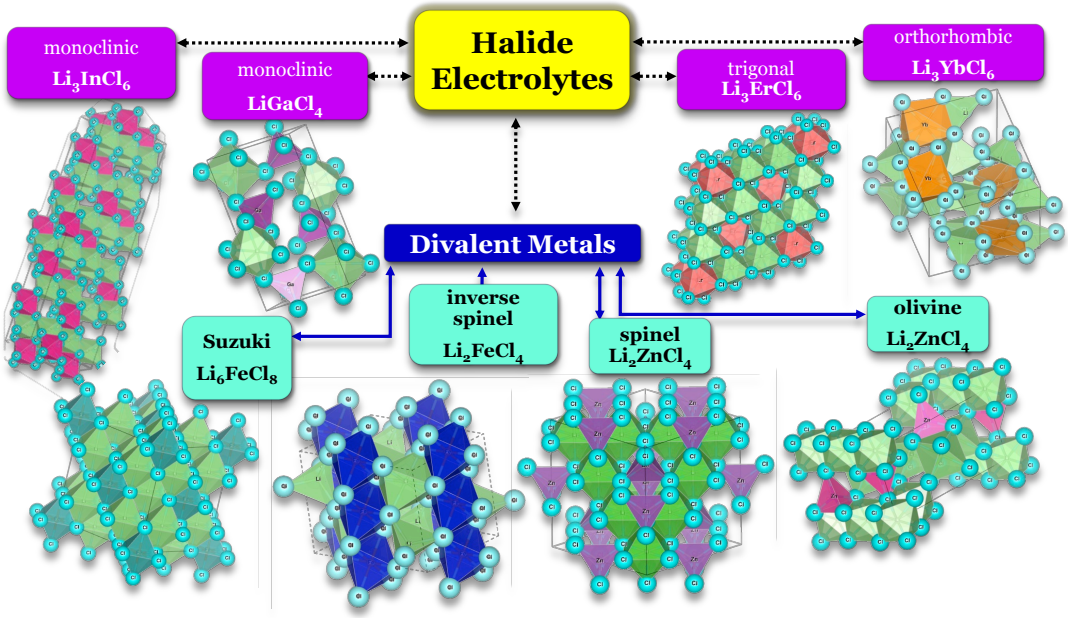

Figure 6. Halide electrolytes Li_xMHal_y, where M = Ga, In, Er, Yb or divalent metals Fe, Zn and Hal is a halogen atom Hal = F, Cl, Br, I. Li_3InCl_6 [22], $LiGaCl_4$ [91], $LiErCl_6$ [28], Li_3YbCl_6[92], Li_6FeCl_8 [93], Li_2FeCl_4 [94], Li_2ZnCl_4 [95]. CIF files: [41]–[54].

2.3.3. Halide Electrolytes

Classifying inorganic electrolytes considering the dominant element is also possible. Sulfide and oxide electrolytes are the most studied; however, several challenges must be considered before their employment in ASSB. The stability of oxide electrolytes in the presence of air and their excellent electrochemical and oxidation stability are noteworthy. However, they suffer from poor ionic contact with electrode materials and cannot prevent

the infiltration of liquids or polymer electrolytes [96]. On the other hand, sulfide electrolytes offer a significant advantage related to their high Li^+-ion conductivity, surpassing even that of liquid electrolytes (**Figure 1**). Nevertheless, these electrolytes are highly susceptible to moisture, leading to detrimental hydrolysis and the release of toxic H_2S. This drawback poses a significant obstacle to the widespread use of sulfide electrolytes in large-scale applications.

To address these challenges, a new class of solid electrolytes containing halogen elements has emerged as a promising alternative. Halide electrolytes capitalize on the unique properties of halogen elements compared to elements like S and O. The monovalent halogen anion exhibits a weaker interaction with Li ions than the divalent S and O, resulting in faster Li-ion conduction. Moreover, the larger radius of halogen anions leads to longer ionic bonds and increased polarizability in the electrolytes, facilitating the migration and plasticity of Li^+-ions [83], [97].

Most halide electrolytes show a general formula Li_aMHal_b where M = Y, Er, Yb, In… and *Hal* = F, Cl, Br, and I. In this subsection, the analysis is mainly focused on electrolytes based on chloride ions as the halogen element. This path was chosen considering several factors already explained in this section's introduction.

Selecting the right central element M is fundamental to successfully designing halide SSEs. Halide electrolytes can be divided in three classes, considering the central element: **(1)** Group 3, **Li_3YCl_6** [27], Li_3ErCl_6 [28], **and Li_3YbCl_6** [92]; **(2)** Group 13, $LiAlCl_4$ [98], $LiGaCl_4$[91]**, and Li_3InCl_6** [22]; **(3)** Divalent metals: **(1)** Li_2ZnCl_4 normal spinel structure at RT [95]; **(2)** Li_2ZnCl_4 olivine structures [95]; **(3)** Li_2FeCl_4 inverse spinel structure [94], **(4)** Li_6FeCl_8 Suzuki structure [93], **Figure 6**. Considering the group 3 and 13 of halogen electrolytes, it is possible to highlight three structures: **(1)** orthorhombic $(Pna2_1)$, **(2)** monoclinic $(P12_1/c1)$, and **(3)** trigonal $(P321)$. The trigonal and orthorhombic structures are based on the hexagonal closed-packed (hcp) anion arrangement, and the monoclinic structure is based on the cubic closed-packed (ccp) anion arrangement, respectively. The ccp structures are usually found in relatively large anionic compounds, such as Cl^- and Br^-, or relatively smaller metal cations. Regarding the divalent metal electrolytes, the reported structures are: **(1)** olivine, **(2)** spinel, **(3)** spinel inverse, and **(4)** Suzuki, however, these structures are usually associated with lower ionic conductivity electrolytes.

The first-time ionic conduction was detected on a lithium halide electrolyte was in 1930 with the synthesis LiHal (Hal = F, Cl, Br, I) [99]. However, the electrolytes had low ionic conductivities, with the maximum being 0.001 mS.cm^{-1}, at RT [99]. Only in 2018, this class of electrolytes gained the interest of the scientific community when for the first time Tetsuya Asano *et al.* [27] mechanochemically synthesized Li_3YCl_6 LYC using a stochiometric mixture of LiCl and YCl_3. LYC electrolyte consists of a hexagonal close-packed (hcp)-like anion arrangement structure, where yttrium resides at the octahedral sites, and yttrium halides display high stability octahedrons YX_6^{3-}. The ionic conductivity of the LYC electrolyte is 0.51 mS.cm^{-1} at RT. The previous conductivity was found to be a revelation since it was observed in a close-packed anion sublattice material; the latter varies from the source of high Li^+-ion conductivity found for sulfide or oxide lithium-ion conductors. The electronic conductivity of LYC is 2.8×10^{-6} mS.cm^{-1}**,** which corresponds to the upper characteristic values of electronic conductivities of an insulator [27] and agrees with our own data for the band gap in Figure 2**(a).** The activation energy was determined to be of 0.40 eV [27]. In 2021, Schlem Romam *et al.* [100] developed a study to assess the lithium sub-structure in lithium conducting halides via temperature-dependent neutron diffraction of the LYC electrolyte. The author considered two different synthesis methods in this study: ball milling and ampule synthesis. It was verified that for the LYC, the mechanochemical synthesis led to a local structure distortion, therefore improving the ionic conductivity. Large disorders motivated by a frustrated energy landscape enhance ionic transport. The disorder in the LYC electrolyte affects the polyhedral volumes of Li^+ and their directional thermal amplitude. Sendek *et al.* [101] performed a DFT simulation guided by a machine learning-based approach to find new fast ionic conductors. This study concluded that Li_3ErCl_6 was an acceptable candidate to achieve good ionic conductivity and was expected to demonstrate an ionic conductivity of 3 mS.cm^{-1} at 25 °C. However, when synthesized via ball milling and annealing, this electrolyte only displayed an RT ionic conductivity of 0.3 and 0.02 mS.cm^{-1}, respectively [28]. This electrolyte displays a trigonal structure $P\bar{3}m1$,**Figure 1** and **Figure 2**. Similarly, to what was reported for the LYC electrolyte, the ionic conductivity is reduced with increasing crystallinity during subsequent annealing processes [101].

Of all the halide electrolytes, the one that showed a higher conductivity at RT was Li_3InCl_6. This electrolyte was first synthesized by a mechanochemical method in 2019 by Li *et al.* [58], which obtained an ionic conductivity of 1.49 mS.cm^{-1}, surpassing all its predecessors. Additionally, this electrolyte exhibited good stability toward conventional oxide cathode materials and good stability in air. The breakthrough of this electrolyte study arose when Li *et al.* [58] proposed a water-mediated synthesis technique to

prepare Li_3InCl_6 [22] **Figure 3 (d).** The obtained RT ionic conductivity was 2.04 mS.cm^{-1}, **Figure 1**.

All the previously reported halide electrolytes have a setback to mass production; the middle element is usually a rare earth metal, leading to high production costs and compromising the commercialization of halide-based solid-state batteries.

In 2021, Kwak *et al.* reported the first cost-effective halide SSE, Li_2ZrCl_6 [26]. This electrolyte was prepared via heat treatment (HT) and ball milling (BM) **Figure 3 (a)**. The use of different synthesis methods introduced considerable variations in the crystal structure and ionic conductivity. When prepared by heat treatment, the electrolyte presented a ccp monoclinic structure with poor Li^+ conduction 0.006 mS.cm^{-1} at 30 °C. When it was prepared by ball milling, it presented an hcp structure with a Li-ion conduction of 0.4 mS.cm^{-1} at 30 °C. These results are atypical in the halide electrolyte world; the monoclinic structure is usually associated with fast ionic conduction, for example, in the Li_3InCl_6 electrolyte. Zirconium is an abundant metal on Earth, approximately an order of magnitude more abundant than yttrium or scandium and more than three orders of magnitude than indium [102]. The cost to produce most no-Li-containing chlorides needed to synthesize Li_3MCl_6 is usually above $1000/kg, completely offsetting the cost-effectiveness of the LiCl precursor rounding ($5.88/kg) [102]. Wang Kai *et al.* [102] reported the synthesis of Li_2ZrCl_6 electrolytes using LiCl and $ZrCl_4$ as precursors. The cost of raw material for Li_2ZrCl_6 at a thickness of 50 μm is approximately $1.38/m^2, which is significantly lower than the cost of Li_3YCl_6 ($23.05/m^2) [102]. Li_2ZrCl_6 is considered the most economical chloride system based on existing literature. Moreover, its cost is well below the $10/m^2 threshold required for cost-competitive all-solid-state batteries. Additionally, the electrolyte was reported to be moisture-resistant at 5% relative humidity and displayed an ionic conductivity at room temperature of 0.81 mS.cm^{-1}.

Until now, solely lithium halide electrolytes have been introduced. Nevertheless, some sodium halide analogs have already been synthesized. The primary challenge encountered in synthesizing sodium-based halides lies in achieving a significant ionic conductivity while preserving the thermal stability of the electrolyte.

In 2020, Schelm *et al.* [103] reported successfully synthesizing $Na_{2.4}Er_{0.4}Zr_{0.6}Cl_6$ with an ionic conductivity of ~0.035 mS.cm^{-1} at RT. The research centered around the synthesis of the $Na_{3-x}Er_{1-x}Zr_xCl_6$ compound series, exploring different values of $0 \leq x \leq 1$ to identify the optimal stoichiometry that maximizes the electrolyte properties. The study

commenced by investigating the case where x = 0 corresponding to Na_3ErCl_6. The analysis revealed that Na_3ErCl_6 crystallizes with a monoclinic structure containing $ErCl_6^{3-}$ octahedra frameworks at the corners of the unit cell. Each $NaCl_6^{5-}$ prism is connected by an edge or corner sharing arrangement with another $NaCl_6^{5-}$ octahedron. The obtained ionic conductivity for the Na_3ErCl_6 electrolyte at approximately 25 ℃ was 10^{-6} mS.cm^{-1}. The case where x = 1 corresponds to the electrolyte Na_2ZrCl_6 displaying a trigonal crystal structure, the maximum reported ionic conductivity, in this case, 3.5 × 10^{-7} mS.cm^{-1}. When the incorporation of Zr^{4+} occurs, the structure adopted by the $Na_{3-x}Er_{1-x}Zr_xCl_6$ is monoclinic, as already discussed. Introducing smaller Zr^{4+} ions reduce lattice parameters. Additionally, the substitution of Er^{3+} by Zr^{4+} introduces sodium vacancies, leading to a tunable ionic conductivity in the series of solid solutions $Na_{3-x}Er_{1-x}Zr_xCl_6$, which in turn provides a promising step toward halide-based sodium-ion conductors.

In the realm of Yttrium metal sodium halide electrolytes, a recent contribution by Xu *et al.* [104] presented a new electrolyte, $Na_3Y_2Cl_9$, which was designed using a building block method. Here, a 3-step structure was proposed to create new structures incorporating Na^+ ions and $(Y_2Cl_9)^{3-}$ units. Theoretical analysis conducted in the study demonstrates that this electrolyte exhibits a low energy barrier for ionic diffusion, leading to an ionic conductivity of 0.1 mS.cm^{-1} at RT. Although the ionic conductivity may not be considered exceptional, the electrolyte demonstrates excellent chemical and electrochemical stability. Additionally, the calculated band gap for this electrolyte is determined to be 7.34 eV. Both agree with the large, simulated band gap of 5.2 eV and lower energy value for the conduction band E_C = -0.11 eV for E_0 electrons at rest for Na_3YCl_6 (**Figure 2** (a) and **Figure 2** (b)). The lowest energy for the E_C of Na_3YCl_6 is 1.62 eV, higher than Na^0. Therefore, Na_3YCl_6 is very stable against Na-metal, although with such a reduced electron affinity energy that it may decompose by being lowered from the surface in contact with any reductant.

Using DFT simulations, Liu *et al.* [105] proposed a new spinel chloride sodium electrolyte, $Na_2Y_{2/3}Cl_4$. This electrolyte is expected to exhibit a high ionic conductivity of 0.94 mS.cm^{-1} at RT with a low activation energy barrier for Na^+ ion diffusion of 0.29 eV while possessing a semiconductor energy gap [105] from –3.85 to –0.68 eV, E_0 = 0 electrons at rest in a vacuum, E_g = 3.17 eV.

Changing to Indium, in April 2023, Zhao *et al.* [106] reported the controlled synthesis of $Na_{2+x}Zr_{1-x}In_xCl_6$ electrolyte. The study was motivated by the limited number of reports on sodium halides, none discussing sodium halides containing indium. The authors investigated a series of solid solutions of $Na_{2+x}Zr_{1-x}In_xCl_6$ ($0 \leq x \leq 1$). The most promising

candidate from this study was the electrolyte for which x = 0.5, $Na_{2.5}Zr_{0.5}In_{0.5}Cl_6$, with an ionic conductivity of 0.066 $mS.cm^{-1}$ at RT.

Even though some promising improvements have been made in the production of halide electrolytes, the ionic conductivities remain considerably low when compared to other electrolytes, such as sulfide electrolytes, **Figure 1**. The advantages of doping existing electrolytes with halide elements such as chlorine are clear. A new class of electrolytes called oxyhalide seems to be the most promising. The previously discussed electrolytes in **Subsubsection 2.3.2** and two recently reported ones, $LiTaOCl_4$ and $LiNbOCl_4$ [11], are plotted considering their optimized stoichiometry and reported ionic conductivities (**Figure 1**).

Both oxide and halide electrolytes show considerably smaller ionic conductivities than sulfide-based electrolytes. Overall, oxyhalides display groundbreaking ionic conductivities, **Figure 1**, highlighting the Na^+ and K^+-glass electrolytes that have been reported to display self-charging behavior due to their ferroelectric nature [8], [107], [108], **Figure 7**, **Section 2.4**.

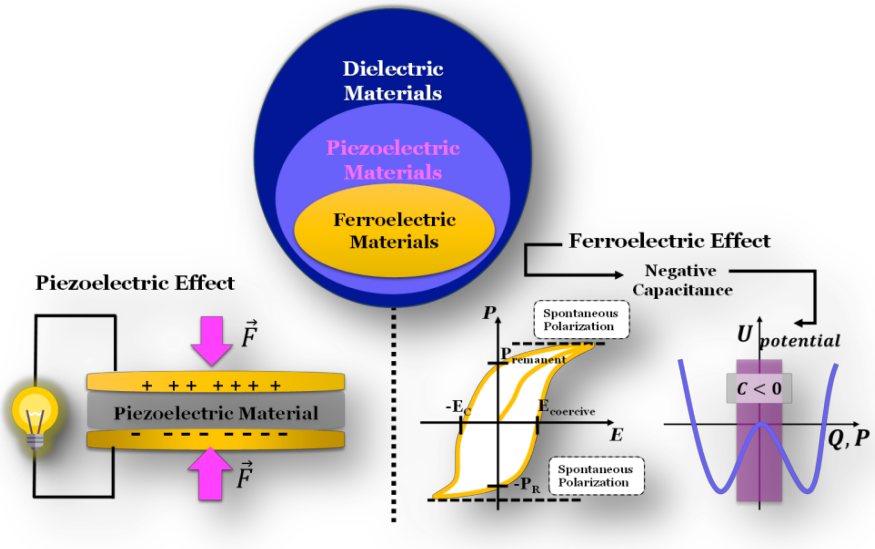

Figure 7.Dielectric, piezoelectric, and ferroelectric materials. Force $\vec{F}$, polarization *P*, capacity *Q*, electric field *E*, potential energy *U*, and capacitance *C*, remanent polarization $P_{remanent}$, coercive electric field $E_{coercive}$

2.4. Ferroelectric materials prospects for harvesting and storing energy.

The development of self-charging systems is fundamental to elevating the next generation of electronic devices. These systems will simultaneously display the ability to store energy as well as the ability to harvest energy. Piezoelectric materials are an option to transition the concept of self-charging to reality, specifically when these piezoelectric materials are also ferroelectric. The piezoelectric phenomenon occurs in dielectric materials that, when subjected to mechanical stress, can generate charge carriers, and polarize (**Figure 7**). Under an electrical field, the piezoelectric material undergoes a mechanical deformation or strain.

Ferroelectric materials have awakened the scientific community's interest due to their ability to display negative capacitance and, therefore, are expected to overcome fundamental limits of power dissipation in integrated circuits [109]. Ferroelectric materials can polarize spontaneously below the Curie temperature, leading to the formation of permanent dipoles, even when no electric field is applied. However, above the Curie temperature, the ferroelectric materials transition into a paraelectric phase, which has no spontaneous polarization. The negative capacitance NC was predicted by the Landau model for ferroelectricity [109]. From this model, it is possible to define capacitance as the reciprocal of the second derivate of the potential energy U with respect to the electric polarization charge, Q_F [110]: $C_F = \left(\frac{d^2U}{dQ_F^2}\right)^{-1}$. These phenomena have been studied and observed in different harvesting and storage devices. In 2014, Salvatore *et al.* [111] verified experimentally that the negative capacitance phase stability in a field transistor (FET) varies with temperature. The NC region narrows down at high temperatures when approaching the Curie temperature of the ferroelectric material, validating experimentally Landau's theory. In 2015, Khan *et al.* [112] performed the first synthesis of a thin epitaxial ferroelectric film displaying negative capacitance. When the applied potential difference is inferior to the coercive voltage (**Figure 7**), the capacity is positive, and therefore, the ferroelectric transistor behaves as a simple transistor. However, the authors verified that when the applied potential difference was superior to the coercive voltage, the ferroelectric switches to negative capacitance (**Figure 7**).

The negative capacitance phenomenon is not limited to transistor technology alone; it has also been observed in the field of batteries. In 2020, Braga *et al.* [108] reported the discovery of negative capacitance in an electrochemical cell that demonstrated the ability to self-charge. The researchers conducted the study using a cell containing two

electrodes separated by a ferroelectric glass oxyhalide electrolyte, previously investigated by the author in [8], [9]. The study established a clear linear relationship between the existence of negative capacitance double-layer capacitors and the system's remarkable capacity for self-charging, even when initially configured to discharge; the cells were set to discharge while maintaining a fixed external resistance. Although the set-up current was negative, the recorded voltage increased, and the current consistently remained above zero, indicating the presence of negative resistance alongside the negative capacitance regime. During this period of negative resistance, the battery exhibited self-oscillations, entering a self-cycling regime.

What is the link between ferroelectric materials, solid electrolytes, and the future of battery technology?

The future of energy harvesting, and storage devices is poised for greater diversity. In the realm of batteries, essential attributes include safety, high energy, and power densities, as well as extended cycle lives.

Solid electrolytes, especially those with ferroelectric properties, offer potential advancements in safety and density: LLTO, Na_3OCl, K_3OCl, $A_{2.99}Ba_{0.005}OCl$ – glass with A = Li, Na, K; with LLTO sub-performing when compared to the others. Ferroelectric materials, including halide-perovskites, demonstrate the prospect of introducing transformative changes to the energy storage landscape. Notably, ferroelectric electrolytes, including $A_{2.99}Ba_{0.005}OCl$ glass with A = Li, Na, K, exhibit unique properties such as self-charging and self-cycling based on coherent complex dynamics allowing for outstanding performance as discussed above. These electrolytes display quantum phenomena due to the spontaneous polarization, showing self-charging behavior, [8], [108], allowing the birth of attainable quantum batteries [113].

2.5. Cathode Materials

Among a battery's fundamental constituents, cathode materials stand out as pivotal elements. Typically, cathodes consist of an active material, a small quantity of conductive material, and a binding agent. The active material determines the theoretical specific capacity of the cathode. As of now, various families of active materials have been notable, including $LiNi_xMn_yCo_{1-x-y}O_2$ - NMC and $LiFePO_4$ - LFP, **Figure 8**.

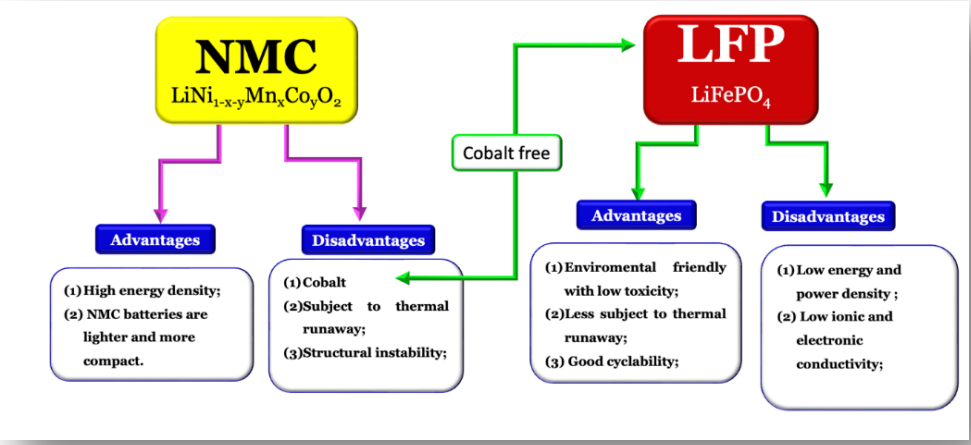

Figure 8. NMC vs LFP: Structure, plating mechanism of Li ions, and optimizations

$LiNi_xMn_yCo_{1-x-y}O_2$ containing batteries were first introduced to the commercial market in 2004 [114]. Over the past few years, NMC has emerged as the dominant cathode material in electric vehicles (EVs) and plug-in hybrid EVs, while also finding applications in power tools, medical devices, and portable electronics. The NMC's success comes from the combination of nickel, cobalt, and manganese [114]. Nickel contributes to a high specific energy, although it has limited stability. On the other hand, manganese enhances structural and thermal stability but lacks specific capacity due to its electrochemical inactivity. Since Co^{3+} is nonmagnetic, [114], and serves as a buffer atom, adding Co^{3+} relieves magnetic frustration from the layered structure due to the mixing of lithium and nickel. Co^{3+} prevents lithium-nickel mixing (cation mixing) and the resulting phase transition [114]. This ensures the formation of a stable cathode, facilitating a high-rate performance and improving cycle stability [115]. Consequently, the synergy of these elements leverages their respective strengths, ultimately resulting in an enhanced overall electrode material performance.

NMC materials are categorized as layered oxides, comprising stacked layers of metal oxide compounds. Each oxide layer has two planes of oxygen atoms, between which transition metal atoms occupy interstitial holes. Lithium ions intercalate the gaps between

the metal oxide compound layers, forming a one-atom thick lithium layer. Transport of lithium ions occurs within each lithium layer, giving rise to two-dimensional diffusion [116], [117]. The mobility of lithium ions within layered cathode active materials varies with their state of charge [118]. The NMC materials contain two types of particles: primary and secondary. The primary particles are composed of single or multiple layers of transition metals and Li and are usually nanosized. Secondary particles are composed of primary particles formed after decomposition and synthesis. The development of secondary particles proves advantageous for enhancing electrochemical properties. This is due to the internal porous structure within these secondary particles, which provides a shorter path for lithium ions and improved electrolyte access. Consequently, this facilitates lithium's efficient release and diffusion during both the charging and discharging processes [114].

Including cobalt in NMC raises environmental and humanitarian concerns, prompting a global shift toward cathode materials free of cobalt. Over the past two years, LFP Li batteries have gained significant popularity in China, the world's largest producer of electric vehicles (EVs). Additionally, Tesla, a prominent American automaker, has adopted LFP as the cathode material in all its standard-range vehicles. Industry competitors are choosing LFP chemistries for several reasons, including enhanced fire safety, lower operational costs, and greater flexibility in terms of depth of discharge. This flexibility is a significant advantage, particularly for short-duration applications.

The LFP cathode material, initially pioneered by Padhi *et al.* in 1997 [119], [120], stands out as a promising candidate for the next generation of batteries [121]. This cathode material is cobalt-free, making it environmentally friendly with low toxicity, economically feasible, and readily available [122]. The $LiFePO_4$ has a characteristic olivine structure [123]. The oxygen atoms form a hexagonal closed-packed ion, and octahedral holes are occupied by iron and lithium cations. The voids occupied by the lithium cations form continuous, parallel channels throughout the lattice [117].

During the charging of the $LiFePO_4$, more than one metastable Li-poor phase can be formed. The covalent bond between oxygen and phosphorous ions contributes to structural stability even when fully charged in the $FePO_4$ phase [124]. The theoretical capacity of LFP material is 170 $mAh.g^{-1}$, however achieving this value is an experimental challenge since instead of reaching a fully delithiated or fully lithiated phase, an intermediate phase with x = 0.25, less stable than $FePO_4$ is often obtained, as illustrated by the equation $LiFePO_4 \leftrightarrow Li_xFePO_4 + (1 - x)\ Li^+ + (1 - x)e^-$, compromising lower effective capacity under experimental conditions.

The stability of the $FePO_4$ framework makes the extraction of oxygen atoms more challenging compared to other oxide cathode materials, thus contributing to excellent thermal stability up to 400 °C [125]. However, at lower temperatures, LFP materials exhibit insufficient capacity due to several factors [126]: **(1)** the olivine structure restricts Li^+ diffusion along the (010) direction, resulting in low ionic conductivity [127] **(2)** the absence of a continuous FeO_6 network, which leads to low electronic conductivity [128] and **(3)** the phase-transforming lithiation-delithiation process during cycling, which impacts battery performance under severe/extreme conditions, resulting in the formation of unwanted phases.

2.6. Anode-Less Assembly – Novel Approach for battery design and construction

Lithium-ion (Li-ion) batteries stand as the predominant choice for energy storage systems. A commercial Li-ion battery configuration contains multiple cell stacks, each consisting of an anode current collector, an anode material, a separator, a cathode material, and a cathode current collector, all bathed in a liquid electrolyte [129]. The conventional anode material for Li-ion batteries is graphite, offering a theoretical capacity of 372 $mAh.g^{-1}$. However, the quest for enhanced energy storage capacity has led researchers to contemplate lithium metal as the ultimate anode material. Lithium metal presents remarkable attributes, such as a low density of 0.534 $g.cm^{-3}$, an extraordinary specific capacity of 3862 $mAh.g^{-1}$, and the most negative standard electrochemical potential, -3.040 V (SHE), among all anode materials [130] [129].

Nevertheless, integrating lithium metal into Li-ion batteries encounters significant challenges [131]. Issues like the growth of lithium dendrites, limited coulombic efficiency, and detrimental parasitic reactions with components in conventional liquid electrolytes consistently plague batteries during lithium deposition and stripping processes. Additionally, safety concerns surrounding the utilization of Li metal are countless; for instance, pure lithium metal is highly reactive and can react with moisture and air. This reactivity can lead to the formation of lithium oxide or lithium hydroxide, which can compromise the performance and safety of the battery. Furthermore, when considering mass production, pure lithium metal faces cost constraints primarily due to a decrease in global lithium reserves and the challenging extraction process required to obtain lithium from lithium-rich salt lakes and seawater, which has led to a significant exponential increase in the price of lithium. All the previous setbacks have instigated the development of Lithium-free batteries, also known as anode-less batteries, **Figure 9**.

In anode-less batteries, all active Li^+ ions are initially stored within the cathode material and the electrolyte. During the first charging process, Li^+ ions, initially sourced in the cathode, migrate through the electrolyte toward the anode current collector, where they undergo plating to create the previously non-existent lithium metal anode [132]. There are several advantages to anode-less batteries. The absence of a Li^+-based anode material reduces the cell's weight and the volume necessary for the anode component. Consequently, an anode-free battery exhibits a significantly higher energy density than conventional Li-ion batteries, even after the battery's thickness increases due to Li plating during charging. Moreover, this approach leads to savings in energy and production costs associated with anode manufacturing.

However, in anode-less systems, the current collector has a high interface energy with lithium, leading to the deposition overpotential rise [133]. This, in turn, affects the morphology of the deposited lithium, resulting in the formation of a solid-electrolyte interphase (SEI) and even dendrite growth [134], [135]. Due to undesirable interfacial and internal events, this structural characteristic can negatively impact the coulombic efficiency (CE) during each cycle. The ideal conditions for depositing lithium on the current collector's surface involve lower nucleation overpotential and weaker surface diffusion barriers, allowing for a two-dimensional (2D) growth of the lithium layer on the current collector [136]. The growth behavior of plated lithium on a given substrate also depends on factors such as surface energy, interfacial energy, and the two-phase contact angle [137].

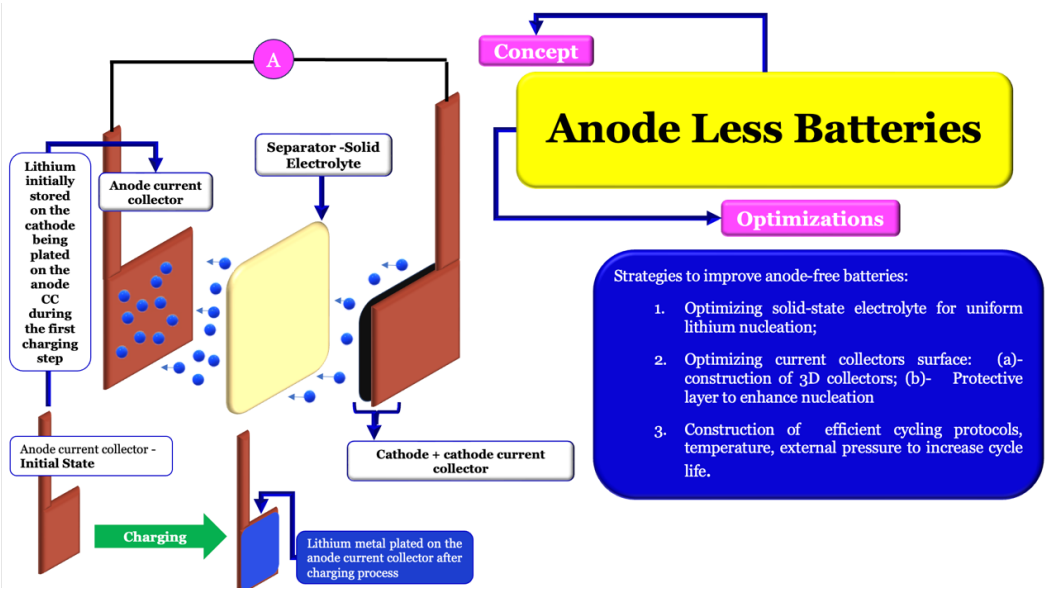

Figure 9. Anode-less Batteries: Structure, plating mechanism of Li ions, and optimizations

Several studies have been undertaken to address the challenges and enhance the efficiency of anode-less cells. Among these strategies, one of the most notable involves incorporating a thin protective layer on the current collector of the anode. Neudecker *et al.* (2000) [138] reported a novel lithium-free thin-film battery with an in-situ Li coating on the Cu anode current collector during the charging step. This work was then cited by Bates *et al.* (2000) [139]. Lee, Liu, and Tracy (2003) [140] assembled an anode-free solid-state battery (AFSSB) with a different configuration, namely SS/LiPON/$Li_{1.3}V_2O_5$/Cu, fabricated on a stainless steel (SS) substrate using sequential thin film deposition methods. Westover *et al.* (2019) [141] worked with a solid LiPON electrolyte, highlighting the importance of achieving a homogeneous, pore-free morphology for anode-less battery success. Zegeye *et al.* (2020) [142] developed a surface-rolled ultrafine polymer solid-state electrolyte for anode-free solid-state batteries. Wang *et al.* (2020) [143] presented a "Li-free" battery using the solid electrolyte $Li_7La_3Zr_2O_{12}$ (LLZO). The cell was achieved by directly depositing lithium from a composite cathode of NCA/PEO onto a copper current collector through the LLZO electrolyte. This cell underwent 50 cycles at a C/19 rate, showing initial capacities of 0.8 $mAh.cm^{-2}$ and nearly 100% Coulombic efficiency.

Lee *et al.* [144] showed the practical viability of sulfide solid state electrolyte anode less batteries, when the authors synthesized an anode less cell with a sulfide electrolyte containing an Ag-C protective layer on the anode current collector. Park *et al.* [145] produced an anode less cell containing nickel powder coated with carbon protective layer. In 2022 and 2023, numerous interdisciplinary studies focused on the advancement of anode-less or anode-free cell configurations across multiple fields were developed [146]–[150]. The MatER laboratory from university of Porto made interesting contributions to these fields. First 2022, Guerreiro *et al*. [151] investigated the surface chemical potentials of different materials with potential applications in lithium-ion battery interfaces. They discovered that zinc oxide (ZnO) demonstrated surface chemical potential equalization when interfaced with copper (CC). Furthermore, they noticed the existence of a negatively charged region at this interface, which they believed would promote the nucleation. This year Baptista *et al.* [152], also from the same research group, confirmed the previous premise through the publication of an article that discusses the optimization and viability of an anode-less cell utilizing zinc oxide as the protective layer for the anode current collector. The author verified the plating of lithium via direct and indirect measurements. Hereafter, these measurements are going to be discussed in detail.

Chapter 3

Experimental Procedures

This chapter is dedicated to defining the assembly procedures used in the fabrication of the cells, offering detailed explanation of the testing methodology, and outlining the sequence for data analysis. To evaluate the performance of the manufactured batteries several methods were used, including: **(1)** Potentiostatic Electrochemical Impedance Spectroscopy (PEIS), **(2)** Electrochemical performance: Charge and Discharge cycles, **(3)** Chronopotentiometry, and **(4)** Cyclic Voltammetry (CV). Additional testing was conducted using an **(5)** atomic force microscope (AFM) with nanometric scale Scanning Kelvin Probe (SKP) to gather data and insights on the materials used to ensemble the batteries.

3.1. Materials

3.1.1. $Li_{2.99}Ba_{0.005}ClO$ electrolyte

The $Li_{2.99}Ba_{0.005}OCl_{1-x}(OH)_x$ all-solid-state electrolyte was obtained from the commercial precursors LiCl (99 %, Merck), Li(OH) (98.0%, Alfa Aesar), and $Ba(OH)_2$ (anhydrous, 94 % - 98 %, Alfa Aesar). Then, $Li_{2.99}Ba_{0.005}OCl_{1-x}(OH)_x$ glass electrolytes were allowed to react and dry between 230 and 250 °C. After obtaining the dry $Li_{2.99}Ba_{0.005}ClO$ solid-state material, the ferroelectric glass-electrolytes were ground for 40 min (300 rpm) using a ball milling machine with an Agate container and five balls with a 20 mm, which was closed hermetically to avoid water absorption during the process.

Pouch Cell. The $Li_{2.99}Ba_{0.005}ClO$ powder was mixed with absolute ethanol. The thermoplastic polyvinyl acetate (PVAc) $(C_4H_6O_2)_n$ was added to the electrolyte/ethanol mixture, with the ratio in weight of 80% $Li_{2.99}Ba_{0.005}ClO$ plus 20 % PVAc. The resulting homogeneous mixture was then impregnated onto the cellulose sheet. Adding PVAc, white glue, improves the hygroscopic character, maintaining the dielectric properties of the electrolyte while promoting electrical contact and mechanical adhesion between the electrodes and the electrolyte. Ultimately, these separators were dried inside the glove box at 90 ºC with Ar-filled (O_2 and H_2O < 1 ppm).

Coin Cell - The $Li_{2.99}Ba_{0.005}ClO$ powder was prepared as a bilayer with the cathode material, inside a GS glovebox.

3.1.2 Li_6PS_5Cl electrolyte

Lithium argyrodite Li_6PS_5Cl was used as an electrolyte and was obtained in MSE. The electrolyte was used as a bilayer with the cathode material.

3.1.3 $LiFePO_4$

Lithium iron phosphate (LFP) (98.71%) powder was used as an active material, with 1.132 $g.cm^{-3}$ density. The cathode reagents were acquired from TMAX Battery Equipment's: **LFP 98.71%** powder; Alfa Aesar: **Carbon black super P® 99+%**; Nanografi Nano Technology: **PVDF binder for battery**; Sigma-Aldrich: **NMP**; and MSE supplies: single side conductive carbon coated aluminum foil.

Pouch Cell. An $LiFePO_4$ double side cathode foil was obtained in MSE Supplies. This foil was cut into a (40 x 40) mm^2 square or (35 x 4) mm^2 rectangle and glued to a Cu current collector using electrical conductor glue. Afterwards the Cu current collector containing the LFP foil was placed at 70 °C overnight in a vacuum oven.

Coin Cell. The LFP cathode mixture was prepared using 57 % LFP, 3 % Carbon black and 40 % of electrolyte ($Li_{2.99}Ba_{0.005}ClO$ or Li_6PS_5Cl). Firstly, the LFP powder and the carbon black powder were heat treated for 1h under 70 ºC. Afterwards they were placed inside the glovebox, where the final mixture was prepared.

3.1.4 NMC

The NMC 90:10:10 cathode mixture was prepared with the following amounts: 57 % NMC 3% Carbon black and 40% Li_6PS_5Cl. The NMC cathode was provided to the laboratory from a partner in the PULSELION project. The Li_6PS_5Cl and the NMC active material were inside the glovebox, controlled environment. Before entering the glove box, the carbon material was heat treated for 1h at 70ºC.

3.1.5 ZnO – Zinc Oxide Solution

A mixture consisting of 90 % zinc oxide (ZnO), 10 % Polyvinylidene Fluoride (PVDF), and N-Methyl-2-Pyrrolidone (NMP) solvent was prepared (3 mL of solvent for 1 g of solute) and stirred for 2 hours at 60 °C. The resulting solution was then doctor-bladed onto a copper substrate, creating a thin coating layer, and subsequently placed in a vacuum oven at 70°C overnight for solidification.

The materials used were sourced from the following suppliers: Alfa Aesar for ZnO (99.99% purity, powder diameter < 74 µm), Nanografi Nano Technology for PVDF binder, and Sigma-Aldrich for NMP solvent.

3.1.6 Li_2O – Lithium Oxide Solution

A mixture consisting of 90 % Lithium oxide (Li_2O), 10 % Polyvinylidene Fluoride (PVDF), and N-Methyl-2-Pyrrolidone (NMP) solvent was prepared (3 mL of solvent for 1 g of solute) and stirred for 2 hours at 60 °C. The resulting solution was then doctor-bladed onto a copper substrate, creating a thin coating layer, and subsequently placed in a vacuum oven at 70 °C overnight for solidification.

The materials utilized were sourced from the following suppliers: Alfa Aesar for Li_2O (99.5 %, metal basis), Nanografi Nano Technology for PVDF binder, and Sigma-Aldrich for NMP solvent.

3.1.7 Laminated Film

A 70 × 160 mm² aluminum laminated film was cut and then folded in half along its largest dimension using a pouch case forming machine, resulting in the formation of the shape where the cell components will later be placed.

3.2. Methods

In this section, the fabrication procedure of the cells will be discussed, along with the techniques used to test the cells. A concise explanation of each method will be provided to comprehend the information extracted from each technique, starting with PEIS and concluding with atomic force microscopy.

Potentiostatic Electrochemical Impedance Spectroscopy (PEIS). Electrochemical impedance spectroscopy, EIS, is a widely used technique in corrosion studies, semiconductor science, energy conversion, storage energy technologies, chemical sensing, noninvasive diagnostics, etc. The principle of EIS involves perturbing an electrochemical system in equilibrium or a steady state by applying a sinusoidal signal over a wide range of frequencies and then monitoring the sinusoidal response of the system towards the applied perturbation. In this thesis, the focus is on potentiostatic EIS (PEIS). In PEIS, the potential of the cells is constant while measuring the sample's impedance across a spectrum of frequencies. This technique allows the user to gain insights into kinetics, charge transfer dynamics, and other electrochemical characteristics of the cells. The PEIS test was performed using a Gamry 3000 potentiostat.

PEIS curves are influenced by the types of materials used in a battery and its architecture. Each curve requires careful interpretation to correctly understand the possible results. To understand the type of interpretation of this curve a theoretical reference curve for a commercial lithium battery cell using liquid electrolyte will be

considered, **Figure 10**. The initial segment of the graph, denoted by the green zone in **Figure 10**, emphasizes the presence of inductive behavior. This is not a result of magnetic effects but rather arises from the increased capacitance of the cell at higher frequencies. Moving on to the yellow zone in **Figure 10**, the first semi-circle corresponds to phenomena occurring within the bulk of the material. The parameter R_1 allows the determination of the ionic conductivity of the material. The third region, highlighted in blue, (**Figure 10**) represents phenomena occurring at the interfaces. However, these phenomena are almost negligible since the electrolyte is liquid and the interfaces of commercial cells are optimized. Concluding with the orange zone in **Figure 10**, depicts diffusion processes associated with the Warburg region.

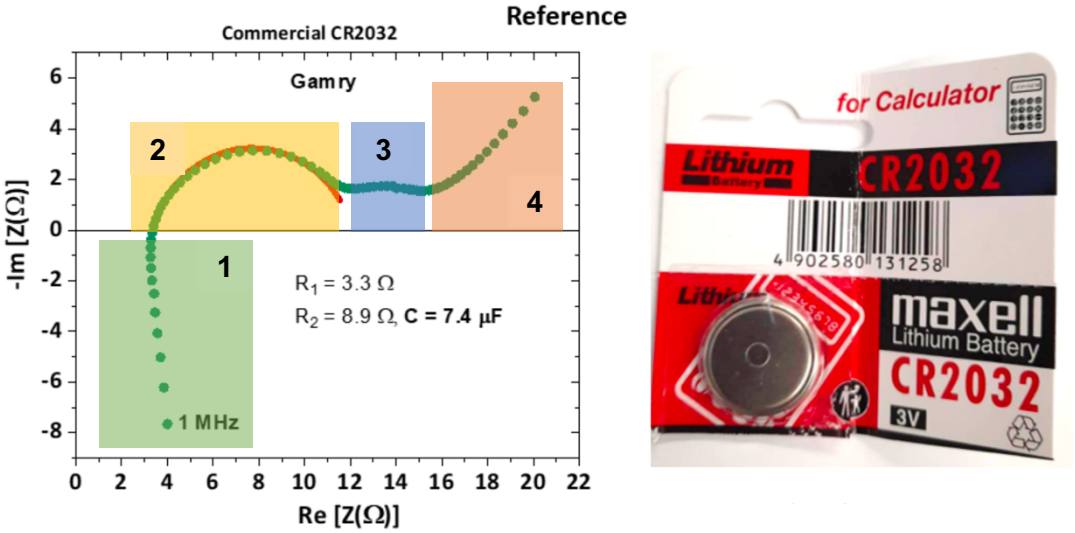

Figure 10. Potentiostatic Electrochemical Impedance Spectroscopy (PEIS) curve of a commercial lithium-ion cell containing liquid electrolyte.

Galvanostatic Charge and Discharge. Galvanostatic Charge-Discharge (GCD) is used to evaluate the performance and longevity of EDLCs and batteries. A cycle is defined as a consecutive sequence of charge and discharge steps. During the charging process, an imposed current is established to charge the cell until it achieves the maximum charging voltage. The following step is the discharge phase, where a negative current is set until a predetermined minimum voltage is reached. This test enables the acquisition of information about the cell: **(1)** calculate specific capacity; **(2)** study the behavior of the cell at different C-rates and the cell's ability to maintain its capacity; **(3)** calculate the coulombic efficiency of the cell; **(4)** study the life cycle of the battery and **(5)** provide an indirect method to observe the deposition of lithium ions in the anode current collector of anode-less cells. The galvanostatic cycling tests were performed in a Neware CT-4008Tn - 5v200mA battery tester.

The charge and discharge performance of a battery is linked to the cell's composition and architecture. While the potential difference limits during charge and discharge are primarily influenced by the cathode's active material, it is crucial to account for factors such as electrolyte degradation above or below specific potential differences. To comprehend the results obtained in the charge and discharge testing, it will be considered the study developed in [153]. It's crucial to acknowledge that the architecture and materials used in that study are somewhat different from what was implemented in this thesis. Consequently, the analysis of the results obtained for the cells assemble in the context of this thesis will differ accordingly.

Figure 11 illustrates the charge and discharge behavior of a coin cell containing LFP as the cathode active material, $LiPF_6$ liquid electrolyte, and graphite as the anode, [153].A plateau region is highlighted in green; this region corresponds to a phase equilibrium between lithiated and non-lithiated states of the LFP active material that occur during charge and discharge.

In contrast, the NMC active material exhibits no plateau region during charge and discharge cycling, indicating that no equilibrium of intermediate phases occurs. For a cell to be considered to perform well, its discharge capacity should closely match the theoretical capacity of the active material. These values have been calculated for our cells, as reported in **Subsection 3.2.1.**

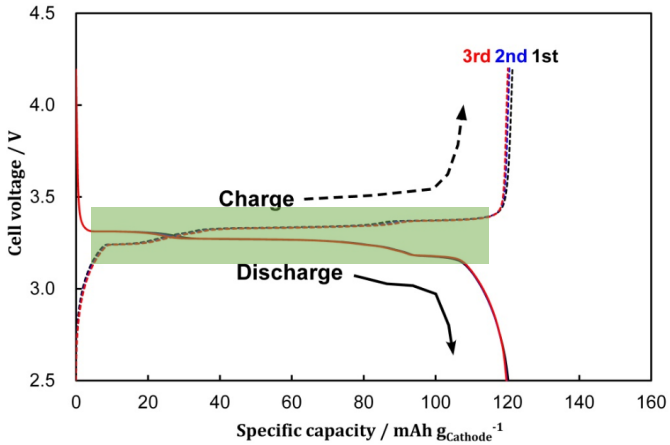

Figure 11. Charge and Discharge curve of a coin-cell featuring LFP as cathode material, LiPF6 liquid electrolyte and graphite as the anode material. Reproduced from ref.[153] CC BY 4.0.

Chronopotentiometry. In chronopotentiometry, a constant electric current is applied to the electrochemical cell. This means that a steady flow of charge is introduced into or withdrawn from the cell over time. Simultaneously, the potential difference across the cell's terminals is continuously measured and recorded as a function of time. Conducting

repeated chronopotentiometry experiments over multiple cycles allows for an assessment of the battery's long-term stability and cycle life. Changes in voltage profiles and performance deviations reveal degradation mechanisms and cycle-to-cycle variations, which are essential for optimizing battery reliability. The chronopotentiometry tests were performed with a Biologic VMP-300 potentiostat/galvanostat/impedance spectroscope.

When implementing a chronopotentiometry test on a symmetric cell containing Li metal in both the cathode and anode sides, one can extract valuable information about Li plating. To comprehend the potential outcomes derived from the chronopotentiometry testing procedure, an interpretation of the results from the study conducted in [154] will be provided, **Figure 12**.

It is crucial to acknowledge that the architecture and materials employed in that study differ from those implemented in this thesis. Consequently, the interpretation of the results for the cells assembled in the context of this thesis will also vary accordingly.

The cell examined in **Figure 12** is a symmetric configuration comprising Li metal – gel polymer electrolytes, GPE, dry membrane – Li metal. This test reveals the variations in cell plating at different current densities and the consequent impact on the cell's overpotential. Notably, the graph indicates that the cell cannot withstand higher current densities, likely due to excessive resistance. Additionally, this graph provides insights into the reversibility of the cell's behavior and its conditioning over prolonged periods.

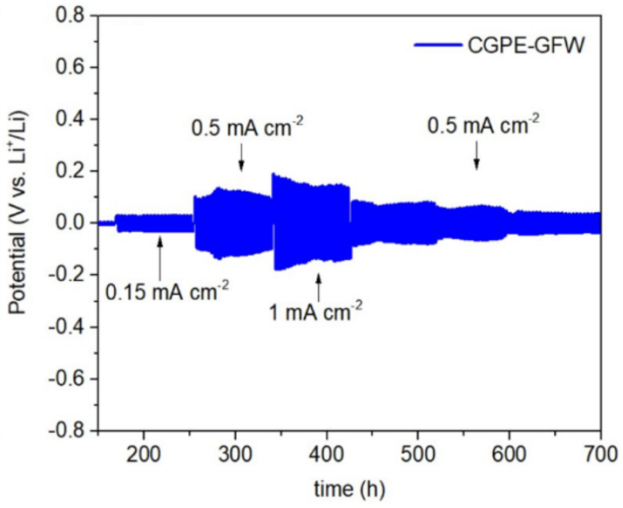

Figure 12. Chronopotentiometry test to study the Li plating/stripping performance of CGPE-GFW Li | Li symmetric cell at different density currents. Reproduced from ref. [154] CC BY 4.0.

Cyclic voltammetry. Cyclic voltammetry (CV) is an electrochemical method employed to study the electrochemical characteristics of a system, commonly an electrochemical cell or electrode. This technique involves cyclically varying the electrode's potential difference between two specified potential limits at a constant rate while monitoring the corresponding current response. The voltage range selection and scan rate is determined according to the specific goals of the experiment. During this potential sweep, the current flowing through the cell is recorded, and it is often directly proportional to the rate at which electrochemical reactions are taking place at the electrode's surface. The cyclic voltammetry test was performed using a Gamry 3000 potentiostat.

Cyclic voltammetry testing reveals the cell's behavior across a broad potential difference range. To comprehend the potential outcomes derived from CV testing, an interpretation of the results from the study conducted in [153] will be provided. It's essential to recognize that the architecture and materials employed in that study differ from those implemented in this thesis. As a result, the interpretation of the results for the cells assembled in the context of this thesis will also differ accordingly. In **Figure 13**, a CV curve of a coin-cell featuring LFP as the cathode active material, $LiPF_6$ as the liquid electrolyte, and graphite as the anode material [153] is plotted. In **Figure 13**, a voltage sweep was conducted across a pre-defined range of potentials as set by the technician. Within this potential difference range, oxidation and reduction peaks were observed. These peaks correspond to lithiation and de-lithiation processes taking place inside the cell. The interpretation of cyclic voltammetry and the observed results vary depending on the materials used in the cell. Furthermore, the response of distinct cells corresponds to different systems; for instance, the absence of oxidation and reduction peaks could indicate that the tested cell functions as a capacitor rather than a battery.

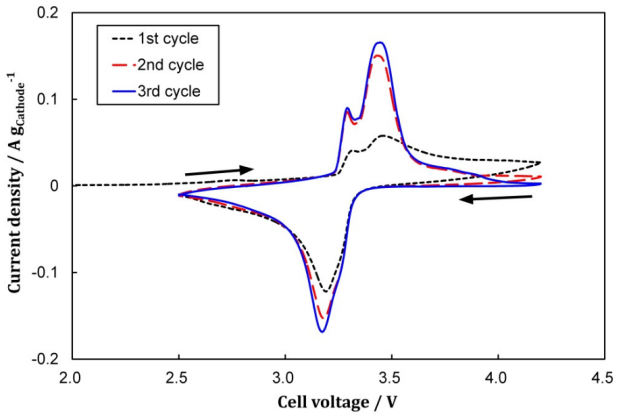

Figure 13. Cyclic Voltammetry curve of a Coin-Cell Featuring LFP as Cathode Material, LiPF6 Liquid Electrolyte, and graphite as the anode material. Reproduced from ref. [153] CC BY 4.0.

Scanning Kelvin Probe, SKP. SKP is a non-invasive technique derived from atomic force microscopy (AFM), that facilitates the electrochemical analysis of materials. SKP measurements provide a range of valuable information, including contact potential differences within a cell, the work function (WF) of each material in the cell, materials topography, capacitance, and, *in operando* cell's behavior. The SKP analysis, with nanometric, definition was carried out in an Oxford Instruments Atomic Force Microscope.

3.2.1. Assembly and Testing Procedures for Coin Cells

The initial step to assemble the coin cell is preparing the cathode mixture, as detailed in **Sections 3.1.3** and **3.1.4.** Subsequently, a bilayer comprising electrolyte and cathode material is fabricated inside a GS glove box. Initially, a 100 mg layer of electrolyte was placed in a 10 mm diameter mold to be compressed for 2 minutes using an applied pressure of 1 Ton. Following this, the top of the previous layer was filled with 15-30 mg of the cathode mixture, carefully positioned, and compressed for 2 minutes with an applied pressure of 2 Ton. Finally, all the cell components were assembled, as depicted in **Figure 14**.The coin cell was securely sealed inside the glovebox under a pressure of 6.14 Ton-force within a crimping machine.

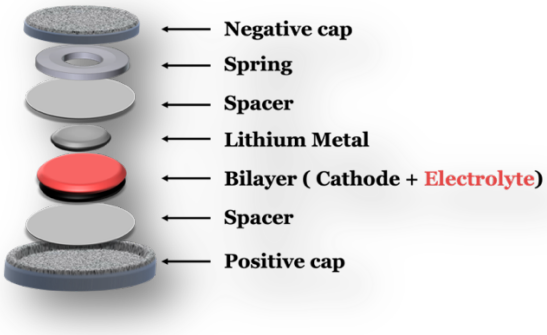

Figure 14. Schematic representation of the half (coin) cell architecture.

The testing of the non-symmetric or half-cell starts with the registration of the open-circuit voltage (OCV), followed by an impedance spectroscopy analysis of the cell. The impedance spectroscopy varies from frequencies between 7 MHz to 1 mHz. The swipe around these frequencies is made three times, resulting in 3 cycles. Subsequently, the cell undergoes charge-discharge cycling at 25 ºC, following a program with the following rates: C/50, C/20, C/10, C/5, C/2, C, and C/50 rate again, **Table 2**. The first step is to determine the cell's theoretical specific capacity of the NMC and LFP cathode materials to calculate the charge and discharge rates. It was considered that during the charging process, only 70% of the Li ions depart from the cathode material, as the metastable

phase forms predominantly. Consequently, the chemical equations for the charging process are as follows, considering both $LiFePO_4$ and NMC materials:

$$\boldsymbol{LiFePO_4 \rightarrow Li_{0.3}FePO_4 + 0.7Li^+ + 0.7e^-}$$

$$\boldsymbol{LiN_{0.90}Mn_{0.05}Co_{0.05}O_2 \rightarrow Li_{0.3}N_{90}Mn_5Co_5O_2 + 0.7Li^+ + 0.7e^-}$$

The molar mass of NMC can be calculated by the following equations: $M(NMC) = M(Li) + 0.90\,M(Ni) + 0.05\,M(Co) + 0.05\,M(Mn) + 2\,M(O) = \ 97.45\ g.mol^{-1}$. Similarly, for LFP, the molar mass is determined as $M(LFP) = M(Li) + M(Fe) + M(P) + 4M(O) = 157.76\ g.mol^{-1}$. The charge corresponding to 0.7 electrons is: $q = n_{electrons} \times N_A \times 1mol \times q_{electron\ elementary\ charge} = 0.7\ \times 6.022\ \times 10^{23} \times 1.6 \times 10^{-19}$ C $= 6.745 \times 10^4 C$. The charge is related to the current through the equation $q = i \times t$, meaning that 1 coulomb is equivalent to 1 ampere-second (1 As), so $\frac{6.745 \times 10^4}{3600} \times 1000\ mAh = 18735.11\ mAh$. Finally, to obtain the value of the specific capacity, it is only necessary to divide the previous value by the molar mass of the cathode material obtaining: $C_{NMC} = \frac{18735.11}{97.45} = \ 192\ \ mAh.g^{-1}$ and $\ C_{LFP} = \frac{18735.11}{157.76} = 119\ mAh.g^{-1}$.

Subsequently, it is essential to identify the cathode's active material corresponding to the surface area of the limiting electrode, which, in this case, is the area of the lithium metal (Li^0). The surface area of the lithium electrode is given by $A = \pi r^2 = \pi \times (4 \times 10^{-3})^2 = 0.504\ cm^2$. It used 10 mg of cathode material within an area of 0.785 cm^2; the mass of the active material corresponds to the active area employed, which, as explained before, corresponds to 0.504 cm^2. The mass of cathode material corresponding to 0.504 cm^2 is 6.42 mg. Only 57% (3.9 mg) of the mass corresponds to the active material of the total cathode material. To calculate the capacity of the active material, it is only necessary to multiply the specific capacity by the mass of the active material, resulting in a value of 0.755 mA.h for the NMC cathode and 0.464 mA.h for the LFP. To determine the required current for the previously mentioned rates, the capacity is divided by the number of hours, as demonstrated in the table below for both LFP and NMC calculations, **Table 2**.

Furthermore, another type of coin cell, known as a symmetric cell, was fabricated. These coin cells were assembled with the following components: Top Cap, Spacer, Li metal, Li_6PS_5Cl electrolyte (100 mg compressed under 1 ton of pressure for 2 minutes), Li metal (again), spacer, conic spring, and bottom cap. Initially, a PEIS test was conducted using the previously mentioned parameters in these cells, followed by a chronopotentiometry test.

Table 2. C – rates charge and discharge

C - Rates	NMC	LFP
C/50	15 μA	9 μA
C/20	38 μA	23 μA
C/10	76 μA	46 μA
C/5	151 μA	93 μA
C/3	251 μA	154 μA
C/2	378 μA	232 μA
C	755 μA	464 μA

3.2.2. Assembly and testing procedures for anode-less cells

Throughout the work leading to this thesis, anode-less batteries were fabricated using a pouch cell production line. The process started with preparing the $Li_{2.99}Ba_{0.005}ClO$ glassy electrolyte, outlined in Section 3.1.1. In the subsequent step, a cellulose separator was embedded within the $Li_{2.99}Ba_{0.005}ClO$ glassy electrolyte already fabricated, as described in section 3.1.1. Once all components had been thoroughly dried, the assembly process commenced. In **Figure 15 (a)**, the materials are arranged sequentially: a copper anode current collector, the $Li_{2.99}Ba_{0.005}OCl$ glassy electrolyte + cellulose, and a copper current collector with LFP attached using conductive glue to the collector. These components were then joined together to form the cell, as depicted in **Figure 15(b)**, and short-circuit-guarded with a Teflon tape, as shown in **Figure 15(c)**. Finally, the cell underwent vacuum sealing and was encased within an aluminum-laminated film, preparing it for subsequent testing procedures (**Figure 15 (d)**).

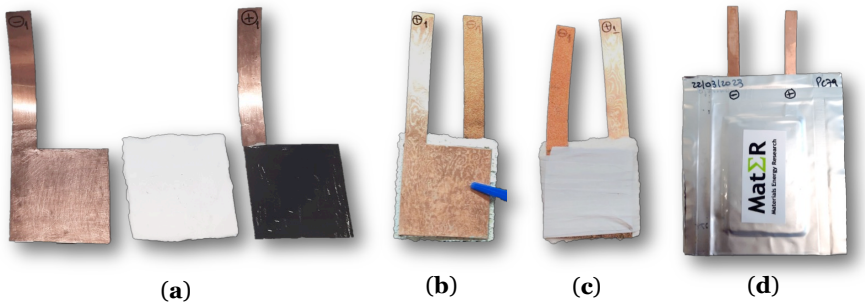

Figure 15. Cell assembly: **(a)** materials; **(b)** cell; **(c)** cell protected by Teflon tape; **(d)** vacuum closed and sealed cell.

The testing procedure started with a charge-discharge cycle. Initially, a current was applied during the initial charging phase to promote the nucleation of lithium ions on the

anode current collector. Following the initial charges, the current was progressively increased to reach the cell's specific capacity, and the performance was closely monitored. Subsequently, the anode-less cells were set to discharge with an external resistance connected to the battery terminals (the machine set no applied discharge current). The resistors used during this testing procedure ranged from 4.7 MΩ to 94.9 kΩ. The testing started with resistance values around 4.7MΩ and ended in smaller values at approximately 94.9 kΩ. Initially, a higher resistance is used to prevent the complete detachment of Li plated on the copper electrode during the discharging phase (higher resistance correlates with smaller discharge current), promoting the creation of stable interfaces. Later, the resistor switched to a lower value to maximize discharge capacity since capacity is directly proportional to the discharge current – a higher discharge current results in greater capacity. This strategy aimed to manage the charge-discharge process effectively. Impedance measurements for the cells were also conducted. The testing parameters employed were the same as those described in section 3.2.1 for the coin cells.

3.2.3. Atomic Force Microscope and Scanning Kelvin Probe Sample Preparation Methodology

The samples were prepared on a glass lamella for the atomic force microscope, AFM. A small amount of powder under study was placed on top and securely attached using a non-reactive organic lacquer. Efforts were made to ensure that the sample surface was as flat as possible to preserve the integrity of the AFM tip. This was achieved using a spreading spatula.

The tip employed for conducting the SKP analysis was an AYLEC – 01. The AFM calibration was carried out directly within the IGOR Software. To ensure the functionality of the AFM tip, an initial calibration was performed with the following parameters: SUM 5 and Deflection 0. Following this, an autotune of the tip was conducted, and the peak of the curve should correspond to the resonance frequency of the tip. Once all these verifications were confirmed, the instrument was set to initiate the SKP protocol.

Chapter 4

Results and Discussion

4.1. Scanning Kelvin Probe – Atomic Force Microscope

In the AFM, samples are analyzed within a 4 μm × 4 μm region. In the **Figure 16**, it is possible to observe two distinct images of two different samples positioned within the AFM. To ensure correct testing, it's crucial to be vigilant for warning signs in the results even after the calibration procedure. Firstly, if the topography closely aligns with the trend of the potential analysis, it may indicate that the tip could be compromised, affecting the accuracy of the measurement. Additionally, observing multiple triangular shaped regions (shaped tips) can indicate contaminations on the tip; this creates two or more contact ends with the sample. This section focused on utilizing AFM and SKP techniques to characterize the cathode active materials employed in this thesis, including NMC with a stoichiometry of 90-5-5 and $LiFePO_4$. Topography and SKP data were acquired for each sample. In the context of this thesis, two samples were subjected to analysis: an LFP sample (**Figure 18**) and an NMC sample (**Figure 17**). Both samples underwent topological analysis and scanning kelvin probe analysis. The analysis performed to both samples shows divergence in data trends between topography, as shown in **Figure 18 (a)** and **(b)** for LFP and **Figure 17 (a)** and **(b)** for NMC, and the scanning Kelvin probe analysis (SKP) data, as illustrated in **Figure 18 (c)** for LFP and **Figure 17 (c)** for NMC.

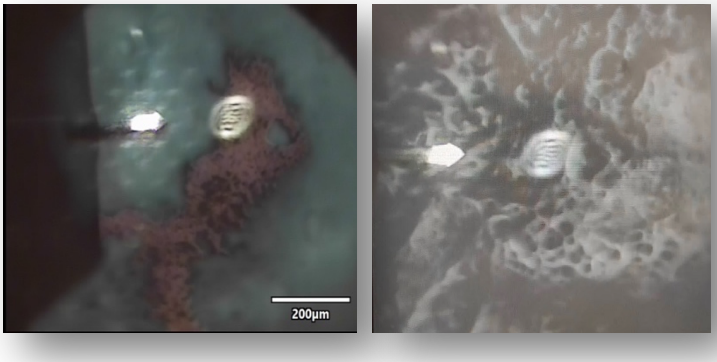

Figure 16. Two different samples analysed on the AFM.

The distinctive behavior of LFP, characterized by charge accumulation regions due to its semiconductor nature, is evident in **Figure 18 (c)**, with oscillations of the chemical potential between a maximum and a minimum value. This behavior is absent in the case of NMC, which exhibits no oscillatory pattern due to its conductor properties, inhibiting

the formation of charge accumulation regions. Furthermore, it is worth noting that in a simulation conducted for another ongoing work (not yet published), the chemical potential of NMC was determined to be +1.1 V vs. SHE. This is in line with the average potential displayed in **Figure 17 (d),** which also reads as +1.1 V vs. SHE, thus demonstrating consistency in the findings.

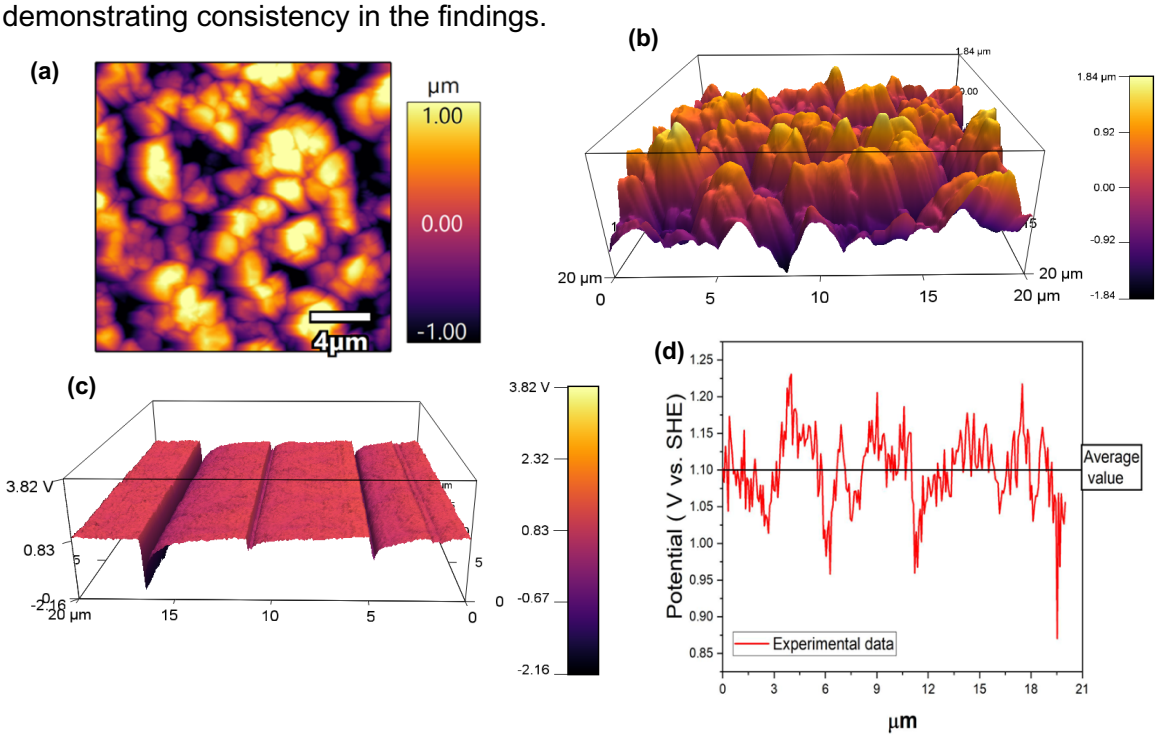

Figure 17. AFM on NMC sample. **Topography**: **(a)** 2D and **(b)** 3D. **SKPM:** **(c)** 3D study and **(d)** 2D Potential study.

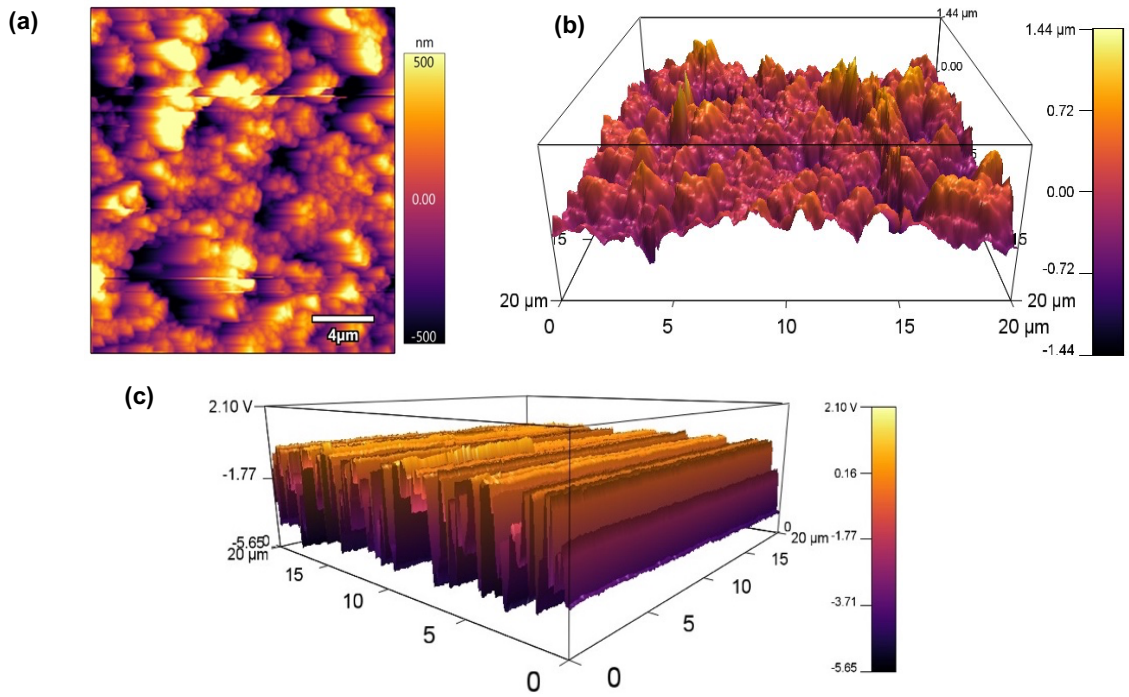

Figure 18. AFM on LFP sample: **Topography**: **(a)** 2D and **(b)** 3D. **(c)** SKPM analysis

4.2. Coin – Cell

This section is dedicated to the investigation of various coin cells under different conditions and composed of diverse materials. Firstly, the cells can be categorized into half and symmetric groups. Two lithium metal layers separated by an electrolyte layer were studied in the symmetric cells. Initially, the cell underwent a Potentiostatic Electrochemical Impedance Spectroscopy (PEIS) test. Subsequently, a chronopotentiometry procedure was initiated. After a 60-hour interval, a reduction in voltage amplitude took place. This variation was studied by conducting a second PEIS test.

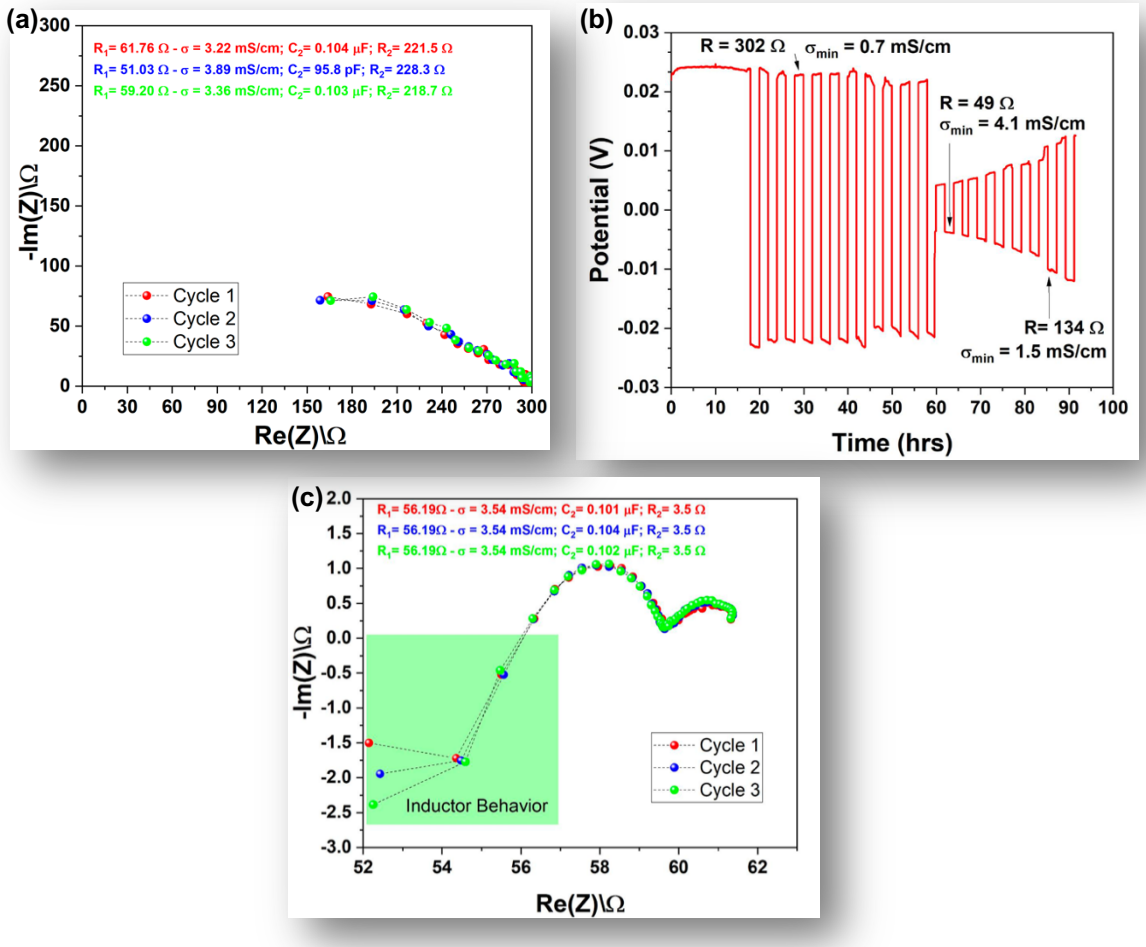

Figure 19. Symmetric cell study: (a) PEIS test immediately after assembling; (b) chronopotentiometry test; (c) final PEIS after chronopotentiometry.

Upon assembly, the symmetric cell underwent an immediate Potentiostatic Electrochemical Impedance Spectroscopy (PEIS) test, as depicted in **Figure 19 (a).** The PEIS technique is considerably interesting since it allows to identify the phenomena that resonates with the applied frequency with precision. In a solid capacitor, usually, when a cation moves, a hole with an opposite charge stays behind. In a solid electrolyte, this

affects both the positive and negative electrodes. In a solid electrolyte equivalent circuit, at least one solid capacitor is present and corresponds to the bulk part of the material. The higher spectrum of frequencies corresponds to the movement of ions in the bulk of the solid electrolyte. The lower ranges of frequencies correspond to phenomena that occur on the interfaces of the different materials that compose the cell. **Figure 19 (a)** offers insights into the estimation of bulk ionic conductivity through the value R_1, which can be calculated considering the formula $\sigma = \frac{d}{A \times R}$, where R is the resistance within the bulk of the electrolyte, d denotes the thickness of the electrolyte separator ($d = 0.1\ cm$ in this thesis), and A represents the cross-sectional surface area ($A = 0.502\ cm^2$). The obtained ionic conductivities varied between 3.22 mS.cm^{-1} and 3.89 mS.cm^{-1}. Following the initial impedance test, the cell underwent a chronopotentiometry test, as illustrated in **Figure 19 (b).** It's evident from the graph that a reduction in voltage amplitude occurred. To understand the nature of this phenomenon, the chronopotentiometry was interrupted, and a PEIS test was performed; the results are plotted in **Figure 19 (c).** The impedance profile, **Figure 19 (c)**, is clearly different from the first impedance, **Figure 19 (a)**, even exhibiting a negative region (green region) indicative of the cell's inductive behavior. This implies an induction of charge not due to magnetism but rather due to an increase in the capacitance of the cell at high frequencies. Additionally, there was an improvement in the cell's resistance/behavior, indicating a conditioning of the cell's performance. This improvement signifies progress in cell behavior. However, it's worth noting that the resistance remains relatively high, highlighting the need for interface enhancement and optimization in cell assembly.

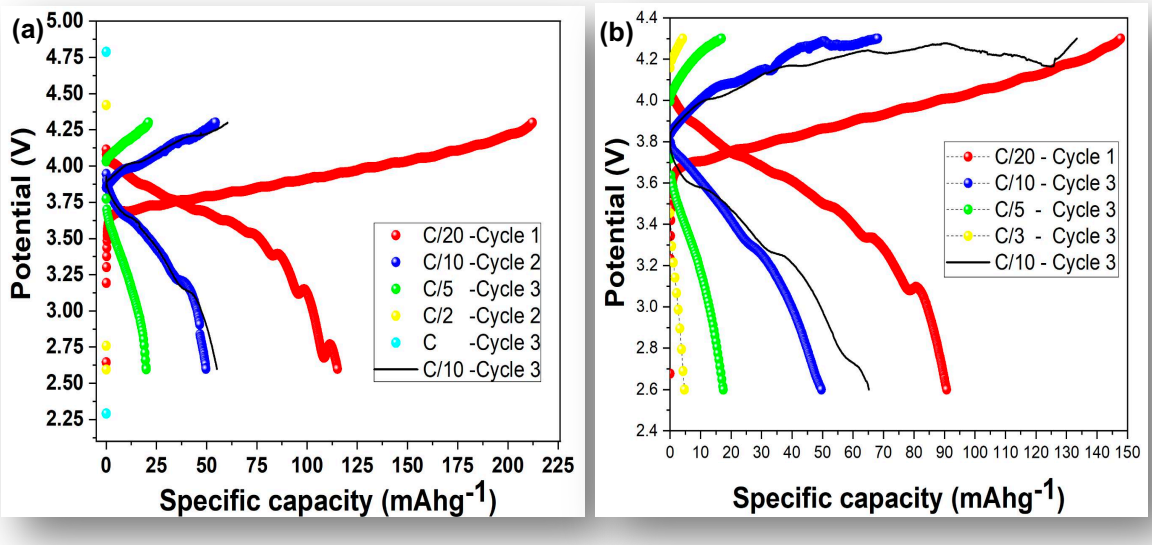

Figure 20. Charge/discharge cycling at 25 ºC for half (coin) cells with configuration: NMC/Li_6PS_5Cl/Li^0 at different C-rates.

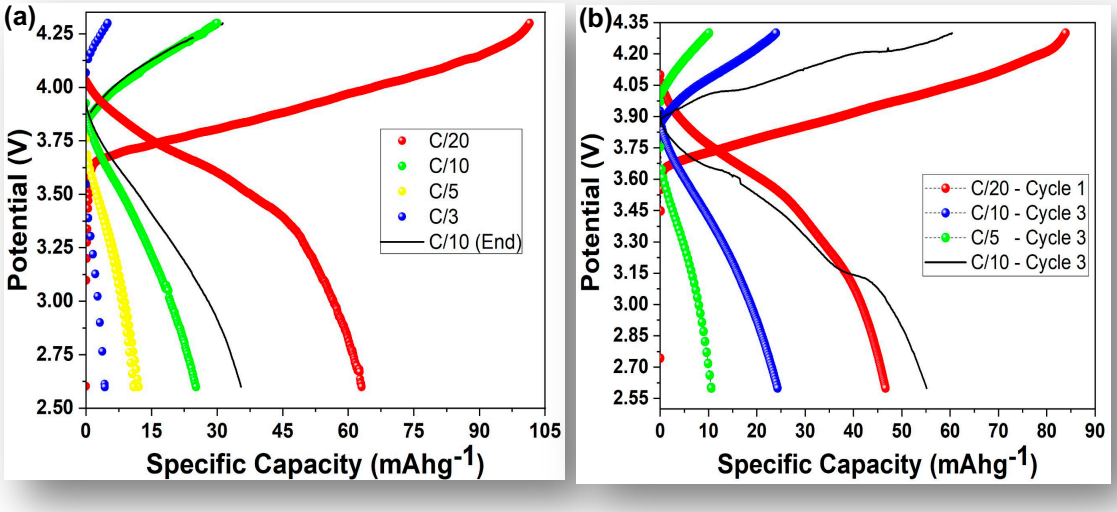

Figure 21. Charge/discharge cycling at 40 ºC for half (coin) cells with configuration: NMC/Li_6PS_5Cl/Li^0 at different C-rates.

The half cells contained lithium metal as the anode, while the cathode material was NMC 90-05-05. The electrolytes used in the half cells were the argyrodite Li_6PS_5Cl. **Figure 20** and **Figure 21** show the charge-discharge curves of four cells incorporating NMC as the cathode material, Li_6PS_5Cl as the solid electrolyte, and lithium metal as the anode material. Two of these cells underwent testing at 25 ºC **Figure 20 (a)** and **(b)**, while the other two were subjected to tests at 40 ºC **Figure 21 (a)** and **(b)**. Each of these cells underwent testing at different C-rates, and three cycles were conducted for each rate.

In **Figure 20** and **Figure 21**, the best cycle for each C-rate is plotted. Several conclusions can be drawn from both graphs. Except for the testing conducted under C/20, it is evident that the cycle with the highest discharge-specific capacity for each C-rate corresponds to the third cycle. This trend indicates a conditioning effect occurring within the cell and its materials; the same behavior was already observed in **Figure 19**. This observation is further supported by comparing the C/10 rates at the beginning and end of the testing procedure. At both temperatures, it's evident that the specific discharge capacity is higher for the C/10 rate after the test.

Initially, the cell's capacity was expected to increase with higher temperatures. However, contrary to this expectation, **Figure 22 (a)** and **(b)** clearly show that the cells tested at 25ºC exhibit higher capacities. Furthermore, when examining **Figure 20 (a)** and **(b)** in the discharge curve, it becomes apparent that there are oscillations during discharge at the C/20 rate. While this behavior has been observed before for the $Li_{2.99}Ba_{0.005}OCl$ electrolyte due to its ferroelectric nature, this phenomenon's nature in the Li_6PS_5Cl electrolyte has not been previously reported or attributed to any specific characteristic. Another notable conclusion is that the coulombic efficiency of the cell remains quite high

across all testing procedures. This is evident since the cell's specific discharge and charge capacities are equal, except for the first cycle at the C/20 rate. However eventhough some interesting results were obtained, the discharge capacity obtained are still far from the theoretical value of 192 $mAhg^{-1}$, **Figure 22** highlighting the need for further optimization.

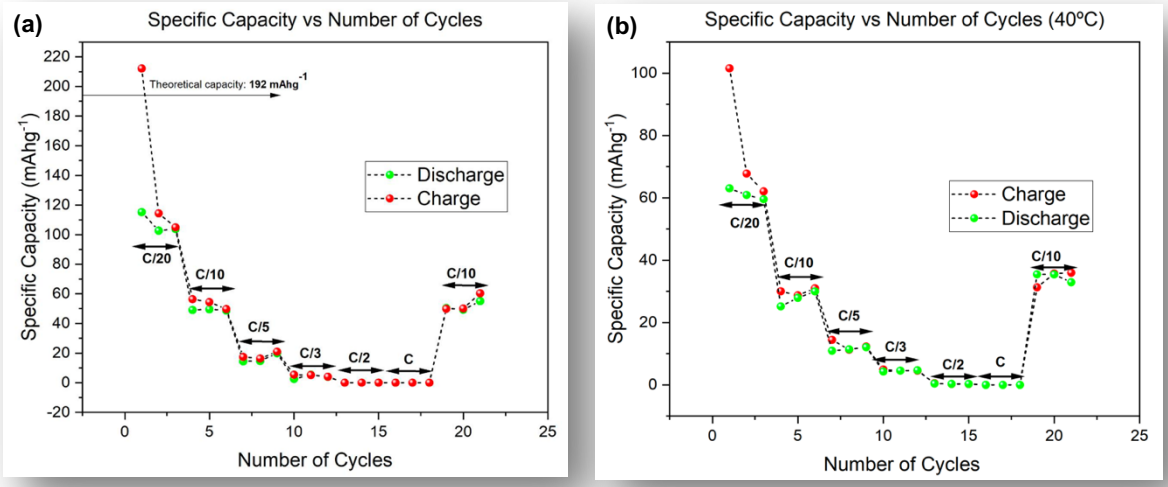

Figure 22. Specific capacity vs. number of cycles at (a) 25 ºC and (b) 40 ºC for coin cells with configuration: NMC/Li_6PS_5Cl/Li^0 at different C-rates.

4.3. Anode – Less

In this chapter strategies were explored to prove the viability of an anode-less cell containing the $Li_{2.99}Ba_{0.005}OCl$ electrolyte. The study started by trying to deposit lithium metal on the surface of the copper current collector. Following this to optimize the plating of lithium on the surface, as well as the overall performance of the cell, different oxide materials were selected as the protective layer of the anode current collector, a ZnO layer and a Li_2O layer. The results obtained will be discussed below.

4.3.1. Cu anode current collector

The charging and discharging protocol for anode-less cells holds significant importance, particularly because in the initial charging step lithium metal is deposited onto the anode current collector. Achieving a successful deposition requires finding an optimal balance between current and time. In the studies leading to this thesis, the approach chosen consisted in applying a low current during the initial charging steps, approximately 0.005 mA. This choice was made since using a higher current during the first cycles tends to lead to a rapid charging step, the maximum potential of 3.7 V for the LFP cathode is reached instantly and it's followed by instantaneous discharge. This behavior suggests that while the lithium ions reach the surface, they are unable to nucleate effectively on

the anode Cu current collector's surface. However, after the first cycles it is necessary to increase the current otherwise, the cell will never reach a high capacity due to the direct proportionality existent between these two physical quantities.

Another crucial step in the charge-discharge testing procedure involves introducing a constant voltage step during the charging process. This means that once the cell reaches 3.7 V, the cell's potential is fixed at this value and an establish a cut-off current is set. This step serves multiple purposes: it enhances the cell's capacity, since time favor the cell capacity and facilitates the even distribution of Li ions on the surface of the anode current collector. From a deposition perspective, this approach ensures that Li ions have sufficient time to access various parts of the anode current collector's surface, preventing/decreasing the formation of isolated islands of lithium, that can then lead to the formation of dendrites. The duration of this step can be limited by either a specific number of hours or the cell's maximum theoretical capacity. Another important experimental observation was the importance of time. In Section 4.2 the conditioning of the cells materials, since for the same C-rates the results were better for the last cycles, showing that the further time progresses the better results are obtained, **Figure 19**, **Figure 20** and **Figure 21**. This becomes more significant for anode-less cells, since initially there is no anode. In Section 4.2 after ensemble the cells were immediately put under a PEIS test, however for anode-less cells this is not possible due to the enormous resistance inside the cell. The cells after assembling should be put to rest for at least two weeks, to allow the formation of more stable interfaces between the materials that compose the cell.

The deposition of Li metal on the copper current collector, was already reported by MATΣR a group of research in each I had the opportunity to work during this thesis. In [152] an article co-authored by me, the deposition of Li-ions on the surface of the copper current collector was verified for when the cell was put to test at around 60 °C.

Following this work an experimental modification was introduced to explore the possibility of optimizing the deposition of Li metal onto the copper surface. Five dots of conductive glue were strategically placed on top of the anode current collector, with four positioned at the corners and one at the center, this cell underwent testing at room temperature, and the charge and discharge outcomes are depicted in **Figure 23**.

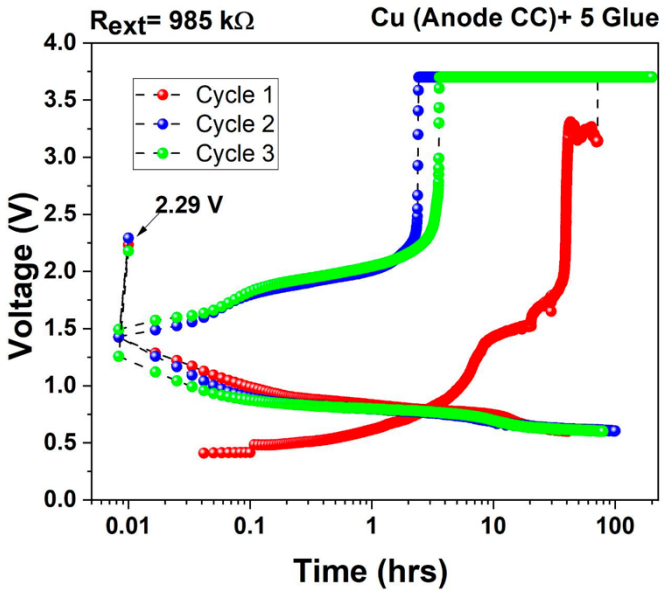

Figure 23. The potential difference for a pouch cell with configuration Cu + 5 dots of glue/$Li_{2.99}Ba_{0.005}OCl$ in cellulose/$LiFePO_4$/Cu while cycling with external resistance of 985 kΩ.

The discharge of the cell starts at a maximum discharge voltage of 2.29 V, with a maximum discharge time of 100 hours. A plateau region, from ≅ 1.4 V is observed until ≅ 0.7 V, for a maximum time of ≅ 11 hours. The maximum obtained discharge capacity for this cell is 0.06 mAh, **Table 3** . Comparing, the results obtained in this thesis with what was already reported in [152] for a cell containing only copper on the anode current collector the discharge capacities obtained for this cell are approximately equal to the ones reported for the cell of Cu tested at 60 °C, for an external resistance of 985 kΩ. Elevated temperatures have a stimulating effect on the kinetic behavior of the electrolyte's constituent particles. As a result, the electrolytes are more likely to reach their activation energy for the ionic conduction threshold compared to lower temperature conditions, therefore for lower temperatures a significantly lower discharge capacity is expected, but interestingly, this is not the case,**Table 3**.

However, upon comparing the results with those obtained in [152], it becomes evident that the discharge duration doubles for the battery tested at 25 °C. Since time is directly proportional to capacity, this can have a substantial impact the outcome result. Nevertheless, it's important to remember the role played by the interfaces within the cells. The interfaces between materials could be more conditioned, for this cell, than their counterparts in previous configurations [152]. Further investigations are necessary to take more definitive conclusions on whether the inclusion of the five dots of conductive

glue on the anode current collector significantly optimized the deposition of lithium, or not.

Table 3. Cu + 5 glue/$Li_{2.99}Ba_{0.005}ClO$ in cellulose/$LiFePO_4$/Cu pouch cell capacity throughout the charge discharge steps. Surface area A = 16 cm^2. All values were determined from voltages measured in the terminals of the external resistor.

Oxide Layer	Resistor	Cycle	Discharge Time (h)	Maximum Discharge potential (V)	Discharge Capacity (mAh)	Discharge Li mass (mg)	Discharge Li volume (mm^3)	Discharge Thickness (μm)
Cu + 5 glue	985 kΩ	1	40	2.23	0.03	0.008	0.015	0.009
		2	100	2.29	0.06	0.016	0.029	0.018
		3	79	2.18	0.05	0.013	0.024	0.015

4.3.2. ZnO layer on the anode current collector

To further enhance the deposition of Li metal onto the anode current collector, a layer of zinc oxide was meticulously applied on top of the collector. This innovation was initially documented in [152], an article co-authored as a significant outcome of this thesis research. In this section, cells featuring different dimensions of current collectors, but the same oxide layer used in [152], will be analyzed. These cells were hermetically sealed using an automated pilot line equipped with two distinct vacuum sealing machines: a pre-sealing unit and a sealing machine, ensuring the cells are securely closed under vacuum.

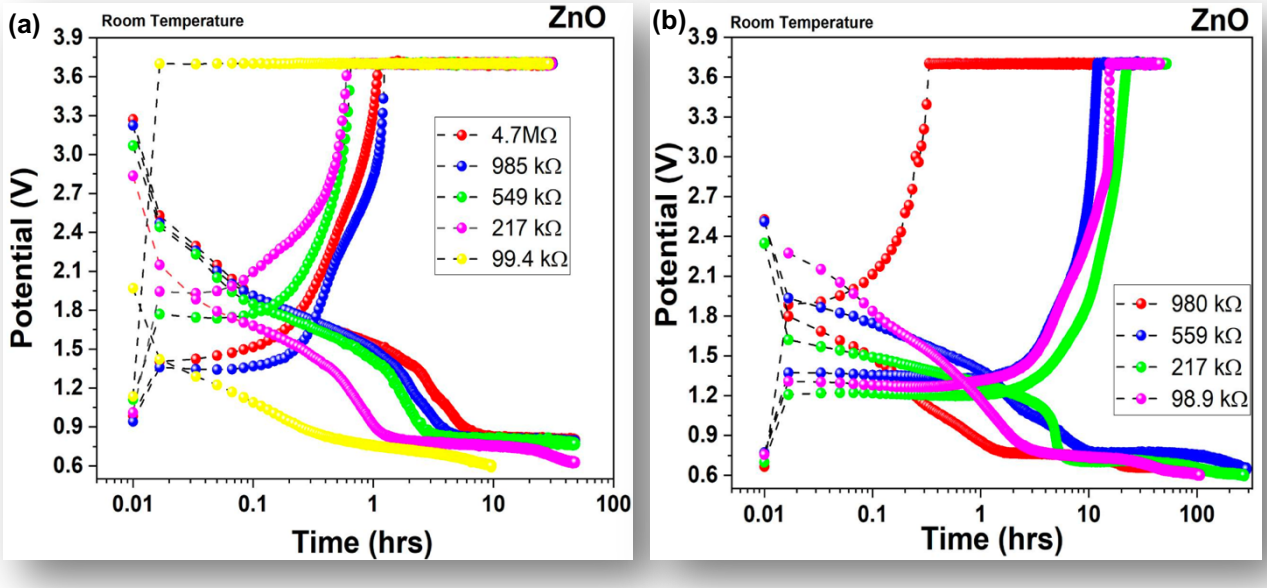

Figure 24. Potential difference for two pouch cells with configuration Cu/ZnO/$Li_{2.99}Ba_{0.005}ClO$ in cellulose/$LiFePO_4$/Cu while cycling with external resistance of **(a)** 4.7 MΩ; 985 kΩ; 549 kΩ; 217 kΩ and 99.4 kΩ; **(b)** 985 kΩ; 559 kΩ; 217 kΩ and 98.9 kΩ;

The results showcased in this section originate from two cells that were manufactured under equal conditions, employing the same configuration, materials, and dimensions.

In **Figure 24**, the charge and discharge curves for the two cells are plotted, with each graph depicting the array of resistances employed for testing each respective cell. The results plotted to the cycle displaying the best discharge capacity for each value of external resistance.

In **Figure 24 (a)**, with an external resistance of 4.7 MΩ, the battery initiated its discharge at a maximum voltage of 3.27 V, sustaining the discharge for approximately 48 hours. During this period, the maximum discharge capacity reached 3.25×10^{-4} mAh. When the external resistance was reduced to 985 kΩ, the battery began discharging at a slightly lower maximum voltage of 3.24V, still maintaining a discharge duration of about 48 hours, with an increased maximum discharge capacity of 0.041 mAh. Transitioning to a resistance of 549 kΩ, the battery's discharge commenced at a maximum voltage of 3.14V and continued for approximately 48 hours, achieving a higher maximum discharge capacity of 0.072 mAh. Further reduction in external resistance to 217 kΩ, the battery-initiated discharge at a maximum voltage of 2.83 V, persisting for roughly 48 hours, and demonstrated a significantly improved maximum discharge capacity of 0.159 mAh. In the final stage, with a resistance of 99.4 kΩ, the battery's discharge started at a maximum voltage of 1.97 V, continuing for about 10 hours, with a maximum discharge capacity of 0.067 mAh. Detailed information related to all the cycles for the cell of **Figure 24 (a)**, can be found in **Table 4**.

In **Figure 24 (b)**, with an external resistance of 985 kΩ, the second cell began discharging at maximum voltage of 2.53 V, maintaining a discharge duration of about 48 hours, with an increased maximum discharge capacity of 0.034 mAh. Transitioning to a resistance of 559 kΩ, the battery's discharge commenced at a maximum voltage of 2.51 V and continued for approximately 288 hours, achieving a higher maximum discharge capacity of 0.38 mAh. Further reduction in external resistance to 217 kΩ, the battery-initiated discharge at a maximum voltage of 2.35 V, persisting for roughly 273 hours, and demonstrated a significantly improved maximum discharge capacity of 0.82 mAh. In the final stage, with a resistance of 98.9 kΩ, the battery's discharge started at a maximum voltage of 2.71V, continuing for about 107 hours, with a maximum discharge capacity of 0.72 mAh. Detailed information related to all the cycles for the cell of **Figure 24 (b)**, can be found in **Table 5**.

In **Figure 24 (a)**, the cell best behavior occurred for a resistance of 217 kΩ, the battery's discharge reached a maximum of 0.159 mAh. For this resistance two plateau regions can be highlighted the first lasted for almost 1h, between 2.14V and 1.32 V, and a second plateau region that lasted for approximately 20h and stayed at an average potential of

0.75 V. The maximum thickness of Li metal deposited on the surface of the anode current collector for this resistance is 0.059 μm. For the cell of, **Figure 24 (b)**, the cells behavior was also better for a resistance of 217 kΩ. However, in this case the maximum discharge capacity was significantly higher 0.82 mAh reached over an impressive 273h. Here as in the previous case two plateau regions can be highlighted, the first plateau region lasted for approximately 4h between voltages of 1.62 V and 1.12 V The second plateau region lasted for 265 h at an average potential of 0.75 V. In this case the maximum thickness of Li metal deposited on the surface of the anode current collector is 0.294 μm. The estimation of the deposited lithium thickness followed an indirect approach. Initially, the calculation relied on the cell's capacity, from which it is possible to determine the number of moles of electrons. Given that the reduction of Li metal follows the equation $Li \rightarrow Li^{+} + e^{-}$, the moles of electrons are equal to the moles of both lithium ions and atoms, therefore using the relation between mass and number of moles it is possible to determine the mass of the deposited lithium. Next, leveraging the known density of lithium metal it is possible to calculate the volume of the deposited lithium, subsequently allowing the indirect deduction of the Li layer thickness.

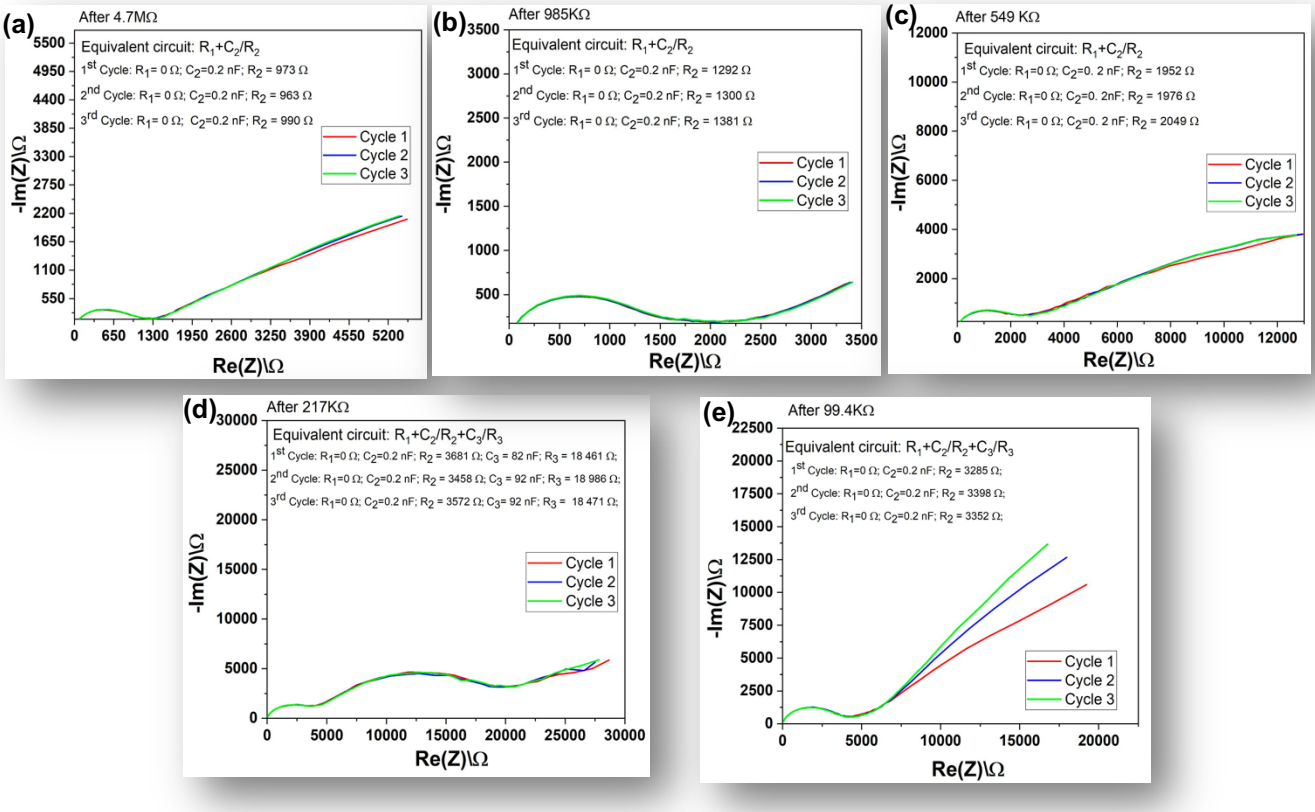

Figure 25. Potentiostatic Impedance Spectroscopy of a pouch cell featuring the Cu/ZnO/$Li_{2.99}Ba_{0.005}OCl$ in cellulose/$LiFePO_4$/Cu configuration. PEIS performed after: **(a)** 4.7 MΩ charge discharge testing; **(b)** 985 kΩ charge discharge testing; **(c)** 549 KΩ charge discharge testing; **(d)** 217 kΩ charge discharge testing and **(e)** 99.4KΩ charge discharge testing.

In **Figure 25**, PEIS tests performed for the cell of **Figure 24 (a)** are plotted. The PEIS test were performed at the end of the cycles of charge discharge for each value of external resistance. In **Figure 25 (a), (b), (c)** and **(e)**, the semicircle corresponds to the parallel between C_1 and R_2, where R_2 is the resistance of the capacitor conducing to the ionic conductivity of the electrolyte $\sigma = \frac{1}{R}\left(\frac{d}{A}\right)$. The capacitor is $ZnO/Li_{2.99}Ba_{0.005}OCl/LiFePO_4$, with Li^+ being the capacitor's mobile element with the highest natural frequency observed below 7 MHz. In **Figure 25 (d)**, a second semicircle appears that corresponds to R_3 parallel to C_2. In this case the semicircle likely corresponds to the electrical double layer capacitor EDLC $Li_{2.99}Ba_{0.005}OCl/Li$ spontaneously formed to equalize the electrochemical potentials between the electrolyte and the positive electrode, meanwhile with Li^+ accumulation at the anode side upon charge.

Table 4. $Cu/ZnO/Li_{2.99}Ba_{0.005}ClO$ in cellulose/$LiFePO_4$/Cu pouch cell, with surface area A = 13.5 cm^2. All values were determined from voltages measured in the terminals of the external resistor – Cell 1.

Oxide Layer	Resistor	Cycle	Discharge Time (h)	Maximum Discharge potential (V)	Discharge Capacity (mAh)	Discharge Li mass (mg)	Discharge Li volume (mm^3)	Discharge Thickness (μm)
ZnO	4.7 MΩ	1	48	3.20	3.25×10^{-4}	8.43×10^{-5}	1.57×10^{-4}	1.17×10^{-4}
		2	48	3.25	2.17×10^{-4}	5.63×10^{-5}	1.05×10^{-4}	7.79×10^{-5}
		3	48	3.27	1.65×10^{-4}	4.28×10^{-5}	8.00×10^{-4}	5.92×10^{-5}
	985 kΩ	1	48	3.24	0.041	0.011	0.020	0.015
		2	48	3.24	0.041	0.011	0.020	0.015
		3	48	3.22	0.041	0.011	0.020	0.015
	549 kΩ	1	48	3.14	0.071	0.018	0.034	0.025
		2	48	3.11	0.072	0.019	0.035	0.026
		3	48	3.07	0.072	0.019	0.035	0.026
	217 kΩ	1	48	2.83	0.159	0.041	0.077	0.057
		2	48	2.74	0.158	0.041	0.077	0.057
		3	47	2.54	0.153	0.040	0.074	0.055
	99.4 kΩ	1	10	1.97	0.067	0.017	0.032	0.024
		2	9	1.92	0.060	0.016	0.029	0.022
		3	6	1.82	0.041	0.011	0.020	0.015

Table 5. Cu/ZnO/$Li_{2.99}Ba_{0.005}ClO$ in cellulose/$LiFePO_4$/Cu pouch cell, with surface area A = 13.5 cm^2. All values were determined from voltages measured in the terminals of the external resistor – Cell 2.

Oxide Layer	Resistor	Cycle	Discharge Time (h)	Max Discharge potential (V)	Discharge Capacity (mAh)	Discharge Li mass (mg)	Discharge Li volume (mm^3)	Discharge Thickness (μm)
ZnO	**985 kΩ**	6	20	2.49	0.015	0.004	0.007	0.005
		7	48	2.53	0.034	0.009	0.016	0.012
		8	30	2.53	0.024	0.006	0.012	0.009
	559 kΩ	1	288	2.40	0.36	0.093	0.174	0.129
		2	288	2.44	0.37	0.096	0.179	0.133
		3	288	2.51	0.38	0.099	0.184	0.136
	217 kΩ	3	220	2.24	0.65	0.169	0.315	0.233
		4	172	2.28	0.52	0.135	0.252	0.187
		5	273	2.35	0.82	0.213	0.397	0.294
	98.9	6	87	2.80	0.60	0.156	0.291	0.215
	kΩ	7	103	2.79	0.70	0.181	0.339	0.251
		8	107	2.71	0.72	0.187	0.349	0.258

4.3.3. Li_2O layer on the anode current collector

In the context of this thesis, a second oxide, lithium oxide (Li_2O), is being explored as a potential candidate to enhance the nucleation process of lithium on the anode current collector. The results from two different cells, are ploted below. The first cell containes a Li_2O protective layer plus 5 dots of glue on the center and four corners of the anode current cullector, and was closed manuellly withouth vaccum. The sencond cell contained only a a Li_2O protective layer on the anode current collector and was closed hermetically using a pillot line for production of pouch cells that contains vaccum sealing machines - cell closed under vaccum.

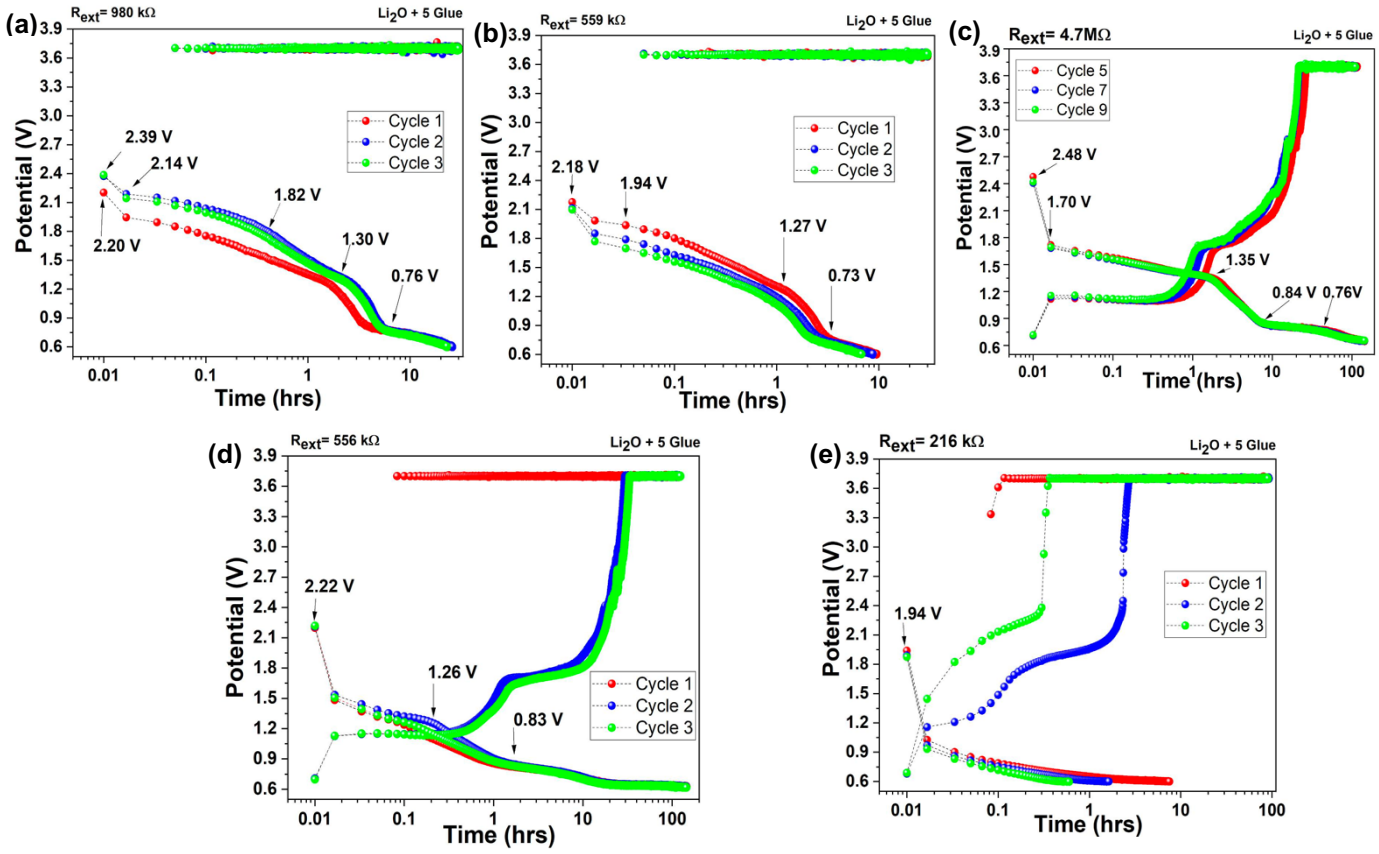

Figure 26. Potential difference for two pouch cells with configuration Cu/Li_2O + 5 dots of conductive glue /$Li_{2.99}Ba_{0.005}ClO$ in cellulose/$LiFePO_4$/Cu while cycling with external resistance of (**a)** 980 kΩ;**(b)** 559 kΩ;**(c)** 4.7 MΩ; **(d)** 556kΩ and **(e)** 216 kΩ

The pouch- cell containing a Li_2O protective layer plus 5 dots of glue on the center and four corners of the anode current cullector was put under charge and discharge testing with an external resistance of 980 kΩ, **Figure 26 (a)**. The battery started to discharge from a maximum potential of 2.15 V, during ≅ 20 hours. The highest capacity occurrs for the 2nd cyle, **Table 6**. At the end of the charge discharge cycling for this battery a potentiostatic impedance spectroscopy test was made, **Figure 27 (a)**. This test was performed during a charging step. In **Figure 27 (a)** the first the semicircle corresponds to the parallel between C_1 and R_2, where R_2 is the resistance of the capacitor conducing to the ionic conductivity of the electrolyte σ. The capacitor is $Li_2O/Li_{2.99}Ba_{0.005}OCl/LiFePO_4$, with Li^+ being the capacitor's mobile element with the highest natural frequency observed below 7 MHz. The second semicircle corresponds to R_3 parallel to C_2. In this case the semicircle likely corresponds to the electrical double layer capacitor EDLC $Li_{2.99}Ba_{0.005}OCl/Li$ spontaneously formed to equalize the electrochemical potentials between the electrolyte and the positive electrode, meanwhile with Li^+ accumulation at the anode side upon charge.

Moving forward, the external resistance was adjusted to 559 kΩ, maintaining a maximum discharge duration of 10 hours, **Figure 26 (b)**. The best performance of the cell occurred in 1st cycle. During this testing phase, the discharge process commenced at ≅ 2.18V. At the end of the third cycle for this cell there was a crash on the duration of the discharge time and the discharge capacity inferior was to the values obtained for the previous resistance **Table 6**. To understand what was occuring with the cell a second PEIS test was performed, **Figure 27 (b)**. Similarly to **Figure 27 (a)** two semicircles were observed, however the resistance values obtained in **Figure 27 (b)** are inferior to the results in **Figure 27 (a).** A reduction of the resistance of the cells, usually translates in an improvement of the interfaces of the materials and the optimization of the cell, however the results obtained during the charging and discharging test, specifically the capacity doesn't show that.

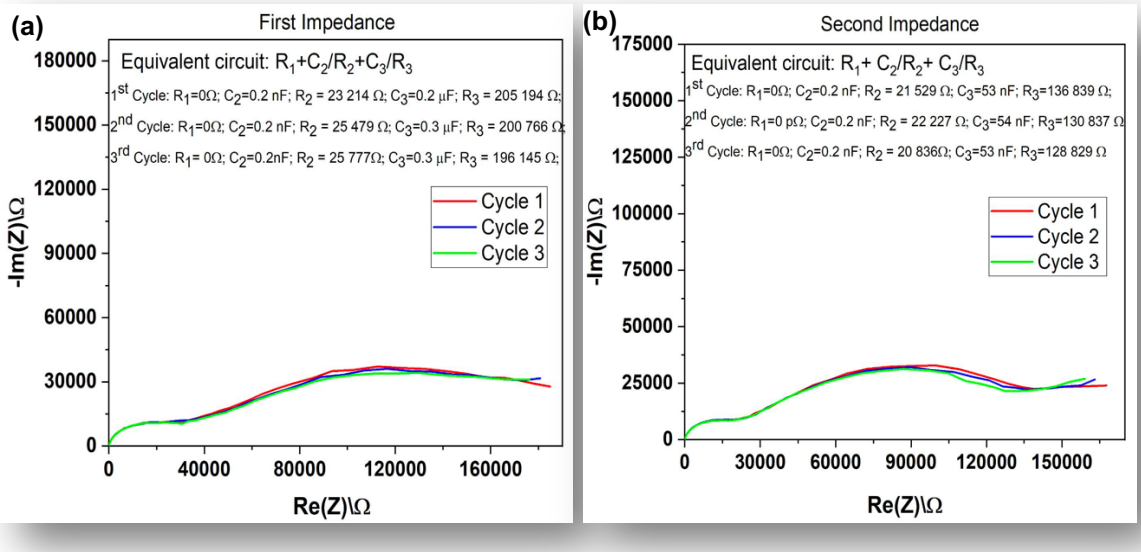

Figure 27. Potentiostatic Impedance Spectroscopy of a pouch cell featuring the Cu/Li_2O + 5 dots of conductive glue /$Li_{2.99}Ba_{0.005}OCl$ in cellulose/$LiFePO_4$/Cu configuration. PEIS test was performed after: **(a)** 980 kΩ charge/discharge testing; **(b)** 559 kΩ charge/discharge testing.

In order to improve performance the value of the external resistance was increased to 4.7MΩ, simulating a resting state for the battery, **Figure 26 (c).** This increase of resistance is the best way to simulate a resting stage of a battery since a very small (residual) current is flowing in the battery, allowing for the occurrence of polarization and feedback phenomena already reported for this electrolyte [108]. The battery underwent testing with a resistance of 4.7MΩ. The discharge duration lasted approximately 144 hours across all cycles depicted in , **Figure 26 (c),** showing a considerable improvement when compared with the previous resistance, **Table 6**. The cycle that exhibited the highest ionic conductivity was the fifth one with a value of 0.023 mAh. Another interinsting

point is that the discharge cycle starts at 1.70 V once again indicating that lithium has already been plated onto the collector.

Moving forward, the external resistance was adjusted to 556 kΩ, maintaining an average discharge duration of 144 hours, **Figure 26 (d).** The best performance of the cell occurred in 2nd cycle. During this testing phase, the discharge process commenced at ≅ 1.5 V. Notably, this resistance closely mirrors the one used in **Figure 26 (b)** at 559 kΩ. Nevertheless, the achieved results outperformed those obtained with the initial resistance, emphasizing a significant enhancement in the cell's interface. Finally a resistance of 216 kΩ was employed, **Figure 26 (e).** In this case the better cycle was the 1st displaying a discharge time of 8 h and discharge voltage of 1 V,**Table 6**.

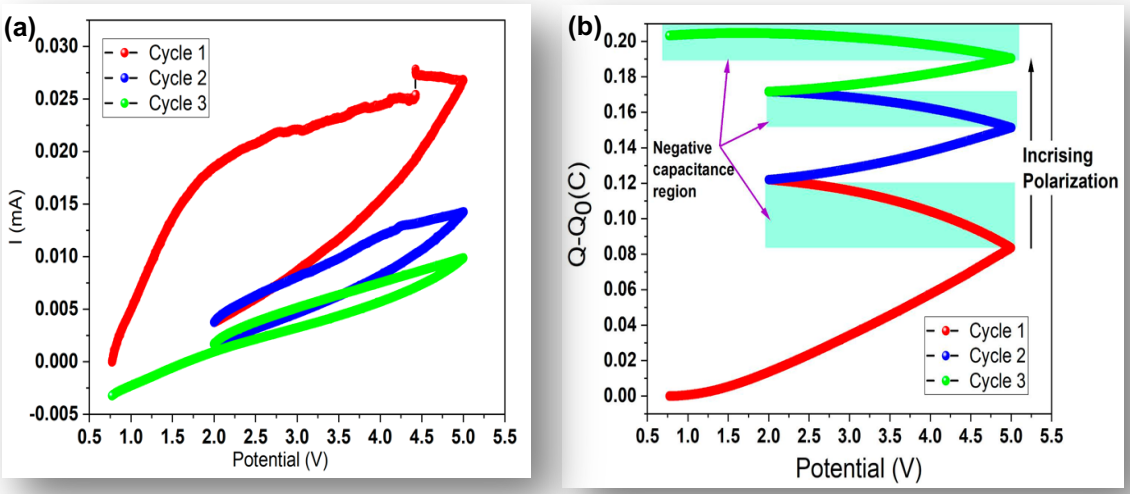

Figure 28. Cyclic Voltammetry test results: (a) I vs. V; (b) Q-Q_0(C) vs. Potential.

The final test performed with the cell containing Li_2O + 5 glue was cyclic voltammetry test **Figure 28**. In **Figure 28 (a)**, the absence of discernible peaks associated with reduction and oxidation reactions suggests that the cell operates in a manner similar to a capacitor. In **Figure 28 (b)**, the graph presents the relationship between capacitance and voltage. Polarization arises from the ratio of capacitance to the cell's surface area. From **Figure 28 (b)** several interesting conclusions can be taken. Firstly, with the time and number of cycles, the cell experiences a progressive rise in polarization, indicating that the cell is inducing and accumulating charge. Secondly, the process appears to be quasi-adiabatic; the curve/system doesn't hold hysteresis, indicating no energy loss. The persistent increase in polarization and energy preservation can be attributed to the phenomenon of negative capacitance, highlighted by the blue region in the graph, **Figure 28 (b)**.

The Li_2O cell closed under vacuum, underwent a series of charge and discharge testing, initially employing a 980 kΩ external resistor, **Figure 29 (a)**. Across all cycles the cell maintained a discharge period of 100 hours, **Table 7**. The graphical representation highlights the presence of three distinct plateau regions. The first plateau emerges within the voltage range of 1.81 V to 1.35 V, for approximately 2 hours. Subsequently, a second plateau becomes evident between 0.84 V and 0.76 V, for ≅ 18 h, followed by a final plateau extending from 0.76 V to 0.60 V of ≅ 60 h. Notably, the initial discharge voltage consistently hovers around the 2 V mark, a phenomenon achievable only if lithium has been effectively deposited onto the anode current collector. For this external resistance, the optimal discharge capacity is achieved during the 8th cycle. Detailed calculations associated with this performance can be found in **Table 7**.

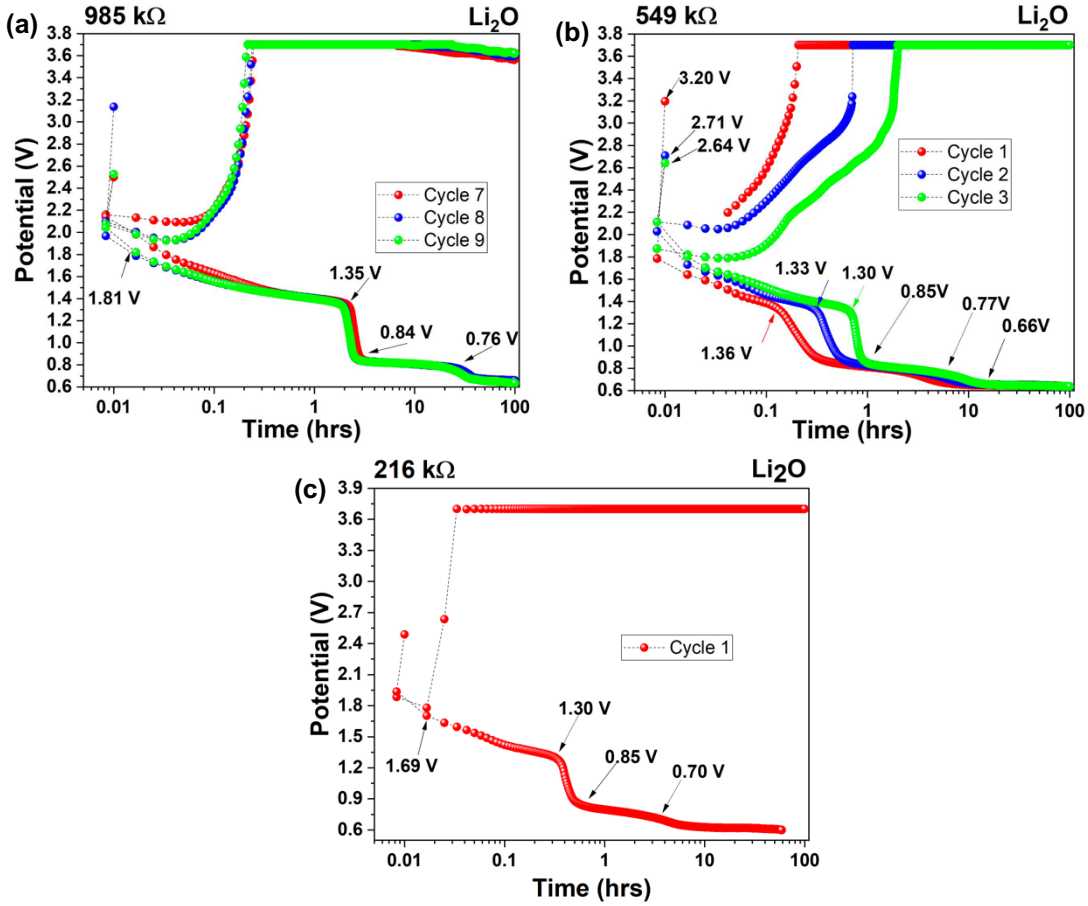

Figure 29. Potential difference of a pouch cell with configuration Cu/Li_2O/$Li_{2.99}Ba_{0.005}ClO$ in cellulose/$LiFePO_4$/Cu while cycling with external resistance of (a) 980 kΩ; (b) 556 kΩ and (c) 216 kΩ.

Following the earlier cycles, the battery was subsequently subjected to charge and discharge testing with an external resistance of 549 kΩ, as illustrated in **Figure 29 (b)**. Under this resistance the maximum discharge duration for all cycles remained consistent

at 100 hours. Notably, the cycle exhibiting the most exceptional performance is the 3rd cycle, characterized by the discharge capacity of 0.121 mAh, as detailed in **Table 7**. Like the observations made under the previously discussed external resistance, three distinct plateau regions are discernible. Specifically, in the case of the third cycle, an initial plateau is established within the voltage range of 1.80V to 1.30V, for about 1 hour. Subsequently, two additional plateau regions are identifiable between 0.85 V and 0.77 V, for 6 hours. The final plateau ends at 0.6 V, that lasts for about 85 hours. Concluding our testing regimen, the battery was subjected to a resistance of 216 kΩ, **Figure 29 (c).** Under this specific external resistance, the discharge cycle spanned a duration of 60 hours. The discharge process commenced at 1.69 V, with an initial plateau extending down to 1.30 V, for about 20 minutes. Subsequently, a second plateau occurred between the voltage range of 0.85 V to 0.70 V, ultimately culminating in a final plateau at 0.6 V.

Table 6. Cu/Li_2O + 5 dots of conductive glue /$Li_{2.99}Ba_{0.005}ClO$ in cellulose/$LiFePO_4$/Cu pouch cell capacity throughout the charge and discharge steps. Surface area A = 16 cm^2.

Oxide Layer	Resistor	Cycle	Discharge Time (h)	Maximum Discharge potential (V)	Discharge Capacity (mAh)	Discharge Li mass (mg)	Discharge Li volume (mm^3)	Discharge Thickness (μm)
Li_2O + 5 glue	980 kΩ	1	23	2.20	0.018	0.005	0.009	0.005
		2	26	2.37	0.021	0.005	0.010	0.006
		3	23	2.39	0.019	0.005	0.009	0.006
	559 kΩ	1	10	2.18	0.014	0.004	0.007	0.004
		2	9	2.11	0.013	0.003	0.006	0.004
		3	7	2.10	0.010	0.003	0.005	0.003
	4.7 MΩ	5	144	2.48	0.023	0.006	0.011	0.007
		7	144	2.41	0.023	0.006	0.011	0.007
		9	141	2.42	0.023	0.006	0.011	0.007
	556 kΩ	1	144	2.20	0.168	0.044	0.081	0.051
		2	144	2.21	0.169	0.044	0.082	0.051
		3	144	2.22	0.167	0.043	0.081	0.051
	216 kΩ	1	8	1.94	0.022	0.006	0.011	0.007
		2	2	1.89	0.005	0.001	0.002	0.002
		3	0.6	1.88	0.002	0.001	0.001	0.001

Table 7. Cu/Li_2O/$Li_{2.99}Ba_{0.005}ClO$ in cellulose/$LiFePO_4$/Cu pouch cell capacity throughout the charge and discharge steps. Surface area A = 13.5 cm^2.

Oxide Layer	Resistor	Cycle	Discharge Time (h)	Maximum Discharge potential (V)	Discharge Capacity (mAh)	Discharge Li mass (mg)	Discharge Li volume (mm^3)	Discharge Thickness (μm)
Li_2O	985 kΩ	7	100	2.5	0.073	0.019	0.035	0.026
		8	100	3.1	0.073	0.019	0.035	0.026
		9	100	2.5	0.072	0.019	0.035	0.026
	549 kΩ	1	100	3.2	0.119	0.031	0.058	0.043
		2	100	2.7	0.120	0.031	0.058	0.043
		3	100	2.6	0.121	0.031	0.059	0.043
	216 kΩ	1	60	2.5	0.172	0.045	0.083	0.062

In **Figure 30**, the best cycles for each cell are plotted side by side, considering the resistance used for each cell. The different assembling of the cell conditions conclusions on what protective layer is better (Li_2O + 5 dots or Li_2O). This limitation arises because the manually sealed cell (cell featuring the 5 dots of glue) was not hermetically sealed under vacuum, potentially allowing moisture to infiltrate the pouch cell case. This issue does not affect the cell containing only Li_2O, as it was sealed under vacuum. In both cases the cells exhibited superior performance for external resistance surrounding the 500 kΩ, in **Figure 30 (a)** 556 kΩ and, in **Figure 30 (b)** 549 kΩ. The discharge capacity is better for the cell in **Figure 30 (b)**, with a maximum capacity of 0.121 mAh, corresponding to discharge Li thickness of 0.043 μm.

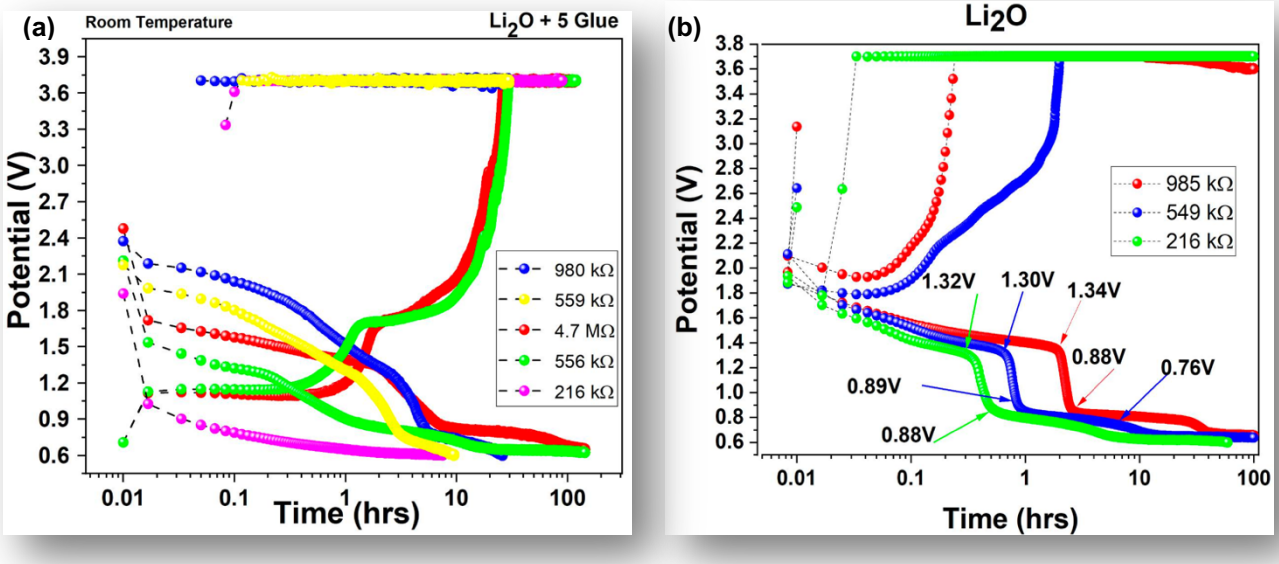

Figure 30. Potential difference of a pouch cell with configuration: **(a)** Cu/ Li_2O + 5 dots of conductive glue/ $Li_{2.99}Ba_{0.005}ClO$ in cellulose/$LiFePO_4$/Cu; and **(b)** Cu/Li_2O /$Li_{2.99}Ba_{0.005}ClO$ in cellulose/$LiFePO_4$/Cu, while cycling with external resistance.

Chapter 5

Conclusion

In this thesis, solid electrolyte implementation over different applications was explored. The research was structured into three distinct parts. Firstly, a comprehensive characterization of LFP and NMC materials was conducted using an atomic force microscope, which also enabled scanning Kelvin probe tests. Through these tests, the semiconductive nature of LFP became evident, notably marked by the observation of charge accumulation regions, as depicted in **Figure 18 (c).** Conversely, NMC cathodes exhibited a different behavior; there were no charge accumulation regions, **Figure 17(c).** This distinction arises from the fact that NMC, unlike LFP, is a conductor. The average chemical potential of the NMC material was experimentally determined using AFM - SKPM data to be approximately + 1.10 V vs. SHE, **Figure 17 (e)**, a value already calculated via simulations on another study not yet published.

The NMC active material was then used to assemble coin cells, featuring Li_6PS_5Cl as the electrolyte separator and lithium metal as the anode material. These cells were meticulously crafted as part of the PULSELiON European project. After assembly, the cells underwent rigorous charge-discharge tests across various C-rates. However, it became apparent that the discharge capacities of these cells fell short of the theoretically anticipated 192 $mAhg^{-1}$ for NMC 900505 material. The maximum discharge capacity for a cell tested at 25 °C was 120 $mAh.g^{-1}$, **Figure 20** and **Figure 22 (a)**, and for a cell tested at 40 °C, 60 $mAhg^{-1}$, **Figure 21** and **Figure 22** (b), this was an interesting conclusion on its own since the cells performed notably better when tested at 25 °C, as opposed to the anticipated superior performance at 40 °C. Higher temperatures increase the kinetic energy of the particle's electrolyte, reaching its activation energy of the ionic conductivity more easily than in lower temperatures. Further work still needs to be done to improve performance, highlighting the need for interface optimization.

Due to its exceptional capacity, Li metal is a promising choice for anodes to enhance conventional batteries. However, Li metal anode manufacturing possesses significant safety risks. Anode-less cells offer an innovative solution by eliminating these hazards. During the initial charge, Li metal deposits onto the anode current collector, creating the anode within the cell and eliminating the need for a pre-existing Li metal anode, **Section 2.6.** To improve environmental friendliness, battery technologies are shifting from cobalt-

containing cathode materials (NMC) to more known eco-friendly materials, such as LFP **Section 2.5.**

In the context of this thesis, anode-less cells were investigated, with LFP serving as the cathode's active material. To enhance nucleation, two distinct protective layers were examined for the anode current collector, namely zinc Oxide (ZnO) subsection and lithium oxide (Li_2O) subsection 4.3.3. The experiments started by assembling a cell in which lithium would be deposited into a bare anode current collector, placing only five dots of conductive glue strategically at the collector's four corners and center. This cell underwent charging and discharging cycles at a temperature of 25 °C, showcasing behavior only achievable if Li metal had been deposited. Notably, when an external resistance of 985 kΩ was applied, the cell exhibited a maximum discharge potential of 2.29 V, **Table 3**. Over a discharge period of up to 100 hours, the cell demonstrated a maximum discharge capacity of 0.06 mAh, corresponding to a Li discharge thickness of 0.018 µm, **Table 3**. When Zinc Oxide was utilized as the anode current collector, **Table 4** and **Table 5** ,the cell's optimal discharge performance was observed for an external resistance of 217 kΩ, as detailed in **Table 5**. This configuration allowed the cell to discharge for approximately 273 hours, with a maximum discharge capacity of 0.82 mAh corresponding to a Li discharge thickness of 0.296 µm —the highest value obtained in the work leading to this thesis. Furthermore, when lithium oxide was employed as the protective layer, the best performance was achieved with a resistance of 549 kΩ, as indicated in **Table 7**. This configuration resulted in a maximum discharge capacity of 0.121 mAh. Additionally, a cell featuring lithium oxide as the protective layer plus five conductive glue dots performed optimally with an external resistance of 556 kΩ, as shown in **Table 6**, achieving a maximum discharge capacity of 0.169 mAh. While further research and optimization are warranted, it is evident that the introduction of a protective layer is beneficial for enhancing the cell's performance. Notably, the Zinc Oxide cells displayed superior performance compared to the Lithium oxide cells, though additional investigations are necessary to ascertain which oxide offers the most favorable behavior.

"*What does the future hold for battery technology?"* The future of battery technology is marked by a clear imperative for higher power density, sustainability, and eco-friendliness. Focusing on prolonged cycle life and efficient material recycling is crucial to combat technological waste. This thesis highlights the significance of solid-state electrolytes as a critical pathway in battery evolution. Among various solid-state electrolytes, inorganic ferroelectric oxyhalides glassy electrolytes, like $Li_{2.99}Ba_{0.005}OCl$ from the $A_{2.99}Ba_{0.005}OCl$ – glass with A = Li, Na, and K family, exhibit promising

characteristics. This specific electrolyte is considered ideal for anode-less cells, thanks to its lithium-rich structure, offering extra Li-ion storage within the solid electrolyte and thereby enhancing cell performance, a conclusion also valid for their Na and K analogs.

Furthermore, ferroelectric materials hold game-changing potential due to their ability to display negative capacitance. Optimizing the already reported self-oscillations could revolutionize energy storage and enable self-chargeable devices [108] . The future of batteries hinges on these innovative developments in solid-state electrolytes and ferroelectric materials.

References

[1] T. B. Clarke, M. W. Glasscott, and J. E. Dick, “The Role of Oxygen in the Voltaic Pile,” *J Chem Educ*, vol. 98, no. 9, pp. 2927–2936, Sep. 2021, doi: 10.1021/acs.jchemed.1c00016.

[2] M. Li, J. Lu, Z. Chen, and K. Amine, “30 Years of Lithium-Ion Batteries,” *Advanced Materials*, vol. 30, no. 33. Wiley-VCH Verlag, Aug. 16, 2018. doi: 10.1002/adma.201800561.

[3] J. Wen, Y. Yu, and C. Chen, “A review on lithium-ion batteries safety issues: Existing problems and possible solutions,” *Materials Express*, vol. 2, no. 3. pp. 197–212, Sep. 2012. doi: 10.1166/mex.2012.1075.

[4] R. Sliz, P. Molaiyan, T. Fabritius, and U. Lassi, “Printed electronics to accelerate solid-state battery development,” *Nano Express*, vol. 3, no. 2, Jun. 2022, doi: 10.1088/2632-959X/ac5d8e.

[5] J. Wu, S. Liu, F. Han, X. Yao, and C. Wang, “Lithium/Sulfide All-Solid-State Batteries using Sulfide Electrolytes,” *Advanced Materials*, vol. 33, no. 6. Wiley-VCH Verlag, Feb. 01, 2021. doi: 10.1002/adma.202000751.

[6] J. C. Bachman *et al.*, “Inorganic Solid-State Electrolytes for Lithium Batteries: Mechanisms and Properties Governing Ion Conduction,” *Chemical Reviews*, vol. 116, no. 1. American Chemical Society, pp. 140–162, Jan. 13, 2016. doi: 10.1021/acs.chemrev.5b00563.

[7] V. Bocharova and A. P. Sokolov, “Perspectives for Polymer Electrolytes: A View from Fundamentals of Ionic Conductivity,” *Macromolecules*, vol. 53, no. 11. American Chemical Society, pp. 4141–4157, Jun. 09, 2020. doi: 10.1021/acs.macromol.9b02742.

[8] F. Danzi, M. Valente, S. Terlicka, and M. H. Braga, “Sodium and potassium ion rich ferroelectric solid electrolytes for traditional and electrode-less structural batteries,” *APL Mater*, vol. 10, no. 3, p. 31111, Mar. 2022, doi: 10.1063/5.0080054.

[9] M. H. Braga, J. A. Ferreira, V. Stockhausen, J. E. Oliveira, and A. El-Azab, “Novel Li _3 ClO based glasses with superionic properties for lithium batteries,” *J. Mater. Chem. A*, vol. 2, no. 15, pp. 5470–5480, 2014, doi: 10.1039/C3TA15087A.

[10] H. Chen *et al.*, “20 mS cm−1 Li-argyrodite solid electrolyte produced via facile high-speed-mixing,” *Chemical Communications*, 2023, doi: 10.1039/d3cc01387a.

[11] Y. Tanaka, K. Ueno, K. Mizuno, K. Takeuchi, T. Asano, and A. Sakai, “New Oxyhalide Solid Electrolytes with High Lithium Ionic Conductivity >10 mS cm−1 for All-Solid-State Batteries,” *Angewandte Chemie - International Edition*, vol. 62, no. 13, Mar. 2023, doi: 10.1002/anie.202217581.

[12] Y. Yu, Z. Wang, and G. Shao, “Theoretical design of double anti-perovskite Na6SOI2 as a super-fast ion conductor for solid Na+ ion batteries,” *J Mater Chem A Mater*, vol. 6, no. 40, pp. 19843–19852, 2018, doi: 10.1039/c8ta08412b.

[13] N. Kamaya *et al.*, “A lithium superionic conductor,” *Nat Mater*, vol. 10, no. 9, pp. 682–686, 2011, doi: 10.1038/nmat3066.

[14] P. Adeli *et al.*, “Boosting Solid-State Diffusivity and Conductivity in Lithium Superionic Argyrodites by Halide Substitution,” *Angewandte Chemie - International Edition*, vol. 58, no. 26, pp. 8681–8686, Jun. 2019, doi: 10.1002/anie.201814222.

[15] J. Yang *et al.*, “Ultrastable all-solid-state sodium rechargeable batteries,” *ACS Energy Lett*, vol. 5, no. 9, pp. 2835–2841, Sep. 2020, doi: 10.1021/acsenergylett.0c01432.

[16] Y. Sun *et al.*, “Rotational Cluster Anion Enabling Superionic Conductivity in Sodium-Rich Antiperovskite Na _3 OBH _4,” *J Am Chem Soc*, vol. 141, no. 14, pp. 5640–5644, Apr. 2019, doi: 10.1021/jacs.9b01746.

[17] Q. Ma, M. Guin, S. Naqash, C. L. Tsai, F. Tietz, and O. Guillon, “Scandium-substituted Na3Zr2(SiO4)2(PO4) prepared by a solution-assisted solid-state reaction method as sodium-ion conductors,” *Chemistry of Materials*, vol. 28, no. 13, pp. 4821–4828, Jul. 2016, doi: 10.1021/acs.chemmater.6b02059.

[18] M. Duchardt, U. Ruschewitz, S. Adams, S. Dehnen, and B. Roling, “Vacancy-Controlled Na+ Superion Conduction in Na11Sn2PS12,” *Angewandte Chemie - International Edition*, vol. 57, no. 5, pp. 1351–1355, Jan. 2018, doi: 10.1002/anie.201712769.

[19] Z. Zhang *et al.*, “A Self-Forming Composite Electrolyte for Solid-State Sodium Battery with Ultralong Cycle Life,” *Adv Energy Mater*, vol. 7, no. 4, Feb. 2017, doi: 10.1002/aenm.201601196.

[20] J. Liang *et al.*, “Site-Occupation-Tuned Superionic LixScCl3+ xHalide Solid Electrolytes for All-Solid-State Batteries,” *J Am Chem Soc*, vol. 142, no. 15, pp. 7012–7022, Apr. 2020, doi: 10.1021/jacs.0c00134.

[21] H. Kwak *et al.*, “Li+ conduction in aliovalent-substituted monoclinic Li2ZrCl6 for all-solid-state batteries: Li2+xZr1-xMxCl6 (M = In, Sc),” *Chemical Engineering Journal*, vol. 437, Jun. 2022, doi: 10.1016/j.cej.2022.135413.

[22] X. Li *et al.*, “Water-Mediated Synthesis of a Superionic Halide Solid Electrolyte,” *Angewandte Chemie*, vol. 131, no. 46, pp. 16579–16584, Nov. 2019, doi: 10.1002/ange.201909805.

[23] Y. Shao *et al.*, “A novel NASICON-based glass-ceramic composite electrolyte with enhanced Na-ion conductivity,” *Energy Storage Mater*, vol. 23, pp. 514–521, Dec. 2019, doi: 10.1016/j.ensm.2019.04.009.

[24] K. H. Park, K. Kaup, A. Assoud, Q. Zhang, X. Wu, and L. F. Nazar, “High-Voltage Superionic Halide Solid Electrolytes for All-Solid-State Li-Ion Batteries,” *ACS Energy Lett*, pp. 533–539, 2020, doi: 10.1021/acsenergylett.9b02599.

[25] A. Banerjee *et al.*, “ Na 3 SbS 4 : A Solution Processable Sodium Superionic Conductor for All-Solid-State Sodium-Ion Batteries ,” *Angewandte Chemie*, vol. 128, no. 33, pp. 9786–9790, Aug. 2016, doi: 10.1002/ange.201604158.

[26] H. Kwak *et al.*, “New Cost-Effective Halide Solid Electrolytes for All-Solid-State Batteries: Mechanochemically Prepared Fe3+-Substituted Li2ZrCl6,” *Adv Energy Mater*, vol. 11, no. 12, Mar. 2021, doi: 10.1002/aenm.202003190.

[27] T. Asano, A. Sakai, S. Ouchi, M. Sakaida, A. Miyazaki, and S. Hasegawa, “Solid Halide Electrolytes with High Lithium-Ion Conductivity for Application in 4 V Class Bulk-Type All-Solid-State Batteries,” *Advanced Materials*, vol. 30, no. 44, Nov. 2018, doi: 10.1002/adma.201803075.

[28] R. Schlem *et al.*, “Mechanochemical Synthesis: A Tool to Tune Cation Site Disorder and Ionic Transport Properties of Li3MCl6 (M = Y, Er) Superionic Conductors,” *Adv Energy Mater*, vol. 10, no. 6, Feb. 2020, doi: 10.1002/aenm.201903719.

[29] A. N. Guerreiro, B. A. Maia, H. Khalifa, M. C. Baptista, and M. H. Braga, “What Differentiates Dielectric Oxides and Solid Electrolytes on the Pathway toward

More Efficient Energy Storage?," *Batteries 2022, Vol. 8, Page 232*, vol. 8, no. 11, p. 232, Nov. 2022, doi: 10.3390/BATTERIES8110232.

[30] S. Boulineau, M. Courty, J. M. Tarascon, and V. Viallet, "Mechanochemical synthesis of Li-argyrodite Li 6PS 5X (X = Cl, Br, I) as sulfur-based solid electrolytes for all solid state batteries application," *Solid State Ion*, vol. 221, pp. 1–5, Aug. 2012, doi: 10.1016/j.ssi.2012.06.008.

[31] C. Yu *et al.*, "Facile Synthesis toward the Optimal Structure-Conductivity Characteristics of the Argyrodite Li6PS5Cl Solid-State Electrolyte," *ACS Appl Mater Interfaces*, vol. 10, no. 39, pp. 33296–33306, Oct. 2018, doi: 10.1021/acsami.8b07476.

[32] S. Yubuchi, S. Teragawa, K. Aso, K. Tadanaga, A. Hayashi, and M. Tatsumisago, "Preparation of high lithium-ion conducting Li6PS5Cl solid electrolyte from ethanol solution for all-solid-state lithium batteries," *J Power Sources*, vol. 293, pp. 941–945, Jun. 2015, doi: 10.1016/j.jpowsour.2015.05.093.

[33] R. Rajagopal, Y. Subramanian, Y. J. Jung, S. Kang, and K. S. Ryu, "Rapid Synthesis of Highly Conductive Li6PS5Cl Argyrodite-Type Solid Electrolytes Using Pyridine Solvent," *ACS Appl Energy Mater*, vol. 5, no. 8, pp. 9266–9272, Aug. 2022, doi: 10.1021/acsaem.2c01157.

[34] X. Tong, V. Thangadurai, and E. D. Wachsman, "Highly conductive Li garnets by a multielement doping strategy," *Inorg Chem*, vol. 54, no. 7, pp. 3600–3607, Apr. 2015, doi: 10.1021/acs.inorgchem.5b00184.

[35] D. J. Kalita, S. H. Lee, K. S. Lee, D. H. Ko, and Y. S. Yoon, "Ionic conductivity properties of amorphous Li-La-Zr-O solid electrolyte for thin film batteries," *Solid State Ion*, vol. 229, pp. 14–19, Dec. 2012, doi: 10.1016/j.ssi.2012.09.011.

[36] J. Tan and A. Tiwari, "Fabrication and characterization of Li7La3Zr 2O12 thin films for lithium ion battery," *ECS Solid State Letters*, vol. 1, no. 6, 2012, doi: 10.1149/2.013206ssl.

[37] K. Hayashi, K. Shima, and F. Sugiyama, "A Mixed Aqueous/Aprotic Sodium/Air Cell Using a NASICON Ceramic Separator," *J Electrochem Soc*, vol. 160, no. 9, pp. A1467–A1472, 2013, doi: 10.1149/2.067309jes.

[38] A. Jalalian-Khakshour, C. O. Phillips, L. Jackson, T. O. Dunlop, S. Margadonna, and D. Deganello, "Solid-state synthesis of NASICON (Na3Zr2Si2PO12) using

nanoparticle precursors for optimisation of ionic conductivity," *J Mater Sci*, vol. 55, no. 6, pp. 2291–2302, Feb. 2020, doi: 10.1007/s10853-019-04162-8.

[39] M. Niazmand, Z. Khakpour, and A. Mortazavi, "Electrochemical properties of nanostructure NASICON synthesized by chemical routes: A comparison between coprecipitation and sol-gel," *J Alloys Compd*, vol. 798, pp. 311–319, Aug. 2019, doi: 10.1016/j.jallcom.2019.05.170.

[40] J.-S. Lee, C.-M. Chang, Y. Il Lee, J.-H. Lee, and S.-H. Hong, "Spark Plasma Sintering (SPS) of NASICON Ceramics."

[41] A. M. Patel, J. K. Nørskov, K. A. Persson, and J. H. Montoya, "Efficient Pourbaix diagrams of many-element compounds," *Physical Chemistry Chemical Physics*, vol. 21, no. 45, pp. 25323–25327, 2019, doi: 10.1039/C9CP04799A.

[42] A. Jain *et al.*, "Formation enthalpies by mixing GGA and GGA $+$ U calculations," *Phys Rev B*, vol. 84, no. 4, p. 45115, Jul. 2011, doi: 10.1103/PhysRevB.84.045115.

[43] K. A. Persson, B. Waldwick, P. Lazic, and G. Ceder, "Prediction of solid-aqueous equilibria: Scheme to combine first-principles calculations of solids with experimental aqueous states," *Phys Rev B*, vol. 85, no. 23, p. 235438, Jun. 2012, doi: 10.1103/PhysRevB.85.235438.

[44] M. Aykol, S. S. Dwaraknath, W. Sun, and K. A. Persson, "Thermodynamic limit for synthesis of metastable inorganic materials," *Sci Adv*, vol. 4, no. 4, p. eaaq0148, Jul. 2023, doi: 10.1126/sciadv.aaq0148.

[45] I. Petousis *et al.*, "Data Descriptor: High-throughput screening of inorganic compounds for the discovery of novel dielectric and optical materials," *Sci Data*, vol. 4, Jan. 2017, doi: 10.1038/sdata.2016.134.

[46] M. De Jong, W. Chen, H. Geerlings, M. Asta, and K. A. Persson, "A database to enable discovery and design of piezoelectric materials," *Sci Data*, vol. 2, Sep. 2015, doi: 10.1038/sdata.2015.53.

[47] M. K. Horton, J. H. Montoya, M. Liu, and K. A. Persson, "High-throughput prediction of the ground-state collinear magnetic order of inorganic materials using Density Functional Theory," *NPJ Comput Mater*, vol. 5, no. 1, Dec. 2019, doi: 10.1038/s41524-019-0199-7.

[48] R. Tran *et al.*, “Data Descriptor: Surface energies of elemental crystals,” *Sci Data*, vol. 3, Sep. 2016, doi: 10.1038/sdata.2016.80.

[49] M. De Jong *et al.*, “Charting the complete elastic properties of inorganic crystalline compounds,” *Sci Data*, vol. 2, Mar. 2015, doi: 10.1038/sdata.2015.9.

[50] J. M. Munro, K. Latimer, M. K. Horton, S. Dwaraknath, and K. A. Persson, “An improved symmetry-based approach to reciprocal space path selection in band structure calculations,” *NPJ Comput Mater*, vol. 6, no. 1, Dec. 2020, doi: 10.1038/s41524-020-00383-7.

[51] K. Latimer, S. Dwaraknath, K. Mathew, D. Winston, and K. A. Persson, “Evaluation of thermodynamic equations of state across chemistry and structure in the materials project,” *NPJ Comput Mater*, vol. 4, no. 1, Dec. 2018, doi: 10.1038/s41524-018-0091-x.

[52] A. K. Singh *et al.*, “Electrochemical Stability of Metastable Materials,” *Chemistry of Materials*, vol. 29, no. 23, pp. 10159–10167, Dec. 2017, doi: 10.1021/acs.chemmater.7b03980.

[53] H. Zheng *et al.*, “Grain boundary properties of elemental metals,” *Acta Mater*, vol. 186, pp. 40–49, Mar. 2020, doi: 10.1016/j.actamat.2019.12.030.

[54] A. Wang *et al.*, “A framework for quantifying uncertainty in DFT energy corrections.” [Online]. Available: https://materialsproject.org/

[55] Ö. U. Kudu *et al.*, “A review of structural properties and synthesis methods of solid electrolyte materials in the Li2S − P2S5 binary system,” *J Power Sources*, vol. 407, pp. 31–43, Dec. 2018, doi: 10.1016/j.jpowsour.2018.10.037.

[56] J. F. M. Oudenhoven, L. Baggetto, and P. H. L. Notten, “All-solid-state lithium-ion microbatteries: A review of various three-dimensional concepts,” *Advanced Energy Materials*, vol. 1, no. 1. pp. 10–33, Jan. 01, 2011. doi: 10.1002/aenm.201000002.

[57] S. Zhao, W. Jiang, X. Zhu, M. Ling, and C. Liang, “Understanding the synthesis of inorganic solid-state electrolytes for Li ion batteries: Features and progress,” *Sustainable Materials and Technologies*, vol. 33, p. e00491, 2022, doi: https://doi.org/10.1016/j.susmat.2022.e00491.

[58] X. Li *et al.*, “Air-stable Li _3 InCl _6 electrolyte with high voltage compatibility for all-solid-state batteries,” *Energy Environ Sci*, vol. 12, no. 9, pp. 2665–2671, 2019, doi: 10.1039/C9EE02311A.

[59] L. Hoffart and D. M. Schleich, “Morphological Investigations on the Solid Electrolyte Li3.6Geo.6Vo.404 and Use in a Solid State Lithium Battery,” 1995.

[60] Y. Deng *et al.*, “Enhancing the Lithium Ion Conductivity in Lithium Superionic Conductor (LISICON) Solid Electrolytes through a Mixed Polyanion Effect,” *ACS Appl Mater Interfaces*, vol. 9, no. 8, pp. 7050–7058, Mar. 2017, doi: 10.1021/acsami.6b14402.

[61] S. Boulineau, M. Courty, J.-M. Tarascon, and V. Viallet, “Mechanochemical synthesis of Li-argyrodite Li6PS5X (X=Cl, Br, I) as sulfur-based solid electrolytes for all solid state batteries application,” *Solid State Ion*, vol. 221, pp. 1–5, Aug. 2012, doi: 10.1016/j.ssi.2012.06.008.

[62] I. Hanghofer *et al.*, “Substitutional disorder: Structure and ion dynamics of the argyrodites Li6PS5Cl, Li6PS5Br and Li6PS5I,” *Physical Chemistry Chemical Physics*, vol. 21, no. 16, pp. 8489–8507, 2019, doi: 10.1039/c9cp00664h.

[63] S. Boulineau, J.-M. Tarascon, J.-B. Leriche, and V. Viallet, “Electrochemical properties of all-solid-state lithium secondary batteries using Li-argyrodite Li6PS5Cl as solid electrolyte,” *Solid State Ion*, vol. 242, pp. 45–48, Jul. 2013, doi: 10.1016/j.ssi.2013.04.012.

[64] W. Xia *et al.*, “Antiperovskite Electrolytes for Solid-State Batteries,” *Chem Rev*, vol. 122, no. 3, pp. 3763–3819, Feb. 2022, doi: 10.1021/acs.chemrev.1c00594.

[65] S. T. Kong, H. J. Deiseroth, J. Maier, V. Nickel, K. Weichert, and C. Reiner, “Li6PO5Br and Li6PO5Cl: The first lithium-oxide-argyrodites,” *Z Anorg Allg Chem*, vol. 636, no. 11, pp. 1920–1924, Sep. 2010, doi: 10.1002/zaac.201000121.

[66] R. Murugan, V. Thangadurai, and W. Weppner, “Fast Lithium Ion Conduction in Garnet-Type Li7La3Zr2O12,” *Angewandte Chemie International Edition*, vol. 46, no. 41, pp. 7778–7781, 2007, doi: 10.1002/anie.200701144.

[67] J. B. Goodenough, H. Y.-P. Hong, and J. A. Kafalas, “Fast Na+-ion transport in skeleton structures,” *Mater Res Bull*, vol. 11, no. 2, pp. 203–220, 1976, doi: https://doi.org/10.1016/0025-5408(76)90077-5.

[68] Y. Zhang, H. Liu, Z. Xie, W. Qu, D. J. Freschi, and J. Liu, “Progress and Perspectives of Lithium Aluminum Germanium Phosphate-Based Solid Electrolytes for Lithium Batteries,” *Advanced Functional Materials*. John Wiley and Sons Inc, 2023. doi: 10.1002/adfm.202300973.

[69] Y. B. Rao, K. K. Bharathi, and L. N. Patro, “Review on the synthesis and doping strategies in enhancing the Na ion conductivity of Na3Zr2Si2PO12 (NASICON) based solid electrolytes,” *Solid State Ion*, vol. 366–367, Aug. 2021, doi: 10.1016/j.ssi.2021.115671.

[70] E. Heo, J. E. Wang, J. H. Yun, J. H. Kim, D. J. Kim, and D. K. Kim, “Improving Room Temperature Ionic Conductivity of Na3- xKxZr2Si2PO12Solid-Electrolytes: Effects of Potassium Substitution,” *Inorg Chem*, vol. 60, no. 15, pp. 11147–11153, Aug. 2021, doi: 10.1021/acs.inorgchem.1c01118.

[71] L. Ran *et al.*, “Sc, Ge co-doping NASICON boosts solid-state sodium ion batteries’ performance,” *Energy Storage Mater*, vol. 40, pp. 282–291, 2021, doi: https://doi.org/10.1016/j.ensm.2021.05.017.

[72] A. G. Belous, G. N. Novitskaya, S. V Polyanetskaya, and Y. I. Gornikov, “Investigation into complex oxides of La 2/3-x Li 3x TiO 3 composition,” *Izv. Akad. Nauk SSSR, Neorg. Mater*, vol. 23, no. 3, pp. 470–472, 1987.

[73] P. Birke, S. Scharner, R. A. Huggins, and W. Weppner, “Electrolytic Stability Limit and Rapid Lithium Insertion in the Fast-Ion-Conducting Li0.29La0.57TiO3 Perovskite-Type Compound,” *J Electrochem Soc*, vol. 144, no. 6, pp. L167–L169, Jun. 1997, doi: 10.1149/1.1837713.

[74] A. N. Guerreiro, B. A. Maia, H. Khalifa, M. C. Baptista, and M. H. Braga, “What Differentiates Dielectric Oxides and Solid Electrolytes on the Pathway toward More Efficient Energy Storage?,” *Batteries*, vol. 8, no. 11, Nov. 2022, doi: 10.3390/batteries8110232.

[75] C. Wei *et al.*, “Sb and O dual doping of Chlorine-rich lithium argyrodite to improve air stability and lithium compatibility for all-solid-state batteries,” *J Power Sources*, vol. 559, Mar. 2023, doi: 10.1016/j.jpowsour.2023.232659.

[76] A. Hayashi, K. Noi, A. Sakuda, and M. Tatsumisago, “Superionic glass-ceramic electrolytes for room-temperature rechargeable sodium batteries,” *Nat Commun*, vol. 3, 2012, doi: 10.1038/ncomms1843.

[77] A. Hayashi, K. Noi, N. Tanibata, M. Nagao, and M. Tatsumisago, “High sodium ion conductivity of glass-ceramic electrolytes with cubic Na3PS4,” *J Power Sources*, vol. 258, pp. 420–423, Jul. 2014, doi: 10.1016/j.jpowsour.2014.02.054.

[78] B. Ouyang, Y. Wang, Y. Sun, and G. Ceder, “Computational Investigation of Halogen-Substituted Na Argyrodites as Solid-State Superionic Conductors,” *Chemistry of Materials*, vol. 32, no. 5, pp. 1896–1903, Mar. 2020, doi: 10.1021/acs.chemmater.9b04541.

[79] L. Zhou, N. Minafra, W. G. Zeier, and L. F. Nazar, “Innovative Approaches to Li-Argyrodite Solid Electrolytes for All-Solid-State Lithium Batteries,” *Acc Chem Res*, vol. 54, no. 12, pp. 2717–2728, Jun. 2021, doi: 10.1021/acs.accounts.0c00874.

[80] H. J. Deiseroth *et al.*, “Li6PS5X: A class of crystalline Li-rich solids with an unusually high Li+ mobility,” *Angewandte Chemie - International Edition*, vol. 47, no. 4, pp. 755–758, 2008, doi: 10.1002/anie.200703900.

[81] T. Hwang *et al.*, “The crucial role of oxygen substitution in argyrodite solid electrolytes from the bulk to the surface under atmospheric conditions,” *J Mater Chem A Mater*, vol. 10, no. 32, pp. 16908–16919, Jul. 2022, doi: 10.1039/d2ta03649e.

[82] N. J. J. De Klerk and M. Wagemaker, “Diffusion Mechanism of the Sodium-Ion Solid Electrolyte Na3PS4 and Potential Improvements of Halogen Doping,” *Chemistry of Materials*, vol. 28, no. 9, pp. 3122–3130, May 2016, doi: 10.1021/acs.chemmater.6b00698.

[83] M. M. Islam, A. Al Maruf, J. Pokharel, and Y. Zhou, “Superhalogen-based Li-rich double antiperovskite Li6OS(BH4)2 as solid electrolyte,” *MRS Commun*, vol. 12, no. 6, pp. 1140–1146, Oct. 2022, doi: 10.1557/s43579-022-00290-6.

[84] B. Reuter, J. Pickardt, and K. Hardel, “Silbersulfidbromid Ag3SBr und Silbersulfidjodid Ag3SJ,” *Zeitschrift für Physikalische Chemie, vol. 56, no. 5_6,* , pp. 309–313, 1967.

[85] Yusheng Zhao, Luke Daemen, and Maria Helena Braga, “Anti-Perovskite Solid Electrolyte Compositions,” 2011 Accessed: Jul. 13, 2023. [Online]. Available: https://hdl.handle.net/10216/67190

[86] Y. Zhao and L. L. Daemen, “Superionic conductivity in lithium-rich anti-perovskites,” *J Am Chem Soc*, vol. 134, no. 36, pp. 15042–15047, Sep. 2012, doi: 10.1021/ja305709z.

[87] H. Fang and P. Jena, “Molecular Origin of Properties of Organic-Inorganic Hybrid Perovskites: The Big Picture from Small Clusters,” *Journal of Physical Chemistry Letters*, vol. 7, no. 8, pp. 1596–1603, May 2016, doi: 10.1021/acs.jpclett.6b00435.

[88] E. Ahiavi *et al.*, “Mechanochemical synthesis and ion transport properties of Na3OX (X = Cl, Br, I and BH4) antiperovskite solid electrolytes,” *J Power Sources*, vol. 471, Sep. 2020, doi: 10.1016/j.jpowsour.2020.228489.

[89] P. C. Tsai *et al.*, “Double Paddle-Wheel Enhanced Sodium Ion Conduction in an Antiperovskite Solid Electrolyte,” *Adv Energy Mater*, vol. 13, no. 7, Feb. 2023, doi: 10.1002/aenm.202203284.

[90] Q. Zhao *et al.*, “Design Principles for Rotational Cluster Anion [BH _4] ^− Promote Superionic Conductivity in Sodium-Rich Antiperovskite Na _3 OBH _4,” *The Journal of Physical Chemistry C*, vol. 126, no. 38, pp. 16546–16555, Sep. 2022, doi: 10.1021/acs.jpcc.2c05262.

[91] W. Hönle, B. Hettich, and A. Simon, “Darstellung und Kristallstrukturen von LiGaCl4 und LiGaI4/ Preparation and Crystal Structure of LiGaCL4 and LiGaI4,” vol. 42, no. 2, pp. 248–250, 1987, doi: doi:10.1515/znb-1987-0222.

[92] J. Park *et al.*, “Heat treatment protocol for modulating ionic conductivity via structural evolution of Li3-xYb1-xMxCl6 (M = Hf4+, Zr4+) new halide superionic conductors for all-solid-state batteries,” *Chemical Engineering Journal*, vol. 425, Dec. 2021, doi: 10.1016/j.cej.2021.130630.

[93] R. Kanno, Y. Takeda, M. Mori, and O. Yamamoto, “Ionic Conductivity and Structure of New Double Chloride Li6FeCl8 in the LiCl-FeCl2 System,” 1987.

[94] H. D. Lutz, A. Pfitzner, and J. K. Cockcroft, “Structural Phase Transition and Nonstoichiometry of Li2FeCl4—Neutron Diffraction Studies,” *J Solid State Chem*, vol. 107, no. 1, pp. 245–249, 1993.

[95] R. Kanno, Yasuo Takeda, Masashi Mori, and Osamu Yamamoto., “‘Ionic Conductivity and Structure of Double Chloride Li2ZnCl4 in the LiCl–ZnCl2 System.,’” *Chemistry Letters 18* , vol. 18, pp. 223-226., 1989.

[96] H. Kwak *et al.*, “Emerging Halide Superionic Conductors for All-Solid-State Batteries: Design, Synthesis, and Practical Applications,” *ACS Energy Letters*, vol. 7, no. 5. American Chemical Society, pp. 1776–1805, May 13, 2022. doi: 10.1021/acsenergylett.2c00438.

[97] Y. He *et al.*, “Recent developments and progress of halogen elements in enhancing the performance of all-solid-state lithium metal batteries,” *Energy Storage Mater*, vol. 49, pp. 19–57, Aug. 2022, doi: 10.1016/j.ensm.2022.03.043.

[98] W. Weppner and R. A. Huggins, “Ionic conductivity of solid and liquid LiAlCl4,” *J Electrochem Soc*, vol. 124, no. 1, p. 35, 1977.

[99] D. C. Ginnings and T. E. Phipps, “TEMPERATURE-CONDUCTANCE CURVES OF SOLID SALTS. III. HALIDES OF LITHIUM,” *J Am Chem Soc*, vol. 52, no. 4, pp. 1340–1345, Apr. 1930, doi: 10.1021/ja01367a006.

[100] R. Schlem, A. Banik, S. Ohno, E. Suard, and W. G. Zeier, “Insights into the Lithium Sub-structure of Superionic Conductors Li3YCl6and Li3YBr6,” *Chemistry of Materials*, vol. 33, no. 1, pp. 327–337, Jan. 2021, doi: 10.1021/acs.chemmater.0c04352.

[101] A. D. Sendek, E. D. Cubuk, E. R. Antoniuk, G. Cheon, Y. Cui, and E. J. Reed, “Machine Learning-Assisted Discovery of Solid Li-Ion Conducting Materials,” *Chemistry of Materials*, vol. 31, no. 2, pp. 342–352, Jan. 2019, doi: 10.1021/acs.chemmater.8b03272.

[102] K. Wang *et al.*, “A cost-effective and humidity-tolerant chloride solid electrolyte for lithium batteries,” *Nat Commun*, vol. 12, no. 1, Dec. 2021, doi: 10.1038/s41467-021-24697-2.

[103] W. G. Zeier, R. Schlem, A. Banik, M. Eckardt, and M. Zobel, “Na3−xEr1−xZrxCl6-A halide-based fast sodium-ion conductor with vacancy-driven ionic transport,” *ACS Appl Energy Mater*, vol. 3, no. 10, pp. 10164–10173, Oct. 2020, doi: 10.1021/acsaem.0c01870.

[104] J. Xu *et al.*, “New Halide-Based Sodium-Ion Conductors Na3Y2Cl9 Inversely Designed by Building Block Construction,” *ACS Appl Mater Interfaces*, May 2023, doi: 10.1021/acsami.3c01570.

[105] J. Liu, S. Wang, Y. Kawazoe, and Q. Sun, “A New Spinel Chloride Solid Electrolyte with High Ionic Conductivity and Stability for Na-Ion Batteries,” *ACS Mater Lett*, pp. 1009–1017, Apr. 2023, doi: 10.1021/acsmaterialslett.3c00119.

[106] T. Zhao, A. N. Sobolev, R. Schlem, B. Helm, M. A. Kraft, and W. G. Zeier, “Synthesis-Controlled Cation Solubility in Solid Sodium Ion Conductors Na2+xZr1-xInxCl6,” *ACS Appl Energy Mater*, Apr. 2023, doi: 10.1021/acsaem.3c00277.

[107] M. H. Braga, “Coherence in the Ferroelectric A3ClO (A = Li, Na) Family of Electrolytes,” *Materials*, vol. 14, no. 9, p. 2398, May 2021, doi: 10.3390/ma14092398.

[108] M. H. Braga, J. E. Oliveira, A. J. Murchison, and J. B. Goodenough, “Performance of a ferroelectric glass electrolyte in a self-charging electrochemical cell with negative capacitance and resistance,” *Appl Phys Rev*, vol. 7, no. 1, Mar. 2020, doi: 10.1063/1.5132841.

[109] M. Hoffmann, P. V. Ravindran, and A. I. Khan, “Why do ferroelectrics exhibit negative capacitance?,” *Materials*, vol. 12, no. 22. MDPI AG, Nov. 01, 2019. doi: 10.3390/ma12223743.

[110] L. Tu, X. Wang, J. Wang, X. Meng, and J. Chu, “Ferroelectric Negative Capacitance Field Effect Transistor,” *Advanced Electronic Materials*, vol. 4, no. 11. Blackwell Publishing Ltd, Nov. 01, 2018. doi: 10.1002/aelm.201800231.

[111] G. A. Salvatore, A. Rusu, and A. M. Ionescu, “Experimental confirmation of temperature dependent negative capacitance in ferroelectric field effect transistor,” *Appl Phys Lett*, vol. 100, no. 16, Apr. 2012, doi: 10.1063/1.4704179.

[112] A. I. Khan *et al.*, “Negative capacitance in a ferroelectric capacitor,” *Nat Mater*, vol. 14, no. 2, pp. 182–186, 2015, doi: 10.1038/nmat4148.

[113] B. M. Gomes, J. F. R. Moutinho, and M. H. Braga, “A perspective on the building blocks of a solid-state battery: from solid electrolytes to quantum power harvesting and storage,” *J Mater Chem A Mater*, 2024.

[114] M. Malik, K. H. Chan, and G. Azimi, “Review on the synthesis of LiNixMnyCo1-x-yO2 (NMC) cathodes for lithium-ion batteries,” *Materials Today Energy*, vol. 28. Elsevier Ltd, Aug. 01, 2022. doi: 10.1016/j.mtener.2022.101066.

[115] M. Li and J. Lu, “Cobalt in lithium-ion batteries,” *Science (1979)*, vol. 367, no. 6481, pp. 979–980, 2020.

[116] Y. Wei *et al.*, “Kinetics tuning of Li-ion diffusion in layered Li (Ni x Mn y Co z) O2,” *J Am Chem Soc*, vol. 137, no. 26, pp. 8364–8367, 2015.

[117] J. C. Stallard *et al.*, “Mechanical properties of cathode materials for lithium-ion batteries,” *Joule*, vol. 6, no. 5. Cell Press, pp. 984–1007, May 18, 2022. doi: 10.1016/j.joule.2022.04.001.

[118] M. S. Islam and C. A. J. Fisher, “Lithium and sodium battery cathode materials: computational insights into voltage, diffusion and nanostructural properties,” *Chem Soc Rev*, vol. 43, no. 1, pp. 185–204, 2014.

[119] A. K. Padhi, K. S. Nanjundaswamy, and J. B. Goodenough, “Phospho-olivines as positive-electrode materials for rechargeable lithium batteries,” *J Electrochem Soc*, vol. 144, no. 4, p. 1188, 1997.

[120] A. K. Padhi, K. S. Nanjundaswamy, and J. B. Goodenough, “LiFePO4: a novel cathode material for rechargeable batteries,” in *Electrochemical Society Meeting Abstracts*, 1996, p. 73.

[121] Z. Ahsan *et al.*, “Recent progress in capacity enhancement of LiFePO4 cathode for Li-ion batteries,” *Journal of Electrochemical Energy Conversion and Storage*, vol. 18, no. 1, p. 010801, 2021.

[122] A. Kumar *et al.*, “Optimization of electrochemical performance of lifepo4/c by indium doping and high temperature annealing,” *Inorganics (Basel)*, vol. 5, no. 4, p. 67, 2017.

[123] C. Gong, Z. Xue, S. Wen, Y. Ye, and X. Xie, “Advanced carbon materials/olivine LiFePO4 composites cathode for lithium ion batteries,” *J Power Sources*, vol. 318, pp. 93–112, 2016.

[124] L.-X. Yuan *et al.*, “Development and challenges of LiFePO 4 cathode material for lithium-ion batteries,” *Energy Environ Sci*, vol. 4, no. 2, pp. 269–284, 2011.

[125] W.-J. Zhang, “Structure and performance of LiFePO4 cathode materials: A review,” *J Power Sources*, vol. 196, no. 6, pp. 2962–2970, 2011.

[126] S. Suttison, K. Pengpat, U. Intatha, J. Fan, W. Zhang, and S. Eitssayeam, “Preparation of LFP-based cathode materials for lithium-ion battery applications,” *Mater Today Proc*, vol. 65, pp. 2347–2350, 2022.

[127] H. Cao *et al.*, “Application and prospects for using carbon materials to modify lithium iron phosphate materials used at low temperatures,” *New Carbon Materials*, vol. 37, no. 1, pp. 46–58, 2022.

[128] S.-P. Chen, D. Lv, J. Chen, Y.-H. Zhang, and F.-N. Shi, “Review on defects and modification methods of LiFePO4 cathode material for lithium-ion batteries,” *Energy & Fuels*, vol. 36, no. 3, pp. 1232–1251, 2022.

[129] J. Qian *et al.*, “Anode-Free Rechargeable Lithium Metal Batteries,” *Adv Funct Mater*, vol. 26, no. 39, pp. 7094–7102, Oct. 2016, doi: 10.1002/adfm.201602353.

[130] D. P. Wilkinson, H. Blom, K. Brandt, and D. Wainwright, “Effects of physical constraints on Li cyclability,” *J Power Sources*, vol. 36, no. 4, pp. 517–527, 1991.

[131] Y. Tian *et al.*, “Recently advances and perspectives of anode-free rechargeable batteries,” *Nano Energy*, vol. 78. Elsevier Ltd, Dec. 01, 2020. doi: 10.1016/j.nanoen.2020.105344.

[132] R. Zhang *et al.*, “Lithiophilic sites in doped graphene guide uniform lithium nucleation for dendrite-free lithium metal anodes,” *Angewandte Chemie*, vol. 129, no. 27, pp. 7872–7876, 2017.

[133] Z. Xie *et al.*, “Anode-free rechargeable lithium metal batteries: Progress and prospects,” *Energy Storage Materials*, vol. 32. Elsevier B.V., pp. 386–401, Nov. 01, 2020. doi: 10.1016/j.ensm.2020.07.004.

[134] J. Wang *et al.*, “Fundamental study on the wetting property of liquid lithium,” *Energy Storage Mater*, vol. 14, pp. 345–350, 2018.

[135] A. Pei, G. Zheng, F. Shi, Y. Li, and Y. Cui, “Nanoscale nucleation and growth of electrodeposited lithium metal,” *Nano Lett*, vol. 17, no. 2, pp. 1132–1139, 2017.

[136] K. Yan *et al.*, “Selective deposition and stable encapsulation of lithium through heterogeneous seeded growth,” *Nat Energy*, vol. 1, no. 3, pp. 1–8, 2016.

[137] J. Jung, D. Y. Hwang, I. Kristanto, S. K. Kwak, and S. J. Kang, “Deterministic growth of a sodium metal anode on a pre-patterned current collector for highly rechargeable seawater batteries,” *J Mater Chem A Mater*, vol. 7, no. 16, pp. 9773–9781, 2019.

[138] B. J. Neudecker, N. J. Dudney, and J. B. Bates, “‘Lithium-Free’ thin-film battery with in situ plated Li anode,” *J Electrochem Soc*, vol. 147, no. 2, p. 517, 2000.

[139] J. B. Bates, N. J. Dudney, B. Neudecker, A. Ueda, and C. D. Evans, “Thin-film lithium and lithium-ion batteries,” *Solid State Ion*, vol. 135, no. 1–4, pp. 33–45, 2000.

[140] S.-H. Lee, P. Liu, and C. E. Tracy, “Lithium thin-film battery with a reversed structural configuration SS/Li/Lipon/Li x V 2 O 5/Cu,” *Electrochemical and solid-state letters*, vol. 6, no. 12, p. A275, 2003.

[141] A. S. Westover, N. J. Dudney, R. L. Sacci, and S. Kalnaus, “Deposition and confinement of Li metal along an artificial lipon–lipon interface,” *ACS Energy Lett*, vol. 4, no. 3, pp. 651–655, 2019.

[142] T. A. Zegeye, W.-N. Su, F. W. Fenta, T. S. Zeleke, S.-K. Jiang, and B. J. Hwang, “Ultrathin Li6. 75La3Zr1. 75Ta0. 25O12-based composite solid electrolytes laminated on anode and cathode surfaces for anode-free lithium metal batteries,” *ACS Appl Energy Mater*, vol. 3, no. 12, pp. 11713–11723, 2020.

[143] M. J. Wang, E. Carmona, A. Gupta, P. Albertus, and J. Sakamoto, “Enabling ‘lithium-free’ manufacturing of pure lithium metal solid-state batteries through in situ plating,” *Nat Commun*, vol. 11, no. 1, p. 5201, 2020.

[144] Y.-G. Lee *et al.*, “High-energy long-cycling all-solid-state lithium metal batteries enabled by silver–carbon composite anodes,” *Nat Energy*, vol. 5, no. 4, pp. 299–308, 2020.

[145] S. H. Park *et al.*, “Designing 3D Anode Based on Pore-Size-Dependent Li Deposition Behavior for Reversible Li-Free All-Solid-State Batteries,” *Advanced Science*, vol. 9, no. 28, p. 2203130, 2022.

[146] D. Gu, H. Kim, J.-H. Lee, and S. Park, “Surface-roughened current collectors for anode-free all-solid-state batteries,” *Journal of Energy Chemistry*, vol. 70, pp. 248–257, 2022.

[147] H. Asano *et al.*, “Enhancing the reversibility of Li deposition/dissolution in sulfur batteries using high-concentration electrolytes to develop anode-less batteries with lithium sulfide cathode,” *J Power Sources*, vol. 554, p. 232323, 2023.

[148] O. Lohrberg *et al.*, “Benchmarking and Critical Design Considerations of Zero-Excess Li-Metal Batteries,” *Adv Funct Mater*, p. 2214891, 2023.

[149] O. J. Dahunsi *et al.*, “Anode-free Na metal batteries developed by nearly fully reversible Na plating on the Zn surface,” *Nanoscale*, vol. 15, no. 7, pp. 3255–3262, 2023.

[150] S. Liu, K. Jiao, and J. Yan, “Prospective strategies for extending long-term cycling performance of anode-free lithium metal batteries,” *Energy Storage Mater*, 2022.

[151] A. N. Guerreiro, M. C. Baptista, B. A. Maia, and M. H. Braga, “Interfacial Chemistry with ZnO: In Operando Work Functions in Heterocells,” *ACS Appl Energy Mater*, vol. 5, no. 8, pp. 9811–9822, 2022.

[152] M. C. Baptista *et al.*, “Conditioning Solid-State Anode-Less Cells for the Next Generation of Batteries,” *Batteries*, vol. 9, no. 8, p. 402, Aug. 2023, doi: 10.3390/batteries9080402.

[153] Y. Abe, N. Hori, and S. Kumagai, “Electrochemical Impedance Spectroscopy on the Performance Degradation of LiFePO 4 /Graphite Lithium-Ion Battery Due to Charge-Discharge Cycling under Different C-Rates”, doi: 10.3390/en12234507.

[154] N. Magalhães, B. Arouca Maia, M. Helena Braga, R. M. Santos, N. Correia, and E. Cunha, “Glass Fiber Reinforced Epoxy-Amine Thermosets and Solvate IL: Towards New Composite Polymer Electrolytes for Lithium Battery Applications,” 2023, doi: 10.3390/ijms241310703.

[155] V. Baheti, R. Abbasi, and J. Militky, “Ball milling of jute fibre wastes to prepare nanocellulose,” *World Journal of Engineering*, vol. 9, no. 1, pp. 45–50, Mar. 2012, doi: 10.1260/1708-5284.9.1.45.

[156] J. Mittra *et al.*, “Role of substrate temperature in the pulsed laser deposition of zirconium oxide thin film,” in *Materials Science Forum*, Trans Tech Publications Ltd, 2012, pp. 757–761. doi: 10.4028/www.scientific.net/MSF.710.757.

[157] M. Saeed, Y. Alshammari, S. A. Majeed, and E. Al-Nasrallah, “Chemical Vapour Deposition of Graphene—Synthesis, Characterisation, and Applications: A Review,” *Molecules*, vol. 25, no. 17. MDPI AG, Sep. 01, 2020. doi: 10.3390/molecules25173856.

Attachment 1

In [1]:

```
# Import all the required libraries
import numpy as np
import pandas as pd
import matplotlib.pyplot as plt
from mpl_toolkits.mplot3d import axes3d
from matplotlib import cm
from matplotlib.colors import ListedColormap
from matplotlib.colors import LinearSegmentedColormap
```

Coherent Solutions - DSG Equation

The Coherent solutions of the DSG equation are given by:

$$U(x,t) = \frac{0.1}{cosh((2(\gamma(x-\varpi t))))} cos(0.8(\gamma(x-\varpi t) - (3+\Omega^2))\gamma(t$$

,where

$$\xi = \gamma(x-\varpi t)$$

$$\rho(\xi) = \frac{A}{cosh(B*\xi)}$$

$$\Omega = \frac{8\lambda+1}{12\lambda(1+2\lambda)}\rho(\xi)$$

In [2]:

```
# Constant Variabels - used to perform th
A = 2
B = 2/19
lamb = -0.11
```

In [3]:

```
# Defining Functions re      to calc      the DSG Equation

def xi_func(gama,      t):
    return(gama*      be      )

def rho_func(g      x,beta,      ):
    return(A/np.      (B*xi_func(gama,x,beta,t)))

def      g_fu      ma,x      ta,t,A,B,lamb):
    eturn((8      mb+1)/(12*lamb*(1+2*lamb))*(rho_func(gama,x,beta,t,A,B))**2)


def U(      ta,A,B,lamb,x,t): # Coherent solutions - Function
    w= 1/np.cosh(2*(gama*(x-beta*t)))
    p=np.cos(0.8*(gama*(x-beta*t)-(3+omeg_func(gama,x,beta,t,A,B,lamb)**2))*gama*(t-beta
    u=0.1*w*p
    return (u)
```

In [4]:

```
# Define the 3 colors you want to use in your gradient
color1 = (0.4, 0.0, 0.0, 1.0)  # RGB value for #660000
color2 = (0.71, 0.54, 0.0, 1.0)   # RGB value for #B58900
color3 = (0.94, 0.77, 0.75, 1.0)   # RGB value for #F0C5BE

# Define the color gradient using the LinearSegmentedColormap class
colors = [color1, color2, color3]
cmap_name = 'my_custom_cmap'
cm = LinearSegmentedColormap.from_list(cmap_name, colors)

#Graphics Font
font = {'family': 'Calibri', 'size': 14,'weight': 'bold'}
```

In [5]:

```
#Experimental Data
data=pd.read_csv('SKP_Frame_up_Line_midle_closer_Cu_Loc_3_FRAME_3_UP_DIR_AL_to_Cul_Sampl
```

Confidential

In [6]:

```
# Data obtained experimentaly
Yf=data.iloc[:,0].to_numpy() # X (micro-meters)
V=data.iloc[:,1].to_numpy() # Potential difference

#------------------------------------------------ Ploting experimental data 2D ---------
fig = plt.figure(figsize=(16,10))
plt.plot (Yf,V) # 2D plot
plt.xlabel ('x(um)')
plt.ylabel ('V(v)')
plt.grid()
plt.show()

#------------------------------------------------ Ploting experimental data 3D ----------

X=np.linspace(-4,4,len(Yf)) # Create Time variable
tlol,xlol=np.meshgrid(X,Yf) # time and x grid
#Creating a grid with the diferential potential by diving and multiplying by th ame pa
Zlol=xlol*V
Zlol=Zlol/xlol

# Customize the plot
fig = plt.figure(figsize=(16,10))
ax = fig.add_subplot(111, projection='3d')
ax.set_xlabel('Time')
ax.set_ylabel('x')
ax.set_zlabel('Voltage')
surf = ax.plot_surface(tlol, xlol, Zlol, rstride=8, cstride=8 width=1 ha=0.8, c
fig.colorbar(surf, ax=ax, shrink=0.4, aspect=10,location='righ =0.1)
ax.set_xlabel('time (a.u.)',font, labelpad=5)
ax.set_ylabel('x (a.u)',font, labelpad=7)
ax.set_zlabel('Potential Energy (V)',font, labelpad
ax.tick_params(axis='x', pad=0.5)
ax.tick_params(axis='z', pad=5)
ax.grid(False)
plt.show()
```

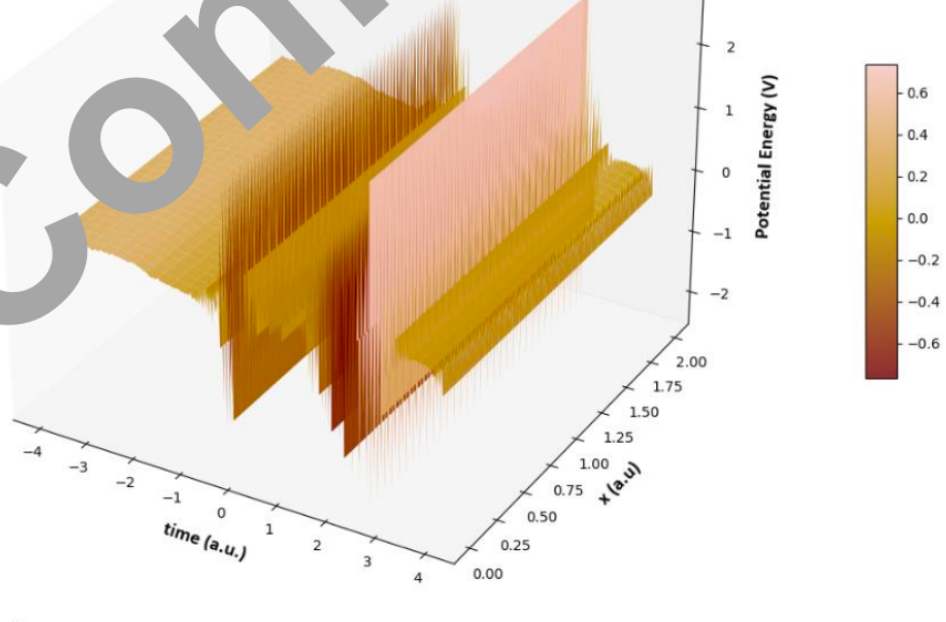

Confidential

In [7]:

```
# Interactions

#---------------------------//----------------------------- #
Beta1=0.05
Yf1=data.iloc[:,0].to_numpy()
X1=np.linspace(-40,60,len(Yf1))

t1,xl1=np.meshgrid(X1,Yf1)
u1=U(1/np.sqrt(1-Beta1**2) ,Beta1,A,B,lamb,xl1,t1)
#--------------------------- // --------------------------- #

Beta2=0.80
Yf2=data.iloc[:,0].to_numpy()
X2=np.linspace(-40,60,len(Yf2))

t2,xl2=np.meshgrid(X2,Yf2)
u2=U(1/np.sqrt(1-Beta2**2) ,Beta2,A,B,lamb,xl2,t2)

#-------------------------------------- // -----------------#
# FINAL Interaction solution
u=u2
u[0:5]=-u2[0:5]/2 + u2[0:5]/2
u[5:100]=u[5:100]-u1[5:100]
u[100:,]=-u2[100:,]/2 + u2[100:,]/2

# ------------------------------- 3D Surface plot representa
fig = plt.figure(figsize=(12,10))
ax = fig.add_subplot(111, projection='3d')
surf = ax.plot_surface(t1, xl1, u, rstride=
cset = ax.contourf(t1, xl1, u, zdir='z',
fig.colorbar(surf, ax=ax, shrink=0.4, aspec
ax.set_xlabel('time (a.u.)',font, labelpad=5)
ax.set_ylabel('x (a.u.)',font, labelpad=7
ax.set_zlabel('Potential Energy (a.u.)'
ax.tick_params(axis='x', pad=
ax.tick_params(axis='z',
ax.grid(False)
plt.show()
```

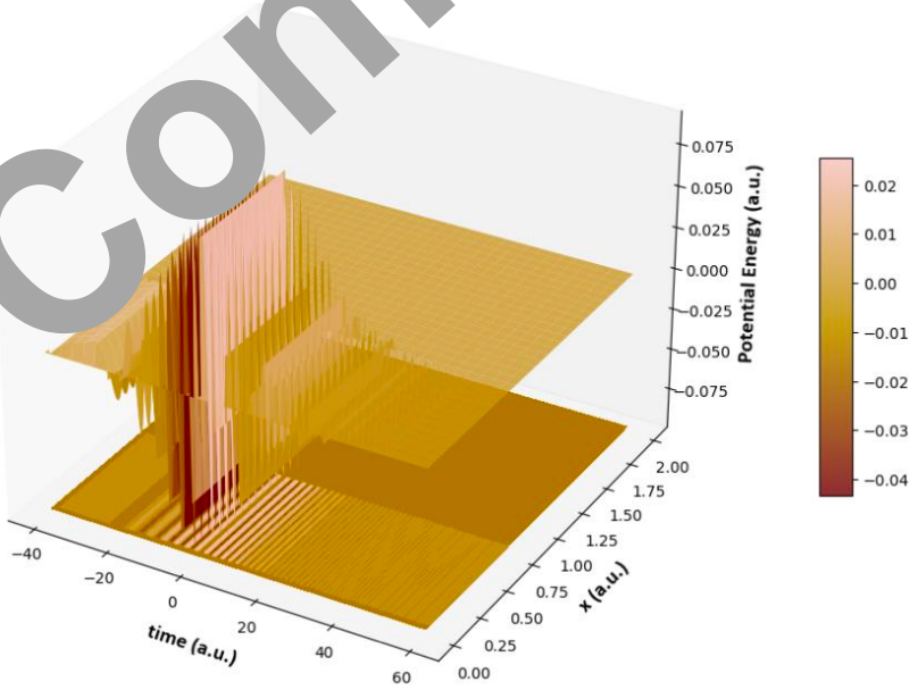

Confidential